Theoretical assessment of the influence of mesa size and shape on the two-dimensional electron gas properties of AlGaN/GaN heterojunctions

Jean-Lou Gosselin

A Thesis

in

The Department

of

Electrical and Computer Engineering

Presented in Partial Fulfillment of the Requirements

for the Degree of Master of Applied Science (Electrical and Computer Engineering) at

Concordia University

Montreal, Quebec, Canada

December 2017

CONCORDIA UNIVERSITY
SCHOOL OF GRADUATE STUDIES

This is to certify that the thesis prepared

By: Jean-Lou Gosselin

Entitled: Theoretical Assessment of the Influence of Mesa Size and Shape on the Two-Dimensional Electron Gas Properties of AlGaN/GaN Heterojunctions

and submitted in partial fulfillment of the requirements for the degree of

Master of Applied Science (Electrical and Computer Engineering)

complies with the regulations of this University and meets the accepted standards with respect to originality and quality.

Signed by the final examining committee:

_____ Chair
Dr. K. Skonieczny

_____ External Examiner
Dr. A. Mohammadi (CIISE)

_____ Internal Examiner
Dr. M.Z. Kabir

_____ Supervisor
Dr. P. Valizadeh

Approved by: _____
Dr. W.E. Lynch, Chair
Department of Electrical and Computer Engineering

_____ 20___

_____
Dr. Amir Asif, Dean,
Faculty of Engineering and Computer Science

ABSTRACT

Theoretical assessment of the influence of mesa size and shape on the two-dimensional electron gas properties of AlGaN/GaN heterojunctions

Jean-Lou Gosselin

AlGaN/GaN heterostructure field-effect transistors (HFETs) are strong candidates for high-power and high-frequency applications. Even in the absence of doping, thanks to high polarization fields, often a two-dimensional electron gas (2DEG) of unprecedented concentrations forms at these heterojunctions. Control over this carrier induction process is crucial in achieving normally-off field-effect transistors (i.e., transistors of zero standby power consumption). One way to achieve this is through polarization engineering. Mesa-isolation geometry seemingly offers interesting avenues to reduce the piezoelectric polarization at the heterointerface, and as a result means for polarization engineering.

Using a Poisson-Schrödinger self-consistent solver, the effect of strain on the sheet charge density is investigated in the context of one-, two- and three-dimensional simulations of AlGaN/GaN heterostructures. Properties of the two-dimensional electron gas are detailed and the influences of Aluminum mole fraction, AlGaN barrier thickness, GaN cap layer inclusion are investigated. The carrier confinement in the 2DEG is explored in the case of two-dimensional version of the simulations. Through these studies, the effect of shrinking the size of the mesa on lowering the 2DEG concentration is confirmed.

Through performing three-dimensional simulations, the effects of cross-sectional geometry on the average sheet charge density and the threshold voltage are presented. It is shown that as the

perimeter-to-area ratio is increased, the carrier concentration decreases, and the threshold voltage becomes less negative. Via these studies, the degree of effectiveness of geometry as means for polarization engineering is, for the first time, theoretically quantified.

AKNOWLEDGEMENTS

First and foremost, I would like to thank Professor Pouya Valizadeh for the constructive supervision, for his ability to share his knowledge and support over the course of my studies. The passion he has for research is contagious. I would also like to thank colleagues, Kaveh Rahbardar, Joseph Record and Merhnegar Aghayan for work ideas. Kaveh has been particularly helpful throughout the various stages of the thesis. I thank my brother, Antoine Gosselin who spent some time discussing and reviewing computational questions. Finally, I thank Jade Desloges, Marlène Asselin, Alexis Gosselin and Guy Gosselin for their unwavering support over the years.

Table of contents

1 Introduction 1
1.1 Status of research on III-nitride field-effect transistors 1
1.2 Motives and outline of the thesis 3
2 Survey of HFETs and fundamental properties of III-nitrides 5
2.1 HFET design 5
2.2 III-nitrides 7
2.2.1 Crystal structure 8
2.2.2 Impact of alloying 10
2.2.3 Polarization in III-nitride semiconductors 11
2.2.4 Calculation of polarization in III-nitrides heterostructures 12
2.2.5 Nonlinearity in assessing polarization parameters 15
2.2.6 Calculation of polarization induced sheet charge concentration 16
2.3 Polarization engineering 17
2.4 Surface states 20
3 Nextnano: principles of simulation 24
3.1 Using the software 24
3.2 Basic assumptions 31
3.2.1 Strain 33
3.2.2 Quantum physics 36
3.2.3 Surface state density 39
4 Study of electron profile at AlGaN/GaN heterojunctions through the one- and two-dimensional simulations 40
4.1 Device structure 40
4.2 Accuracy of simulation and the selection of the required number of eigenvalues 42
4.2.1 Selection of the number of eigenvalues for the one-dimensional version of simulations 43
4.2.2 Number of eigenvalues for simulations of two- and three-dimensional structures 45
4.3 Wave function solutions and energy levels in 1-D and 2-D simulations 47
4.4 Strain evaluation 51
4.5 Sheet charge concentration evaluation 55
4.5.1 Calculating the average sheet charge density 55

4.5.2 Influence of the aluminum mole fraction of the AlGaN barrier, mesa width, and barrier thickness 56
4.5.3 Interpretation of the influence of the mesa's dimensions on the electron distribution profile 58
4.5.4 Carrier confinement 63
4.6 Coexistence of 2DEG and 2DHG 65
4.7 Conclusion 68
5 Evaluation of electron concentration in terms of three-dimensional simulation of AlGaN/GaN heterostructures 69
5.1 Typical challenges in simulating the island-like 3-D isolation features in nextnano 69
5.2 3-D assessment of electron concentration among island-like isolation features 71
5.3 Effect of isolation-feature geometry on carrier concentration 85
5.3.1 Simulating different geometries of different degrees of roundness 85
5.3.2 Assessing the impact of conduction band pinning at the sidewalls 92
5.3.3 Reassessing the use of the perimeter-to-area ratio as a metric 97
5.4 Threshold voltage calculations and results 99
5.4.1 Extracting threshold voltage from the average sheet charge density 99
5.4.2 Influence of mesa geometry and size, AlGaN barrier thickness, and of aluminum mole fraction on the threshold voltage 101
5.4.3 The effect of geometry and size on the hydrostatic pressure 105
5.5 Conclusion 107
6 Conclusion and future works 108
6.1 Conclusion 108
6.2 Future works 109
6.2.1 Quaternary materials 109
6.2.2 Mesa geometries 111
6.2.3 Triple-gate devices 112
7 Bibliography 114

List of Figures

Figure 2.1 – (a) Band diagram for an AlGaAs/GaAs heterojunction and (b) a cross-sectional depiction of an AlGaAs/GaAs HFET with recessed gate and n^+ cap layer. Source: [2]. 6

Figure 2.2 - Relation between bandgap and lattice constant of III-nitrides for the wurtzite (full line) and zinc blende (dashed line) forms. Source: [12]. 7

Figure 2.3 - Wurtzite GaN crystal with lattice constants (a and c). Black and white spheres represent Ga and N atoms, respectively. This crystal is (0001) oriented. Source: [6]..... 9

Figure 2.4 - Basic lattice vectors (a) and reciprocal lattice vectors (b) for the hexagonal crystal system (in the (0001) plane). A few typical directions are shown. Source: [13]..... 10

Figure 2.5 - Orientation of the spontaneous and piezoelectric polarization in Ga- and N-face structures where the barrier is relaxed or under tensile or compressive strain. Source: [14]. 15

Figure 2.6 - (left) AlGaN/GaN triple-gate device as devised in [27]. (Right) Effect of body width reduction on the electron concentration in the bulk. The triple-gate effect is illustrated by the depletion of carriers near the sidewalls. 20

Figure 2.7 - Depiction of the influence of peel forces at corners. 20

Figure 2.8 – Differences between (a) the single ionized surface donor state model of Ibbetson and (b) the distributed surface donor states model of Gordon. Source: [37]. 22

Figure 2.9 - Two-dimensional electron gas density and bare surface barrier height (BSBH) for an $Al_{0.35}Ga_{0.75}N$/GaN heterostructure. Source: [36]. 22

Figure 2.10 – Band diagram for a AlGaN/GaN cylindrical heterostructure whose AlGaN barrier is 20 nm thick and has a 30% aluminum mole fraction. A vertical cut through the mesa is shown with upwards band bending at the sidewalls..... 23

Figure 3.1 - Portion of an input file in nextnano^3 devoted to global variable definition. 26

Figure 3.2 - Example of a structure in a nextnano^3 input file. The keyword, "alloy-function" is completely described using the parameters between the $ symbols. 26

Figure 3.3 – Another example of a structure in a nextnano^3 input file. The above code determines the extent of the simulation region, its structure and composition. 30

Figure 3.4 – Third example of a structure in a nextnano^3 input file. The above code determines the simulation flow, the strain calculation algorithm with the boundary conditions at the sidewalls. It also determines the extent of the simulation region and the crystal growth direction. 31

Figure 3.5 - Self-consistent Schrödinger-Poisson solution for the band edge potential. The loop is entered at the "Solve Poisson Equation" step. Figure adapted from [43]..... 32

Figure 3.6 – Illustration of the strain calculation process in nextnano^3. First, the material grown epitaxially is adjusted to the substrate's lateral lattice constant and then it relaxes by energy minimization scheme. Source: [45]. 36

Figure 4.1 – Cross section of a simulated device structure in nextnano^3. A GaN buffer in which a 2DEG forms is topped by an AlGaN barrier. The device width can be adjusted. The one-dimensional simulation is based on a normal cut to the heterointerface of this structure. 42

Figure 4.2 - Electron concentration for the first three calculated subbands (eigenstates), in units of 10^{18} cm^{-3}, as a function of device depth for a one-dimensional simulation. 44

Figure 4.3 - Subband energy (left axis) and eigenstate density (as a percent of the total sheet charge density (n_s) – right axis) versus the eigenstate number. The grey line at $E = 0$ represents the Fermi level. 45

Figure 4.4 – Subband density as a percentage of the total value versus the eigenstate number for two-dimensional version of simulation of a typical AlGaN/GaN HFET of varying width. 46

Figure 4.5 - Number of calculated eigenvalues needed to reach the 0.05% threshold as a function of the structure size. 47

Figure 4.6 - Gamma conduction and heavy hole valence band edges with electron concentration in the quantum well for a one-dimensional $Al_{0.30}Ga_{0.70}N$/GaN structure with 22 nm thick barrier employing the homogeneous strain algorithm. 48

Figure 4.7- Energy levels and probability density functions (shifted with respect to the eigenvalue energy level) for the three lowest subbands of a 22 nm thick barrier $Al_{0.30}Ga_{0.70}N$ / GaN undoped HFET simulated in 1-D using homogeneous strain algorithm. The Fermi level is set at 0 eV..... 49

Figure 4.8 - Sheet charge density versus mesa width for two-dimensional simulations of AlGaN/GaN structures under quantum mechanical and classical assumptions for 30% aluminum mole fraction and 22 nm thick barrier. Strain minimization algorithm is used. 50

Figure 4.9 - Comparison between classical and quantum based calculations of the electron concentration profile in simulations of an $Al_{0.30}Ga_{0.70}N$ / GaN structure with 22 nm AlGaN barrier thickness. 51

Figure 4.10 – 2-D evaluated electron concentration in AlGaN/GaN structures plotted at different slices of an $Al_{0.3}Ga_{0.7}N$/GaN HFET on a 25 nm wide mesa (middle, x=12.5 nm and side, x=3 nm) using strain minimization and homogeneous strain algorithms. Both homogeneous strain curves overlap. The inset shows the electron concentration (in 10^{18} cm^{-3}) versus width for the peak concentration. Barrier thickness is 20 nm and the structure is simulated under closed simulation region assumptions..... 53

Figure 4.11 - Energy density (in eV/nm^3) of the elastic deformation for (top) homogeneously strained structure and (bottom) minimized strain structure. The GaN buffer (i.e. depth 20 nm and over) is considered completely unstrained..... 54

Figure 4.12 - Hydrostatic strain (sum of the diagonal strain tensor components) for the minimized strain structure. The GaN buffer (i.e. depth 20 nm and over) is considered unstrained. 54

Figure 4.13 - Influence of the aluminum mole fraction of the barrier on the average sheet charge density in 2-D evaluated mesas of different widths and with a 20 nm thick AlGaN barrier. Comparison with data from [35] for a one-dimensional simulation is also made. Jogai assumes $q\phi b = 1.4$ eV for a fix surface donor state, whereas we assume that $q\phi b$ follows $(0.84 + 1.3x)$. The mesas were subject to the strain-minimization algorithm and simulated under closed simulation region assumptions..... 57

Figure 4.14 - Influence of AlGaN barrier thickness on the average sheet charge density for epilayers of different widths (for two-dimensional version of simulation). Aluminum mole fraction is constant at 30%, we thus assume $q\phi b = 1.23$ eV. The structures were simulated under closed simulation region assumptions and the strain minimization algorithms. 58

Figure 4.15 - Electron distribution in the 2DEG of the structure from Figure 4.1, showing the influence of body width. The electron distribution versus width is shown at the depth from the AlGaN surface where the maximum electron concentration occurs. The $Al_{0.30}Ga_{0.70}N$/GaN heterostructures (with AlGaN barrier of 20 nm) were simulated under closed simulation region assumptions and with energy minimization..... 61

Figure 4.16 – Electron distribution in the body of a 100 nm wide $Al_{0.3}Ga_{0.7}N$/GaN structure with an 18 nm thick barrier obtained using the strain minimization algorithm and under the closed simulation region assumptions. Upper left: 2-D view of the carrier distribution. Upper right: 1-D side view showing the extent of the carrier confinement. Lower left: 1-D front view at the peak plane. Lower right: 2-D top view..... 62

Figure 4.17 - Carrier confinement of the 2DEG for a 50 nm wide mesa whose AlGaN barrier is 20 nm thick (indicated by the horizontal red line). The full circles represent the peak of the distribution profile, while the open circles highlight positions Z_L and Z_H as identified in the text. The structures were simulated under closed simulation region and with energy minimization algorithm. 64

Figure 4.18 - Carrier confinement of the 2DEG for a 50 nm wide mesa whose aluminum mole fraction is fixed at 30%. The barrier thickness varies but the scale is with respect to the heterointerface. The circles have the same representation as in Figure 4.17. The structures were simulated under closed simulation region and with energy minimization algorithm. 64

Figure 4.19 - Band diagram and free carrier concentration along the depth of a 1-D simulated GaN/AlGaN/GaN epilayer with a 15 nm GaN cap, 20 nm $Al_{0.3}Ga_{0.7}N$ barrier and 2 eV applied surface potential. 66

Figure 4.20 - Calculated 2DEG and 2DHG sheet charge densities (n_S and p_S) versus barrier height ($q\phi b$) for one-dimensionally evaluated version of GaN/AlGaN/GaN epilayers under the homogeneous strain calculation algorithm with a 20 nm thick AlGaN barrier and 30% aluminum mole fraction. As shown for the 5 nm cap a 2DHG is only formed for higher values of surface potential..... 67

Figure 4.21 - Calculated 2DEG and 2DHG sheet charge densities (n_S and p_S) versus AlGaN barrier thickness for one- and two-dimensional versions of simulation of GaN/AlGaN/GaN epilayers (25 nm wide mesa) under homogeneous strain calculations with 5 or 15 nm thick GaN cap, 30% aluminum mole fraction and fixed 1 eV applied surface potential. 68

Figure 5.1 – A typical island-like AlGaN/GaN heterostructure. Grown along the [0001] axis, the heterostructure is undoped and a Schottky barrier is defined at the top surface..... 71

Figure 5.2 - Comparison between the electron concentration profiles along the width of the isolation feature at the peak of the profile for two- and three-dimensionally simulated AlGaN/GaN heterostructures. All three epilayers have a device width of 50 nm and are simulated under the closed simulation region assumptions. The heterostructures are composed of a 20 nm thick $Al_{0.30}Ga_{0.70}N$ barrier with a 1.23 eV Schottky barrier at the top exposed surface, strain minimization algorithm is in effect. 72

Figure 5.3 – Average sheet charge density versus AlGaN barrier thickness for epilayers simulated in the 1-D, 2-D and 3-D versions of the simulation. Fixed aluminum mole fraction of 30% is assumed as well as a closed simulation region. In the 2-D and 3-D cases, the strain minimization algorithm is in effect. 73

Figure 5.4 - Average sheet charge density versus aluminum mole fraction in the barrier for epilayers simulated in the 2-D and 3-D versions. Among these a fixed AlGaN barrier thickness of 20 nm is assumed as well as a closed simulation region. The Schottky barrier height is given by: $1.3 + 0.84x$ and strain minimization algorithm is in effect. 74

Figure 5.5 – In-plane electron concentration at the peak for the island-shaped polar Ga-face wurtzite AlGaN/GaN heterostructure of 20 nm thick AlGaN barrier of 30% aluminum mole fraction, 50×50 nm^2 top surface area where a 1.23 eV Schottky barrier height is considered and the simulation is performed under the closed simulation domain assumptions and strain minimization algorithm is in effect. 75

Figure 5.6 – In-plane electron concentration at the peak for the (a) island (50×50 nm) and (b) fin-like (30×83.3 nm) AlGaN/GaN heterostructures. Note that the x- and y-axes for the inset (b) are on different scales to highlight the spikes. Both heterostructures have a 20 nm thick AlGaN, 30% aluminum mole fraction, 2500 nm^2 top surface area and 1.23 eV Schottky barrier height and are simulated under the closed simulation regional assumptions. (c) Depicts cuts through the electron concentration profile in the fin-like structure along the short and long axis of the fin. The strain minimization algorithm is in effect. 77

Figure 5.7 – First four wave-function squared solutions for an island-shaped (2500 nm^2 top surface area) $Al_{0.30}Ga_{0.70}N$/GaN heterostructure under energy minimization strain algorithm for simulation domains matching exactly the epilayer structure. 78

Figure 5.8 - First four wave-function squared solutions for an elongated fin-shaped (2500 nm^2 fin-like top surface area) $Al_{0.30}Ga_{0.70}N$/GaN heterostructure under energy minimization strain algorithm for simulation domains matching exactly the epilayer structure. 79

Figure 5.9 – Average sheet charge density versus perimeter-to-area ratio for two types of 3-D simulated epilayers matching exactly the simulation region ("closed simulation"). The aluminum mole fraction is 30% in both cases with a 20 nm thick AlGaN barrier and the strain minimization algorithm is in effect. The fin-shaped epilayer, one side was held constant at 30 nm. The length of the other side was left varying. 81

Figure 5.10 – Elastic energy density (in eV/nm^2) for a 1600 nm^2 (a, b, and c) and a 4900 nm^2 (d, e, and f) polar $Al_{0.30}Ga_{0.70}N$/GaN heterostructures of equal lateral dimensions for "closed simulation region". Figures (a) and (d) show a horizontal cut taken at 0.375 nm and 0.250 nm above the heterointerface, in the barrier for the heterostructures of cross-section 1600 nm^2 and 4900 nm^2, respectively. (b) and (e) zoom in the top left corner of each epilayer to show further details while (c) and (f) show a vertical cut through the depth of the device taken in the middle of it (at y = 20 nm and y = 35 nm, respectively). The strain minimization algorithm is in effect. ... 83

Figure 5.11 – Electron concentration profiles (in (a) and (d)) and hydrostatic strain coefficients (in (b), (c), (e) and (f)) for a 1600 nm^2 (panels a, b, and c) and a 4900 nm^2 (panels d, e, and f) island $Al_{0.30}Ga_{0.70}N$/GaN heterostructures for "closed simulation region". The electron concentration is taken at the peak concentration for both epilayers, (i.e. at a depth of 0.9333 nm and 0.8400 nm below the heterointerface for the 1600 nm^2 and 4900 nm^2 versions, respectively). Figures (b), and (e) show a horizontal cut taken 0.375 nm and 0.250 nm above the heterointerface, in the barrier for the 1600 nm^2 and 4900 nm^2 versions, respectively. (c) and (f) zoom in the top left corner of each epilayer to show detailed level curves. The strain minimization algorithm is in effect. 84

Figure 5.12 - Typical cylindrical AlGaN/GaN heterostructure. Grown along the [0001] axis, the heterostructure is undoped and a Schottky barrier is defined at the top surface. nextnano allows adjustments of the top surface area. 85

Figure 5.13 – Top view of the five different simulated nanowires. (a) triangular prism, (b) cube, (c) hexagonal prism, (d) cylinder, (e) fin-like structure. 87

Figure 5.14 - Top view of a 1600 nm^2 (top surface area) cylindrical nanowire as simulated by nextnano. 87

Figure 5.15 – Illustration of the top views of the rectilinear simulation region boundaries compared to the nanowire itself (darker region). 88

Figure 5.16 - Position of band edges in an island nanowire of 2500 nm^2 top surface area of 20 nm thick $Al_{0.30}Ga_{0.70}N$ barrier, under two different conditions at the sidewalls. This cut is taken 1 nm below the interface in the GaN buffer in the middle of the heterostructure. 89

Figure 5.17 - Electron concentration (in 10^{18} cm^{-3}) in the horizontal peak plane below the heterointerface for five geometries. The white lines on each panel represent the extent of the structures. All structures have a 20 nm thick $Al_{0.30}Ga_{0.70}N$ barrier. The Fermi level pinning is set at 0.6 eV below E_c. The nanowires are of (a) triangular prism, (b) cylinder, (c) fin-like, (d) island-isolated, and (e) hexagonal geometries. 91

Figure 5.18 - Hydrostatic strain in the barrier for a central horizontal cut 1.5 nm above the heterointerface for two island-shaped heterostructures of different top surface areas. Strain minimization algorithm is in effect and simulation domain is closed (no band-bending due to Fermi-level pinning). 92

Figure 5.19 - Conduction band edge in an island-shaped AlGaN/GaN HFET, with 20 nm thick barrier whose aluminum mole fraction is 30%. 3-D simulations are presented for three simulation conditions. 94

Figure 5.20 - Average sheet charge density for a vertical middle cut through an AlGaN/GaN HFET under three simulation conditions. The AlGaN/GaN heterostructure has a 2500 nm^2 top surface area, 20 nm thick AlGaN barrier and a 30% aluminum mole fraction. Among the three cases, strain minimization is in effect. 95

Figure 5.21 - Comparison between the sheet charge densities calculated for AlGaN/GaN heterostructures whose sidewalls are subjected to Fermi level pinning (0.6 eV below E_C) or not ("open"). Four different nanowire geometries of 1600 nm^2 cross-sectional area, are considered. Each structure has a 20 nm thick AlGaN barrier and 30% aluminum mole fraction in the AlGaN barrier. Strain minimization algorithm is in effect..... 96

Figure 5.22 - Average sheet charge density versus top surface area for island-, cylindrical-, and hexagonal-shaped AlGaN/GaN heterostructures. The aluminum mole fraction is 30% in all cases with a 20 nm thick AlGaN barrier. The sidewall condition is set as “open”. Strain minimization is in effect..... 97

Figure 5.23 - Average sheet charge density versus perimeter-to-area ratio for island-, cylinder-, and hexagonal-shaped AlGaN/GaN heterostructures. The aluminum mole fraction is 30% in all cases with a 20 nm thick AlGaN barrier and sidewalls are set as “open”. Strain minimization algorithm is in effect. 98

Figure 5.24 – Average sheet charge density versus the applied surface potential on the top gate for island-, hexagonal prism- and cylindrical-shaped AlGaN/GaN heterostructures of 1225 nm^2 top surface area. The Fermi level at the sidewalls is considered floating. Strain minimization algorithm is in effect. Aluminum mole fraction and AlGaN barrier thickness are 30% and 20 nm, respectively. 100

Figure 5.25 –Influence of AlGaN barrier thickness on the threshold voltage. Average sheet charge density is shown as a function of applied surface potential at the top gate for island-, hexagonal-, and cylindrical-shaped heterostructures of 1225 nm^2 top surface area. The Fermi level at the sidewalls is pinned at 0.6 eV below conduction band level. Strain minimization algorithm is in effect and aluminum mole fraction in the barrier is 30%. 101

Figure 5.26 - Influence of top surface area on the threshold voltage of island-, hexagonal-, and cylindrical-shaped AlGaN/GaN heterostructures. The sidewalls are set as “open”. The AlGaN barrier thickness is 20 nm and the aluminum mole fraction is 30%. Strain minimization algorithm is in effect. 102

Figure 5.27 - Influence of perimeter-to-area ratio on the threshold voltage for island-, hexagonal-, and cylindrical-shaped AlGaN/GaN heterostructures of different top surface areas. The sidewalls are set as “open”. The AlGaN barrier thickness is 20 nm and the aluminum mole fraction is 30%. Strain minimization algorithm is in effect..... 102

Figure 5.28 - Influence of top surface area on the threshold voltage of island-, hexagonal-, and cylindrical-shaped AlGaN/GaN heterostructures. The sidewalls are pinned at 0.6 eV below the conduction band level. The AlGaN barrier thickness is 20 nm and the aluminum mole fraction is 30%. Strain minimization algorithm is in effect. 103

Figure 5.29 - Influence of perimeter-to-area ratio on the threshold voltage of island-, hexagonal-, and cylindrical-shaped AlGaN/GaN heterostructures. The sidewalls are pinned at 0.6 eV below the conduction band level. The AlGaN barrier thickness is 20 nm and the aluminum mole fraction is 30%. Strain minimization algorithm is in effect. 104

Figure 5.30 - Influence of sidewall conditions on the threshold voltage with respect to the top surface area for island-shaped AlGaN/GaN heterostructure with 30% aluminum mole fraction on a 20 nm thick AlGaN barrier. The perimeter-to-area ratio is indicated as a reference metric. Strain-minimization algorithm is in effect. 105

Figure 5.31 - Average hydrostatic pressure in the barrier for island-, hexagonal-, and cylindrical-shaped AlGaN-GaN heterostructures of increasing top surface area compared with a reference value. The reference value is set at the average hydrostatic pressure in the barrier of an island-shaped heterostructures whose top surface area is 900 nm^2. The aluminum mole fraction is 30% and the AlGaN barrier thickness is 20 nm for all heterostructures. Strain minimization algorithm is in effect. 106

Figure 6.1 - Conduction band energy (eV) versus depth in a $Al_{0.3}In_{0.07}Ga_{0.63}N$/GaN mesas for three different AlInGaN barrier thicknesses. 110

Figure 6.2 - Conduction band edges (eV) and electron concentration (10^{18} cm^{-3}) for two quaternary heterostructures with 16 nm thick barriers. 111

Figure 6.3 – Cross-section of a potential two- or three- dimensional simulation including effect of slanted sidewalls. 112

List of Tables

Table 1.1 - Material properties at 300 K. 2

Table 2.1 - Structural parameters (a_0, c_0, c_0/a_0 and u_c) and experimentally evaluated elastic constants for AlN, GaN and InN of wurtzite form. References are indicated in the Table. 9

Table 2.2 - Cell-internal bowing parameters (u_c) for ternary III-nitride alloys. Source: [16]. 11

Table 2.3 - Pyroelectric and piezoelectric constants. Sources are indicated in the table. 14

Table 3.1 - Summary of main characteristics of the most useful strain algorithms in nextnano^3. 34

Table 4.1 – Assumptions adopted in this work and in [27]. 59

List of Abbreviations

Abbreviation	Description
2DEG	Two-dimensional electron gas
2DHG	Two-dimensional hole gas
BSBH	Bare surface barrier height
EPC	Efficient power conversion
FET	Field effect transistor
HEMT	High electron mobility transistor
HFET	Heterojunction field effect transistor

Chapter 1

Introduction

Using heterojunctions in realizing transistors dates back to 1979 when Mimura paired an n-type doped AlGaAs layer with undoped GaAs to create the first high electron-mobility transistor (HEMT) [1]. This presented a great way to achieve higher operating speeds. Mimura's intuition was to use the field-effect of a gate electrode to control electron population at the interface between AlGaAs and GaAs [2]. In these heterojunctions, thanks to the higher electron affinity of GaAs, free electrons resulting from the ionization of the dopants present in the AlGaAs layer transfer to the undoped GaAs side to form a two-dimensional electron gas (2DEG). In this Fermi gas, due to spatial separation between dopants and carriers, electron mobility is observed to vastly enhance. Once the concept was laid down and turned into a reality, the next step was to search for other such heterojunctions that would improve different aspects of device operation.

1.1 Status of research on III-nitride field-effect transistors

Over the past two decades, the field of III-nitrides semiconductors has flourished. Thanks to the observed high critical electric field, wide bandgap and high electron drift-velocity among many members of this semiconductor family, they are deemed well suited for power transistor and high frequency device applications. Despite these luring advantages, a myriad of issues still stand in the

way of commercialization of this technology. One such issue is the price. Quite recently, a California-based company (Efficient Power Conversion – EPC for short), offered two GaN-based power transistors (60 volt and 100 volt designs) at prices cheaper than their silicon counterpart [3]. This is one of the first times, if not the first, that a gallium nitride product, boasting similar performance, is priced cheaper than the typical silicon transistor. This seems encouraging as we start to delve further into the topic of III-nitride devices.

Table 1.1 presents a summary of the properties of GaN, as the most studied member of the III-nitride family for the channel of field-effect transistors versus those of some of its rivals in high power and high frequency applications.

Table 1.1 - Material properties at 300 K.

Property	GaN[1]	GaAs	Si [4]
Bandgap – E_g (eV)	3.434 (direct) [5]	1.42 – 1.435 [5] (direct)	1.13 (indirect)
Electron mobility - μ ($cm^2V^{-1}s^{-1}$)	2000 [6]	8800 [4]	1417
Breakdown field – E_{br} (Vcm^{-1})	3×10^6 [6]	3.5×10^5 [4]	3×10^5

In comparison to these rivals, because of the large bandgap, GaN devices can operate at higher temperatures and have a higher breakdown voltage, which make them suitable for power electronic applications. In addition, the polar nature of the wurtzite crystalline form in properly designed III-nitride heterojunctions offers an extremely high carrier density, which allows for higher maximum current.

After two decades of intensive research on III-nitride transistors, research for fully unleashing the power of this technology is still ongoing. Understanding the gate leakage, the effect of mesa geometry on the carrier density and the role played by the quaternary alloys in realization of HFETs

[1] Considering the wurtzite form of gallium nitride.

are only some of the directions in which progress still must be made. An important endeavor to achieve this progress is through computer modeling. To understand the implications of polarization in wurtzite III-nitrides, advanced models offering accurate appreciation of the microscopic physics are needed. Over the years, increased computational power has enabled more sophisticated models. For III-nitride materials specifically, this means models capable of accounting for the effect of strain on deformation potentials and piezoelectric fields [7], in addition to allowing for different alloy compositions and multi-dimensional confinements to be considered.

1.2 Motives and outline of the thesis

In this thesis, physics-based numerical models are employed in the *nextnano* environment [8] [9]. *Nextnano* is a semiconductor nanodevice simulation tool which allows accurate assessment of the link between polarization and charge induction. Simulations are performed on AlGaN/GaN epilayers in quest for normally-off[2] transistors by investigating various design parameters. One recently proposed way to achieve this feat is through polarization engineering [10] [11]. Reducing the piezoelectric polarization at the heterointerface, via lowering the density of carriers in the well, contributes to a positive shift in the threshold voltage. Reducing the size of the isolation mesa and changing its geometry are interesting avenues in this regard. This thesis will thus present, via numerical simulations, design strategies for realization of HFETs aiming for normally-off behavior based on polarization engineering at the AlGaN/GaN heterointerface.

[2] These are n-channel transistors with a positive threshold voltage, hence zero standby power consumption.

Chapter 2 introduces relevant theories and background information needed to understand the intricacies of the simulations. In this chapter, the various material parameters and simulation assumptions are highlighted. Chapter 3 presents a brief survey of the *nextnano* software that was used to perform the simulations. In this chapter, the model and the strain calculation algorithm are presented. Chapter 4 is devoted to the analysis of simulations performed on one- and two-dimensional simple AlGaN/GaN epilayers. Results presented in this chapter confirm that the carrier confinement in the quantum well depends on the aluminum mole fraction and barrier thickness. Finally, in this chapter results of additional simulations via introducing a GaN cap layer on the epilayer are presented. The discussions of chapter 5 reveal how the carrier concentration varies in three-dimensional structures of different lateral geometries. In these discussions, based on the extraction of threshold voltage, the variation for this parameter is investigated with the perimeter-to-area ratio of the top surface of the isolation feature. Chapter 6 includes concluding remarks and three possible directions for future work.

Chapter 2

Survey of HFETs and fundamental properties of III-nitrides

The polar nature of the wurtzite III-nitrides demands a close attention to the correlation between the polarization and charge-induction. In the present chapter, in addition to a brief presentation of the operation principles of heterostructure FETs, the issue of polarization in III-nitrides is particularly highlighted.

2.1 HFET design

Improving the switching speed and expanding the operation frequency of FETs among other things require elimination of the sources of carrier scattering. One way to achieve this, as it was hinted in the introduction, is through the realization of heterojunction field effect transistors (i.e. HFETs) using modulation doping technology[3]. In Mimura's first depiction of the AlGaAs/GaAs transistor [2], an undoped GaAs layer is grown on top of a semi-insulating GaAs substrate. On top of this undoped layer, the heterojunction is formed through growing an n-type doped layer of $Al_xGa_{1-x}As$ (x = 0.32). The typical band diagram in the vicinity of this heterojunction is depicted in Figure 2.1

[3] Devices made using this principle are also termed Modulation Doped Field Effect Transistor (MODFET) or High Electron Mobility Transistor (HEMT).

(a). Figure 2.1 (b) presents a cross-sectional depiction of an AlGaAs/GaAs HFET with indication of source, drain and recessed gate electrodes, n^+ GaAs cap layers. These devices are often isolated from the neighboring transistors on a chip by selective removal of the heterostructure and as a result the 2DEG. This type of isolation is referred to as mesa-isolation.

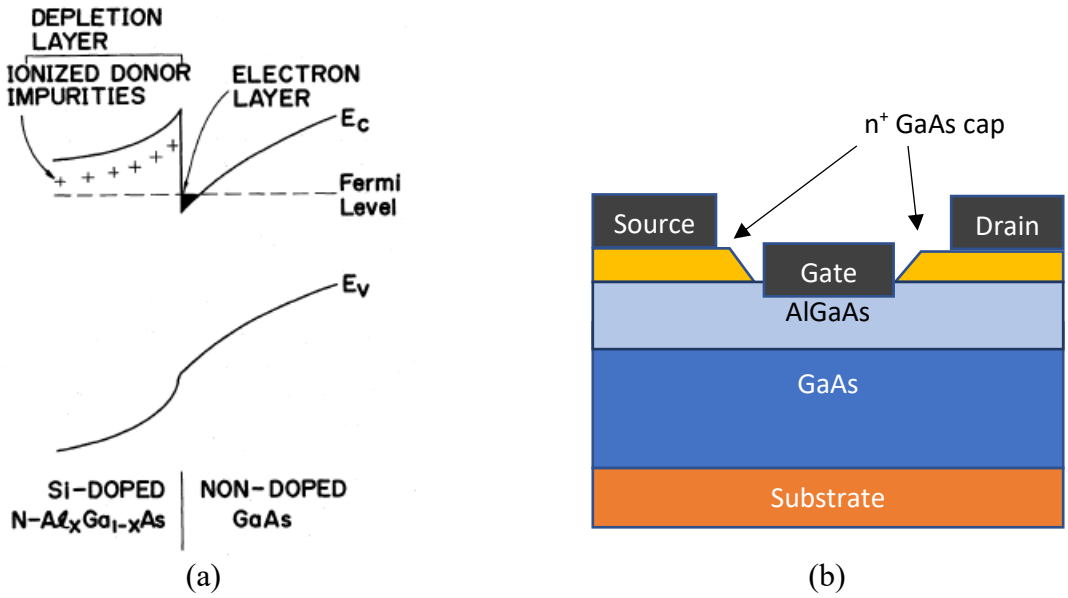

Figure 2.1 – (a) Band diagram for an AlGaAs/GaAs heterojunction and (b) a cross-sectional depiction of an AlGaAs/GaAs HFET with recessed gate and n^+ cap layer. Source: [2].

As suggested in Figure 2.1 (a), a two-dimensional electron gas (2DEG), caused by the conduction band discontinuity, forms on the small bandgap GaAs side. The electrons of this 2-D gas originate from the donors introduced into the AlGaAs barrier. The resulting formation of a charge dipole across the heterojunction and the conduction band discontinuity lead to a band bending, creating a quantum well in which the electrons are two-dimensionally confined. The great benefit of this electron confinement resides in the fact that the confined carriers are now free to move in a plane parallel to the heterojunction, but not in the growth direction. Caused by the spatial separation

from the ionized impurities, this allows for a very high electron mobility. For the first GaAs HFET, with 32% aluminum mole fraction and 6.6×10^{17} cm^{-3} barrier doping level, the Hall electron mobility was observed to be 30% higher at 300K and up to 5.5 times higher at 77K, when compared to a conventional Schottky-gate GaAs metal-semiconductor field effect transistor (MESFET) of similar carrier concentration [2].

2.2 III-nitrides

The introduction of polar materials, in the form of III-nitrides, to HFETs reduced the need for doping. The unique properties of gallium nitride and its alloys (mainly AlGaN and InGaN in ternary compositions) are sought in many electronic and also optoelectronic devices. Figure 2.2 shows the variation of bandgap energy with respect to the lattice constant for both wurtzite and zinc blende forms of the most studied III-nitride binaries and their ternary alloys.

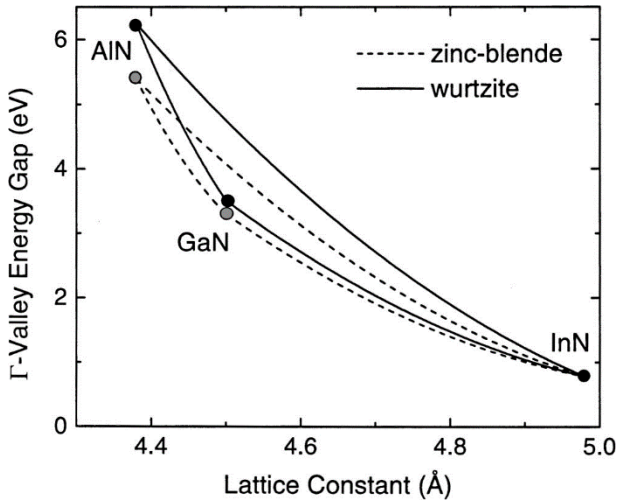

Figure 2.2 - Relation between bandgap and lattice constant of III-nitrides for the wurtzite (full line) and zinc blende (dashed line) forms. Source: [12].

2.2.1 Crystal structure

III-nitride materials are normally grown in the form of the hexagonal (wurtzite) crystal system, contrary to GaAs or InP that are grown in the zinc blende system. Figure 2.3 shows a unit cell of the hexagonal wurtzite crystal of GaN grown along the (0001) direction with indication of lattice constants *a* and *c*. Due to termination with Ga atoms, the crystal unit cell of Figure 2.3 is referred to as Ga-face. Ideal wurtzite lattice constants identified in a maximally close-packed hexagonal structure require $c/a = \sqrt{(8/3)} = 1.633$, where *a* is the hexagonal edge and *c* is the height of the hexagonal prism [13]. Also, in this ideal structure, the bond-length u_c needs to be equal to $3/8 = 0.375 \cdot c$. Substantial deviation from these ideal values among III-nitrides, especially when III-nitrides of different degrees of non-ideality form a heterojunction, is one of the major sources of polarization induced charges at such heterointerfaces.

In addition to this mechanism of charge induction, which is known as spontaneous polarization, strained growth of lattice-mismatch III-nitride heterojunctions in the pseudomorphic form serves as a complimentary mechanism of polarization charge induction. This mechanism is referred to as the piezoelectric effect.

To account for mismatch in the lattice constants, the elastic constants of each of the materials forming the junction are needed. These are labelled as C_{ij}. The most relevant of these structural parameters and lattice constants to charge induction for the case of AlN, GaN and InN are provided in Table 2.1. These values are the ones employed in the simulations reported in this thesis.

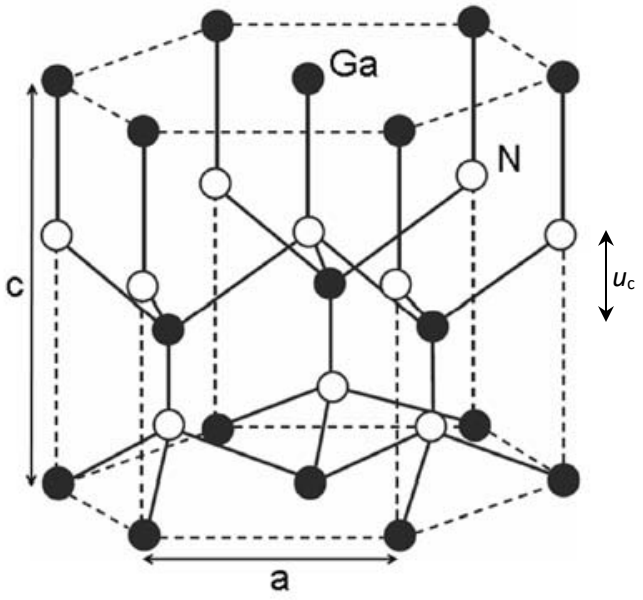

Figure 2.3 - Wurtzite GaN crystal with lattice constants (a and c). Black and white spheres represent Ga and N atoms, respectively. This crystal is (0001) oriented. Source: [6].

Table 2.1 - Structural parameters (a_0, c_0, c_0/a_0 and u_c) and experimentally evaluated elastic constants for AlN, GaN and InN of wurtzite form. References are indicated in the Table.

Wurtzite (@ 300 K)	**AlN**	**GaN**	**InN**
a_0 (Å) [12]	3.112	3.189	3.545
c_0 (Å) [12]	4.982	5.185	5.703
c_0/a_0 (exp.) **[14]**	1.6010	1.6259	1.6116
***u_c* [14]**	0.380*c*	0.376*c*	0.377*c*
C_{11} (GPa) [12]	396	390	223
C_{12} (GPa) [12]	137	145	115
C_{13} (GPa) [12]	108	106	92
C_{33} (GPa) [12]	373	398	224
C_{44} (GPa) [12]	116	105	48

In naming the directions in hexagonal lattices using Miller Bravais indices, the vectors $\mathbf{a_i}$ are shown in Figure 2.4 indicating a few typical directions. The reciprocal lattice vectors indicating the hexagonal form of the first Brillouin zone are also shown in this figure.

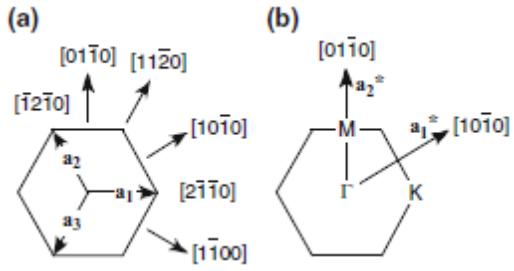

Figure 2.4 - Basic lattice vectors (a) and reciprocal lattice vectors (b) for the hexagonal crystal system (in the (0001) plane). A few typical directions are shown. Source: [13].

2.2.2 Impact of alloying

In the heterostructures studied in this thesis, the ternary alloy, $Al_xGa_{1-x}N$ is in contact with a thick GaN buffer layer. Thus, the impact of alloying AlN and GaN is important to describe. Depending on the Al-composition (i.e. x), up to a certain thickness of AlGaN layer, pseudomorphic growth of AlGaN/GaN layers has been demonstrated [14]. Pseudomorphic growth occurs when the epilayer undergoes strain to match the lattice constant of the substrate [15]. While the freestanding AlN has a smaller lateral lattice constant compared to GaN, such a pseudomorphic growth imposes tensile strain on the so-called AlGaN barrier layer. This layer will undergo cracking when the layer thickness is beyond a certain x-dependent value.

Material parameters for $Al_xGa_{1-x}N$ alloy can be approximately inferred through a weighted averaging law referred to as Vegard's law. According to the generic form of this law, in an alloy of x part PN and $1-x$ part QN (i.e. in $P_xQ_{1-x}N$ alloy), a parameter such as lattice constant would be calculated using an equation of the form [16]:

$$a_{P_xQ_{1-x}N} = a_{PN}x + a_{QN}(1-x) + bx(1-x) \tag{2.1}$$

where, b is the bowing parameter.

For some parameters, like lattice constants, b is often taken as zero, yielding:

$$a_{\mathrm{AlGaN}}(x) = (3.1986 - 0.0891x)10^{-10}\ \mathrm{m} \quad (2.2)$$

$$c_{\mathrm{AlGaN}}(x) = (5.2262 - 0.2323x)10^{-10}\ \mathrm{m}. \quad (2.3)$$

In contrast to this assumption, in assessing u_c, it scales non-linearly with ternary alloy composition. Values used for all three ternaries in assessing u_c are indicated in Table 2.2.

Table 2.2 - Cell-internal bowing parameters (u_c) for ternary III-nitride alloys. Source: [16].

	AlGaN	**AlInN**	**InGaN**
Bowing parameter (b) used in evaluating cell-internal factor (u_c)	-0.0032	-0.0086	-0.0057

2.2.3 Polarization in III-nitride semiconductors

In the (0001) direction, wurtzite crystals of III-nitrides lack a center of symmetry, causing the development of charge dipoles. As mentioned earlier, in III-nitride heterostructures, two types of polarization can emerge: spontaneous ($\mathbf{P}_{SP}$) and piezoelectric ($\mathbf{P}_{PZ}$). It is worth noting that spontaneous polarization exists in two classes of materials: ferroelectrics and pyroelectrics [17]. The nature of III-nitrides is that of pyroelectrics, in which the pyroelectric axis (and $\mathbf{P}_{SP}$) is parallel to the (0001) direction. Whereas in ferroelectric materials the polarization can be reversed when an electric field is applied, in pyroelectric materials the direction of polarization is fixed along one of the crystal symmetry axes. The name pyroelectric stems from the fact that these properties are observed and measured when a change of temperature induces a change in the spontaneous polarization.

In pyroelectric materials, the polarization is permanent and is an intrinsic property of the material, which can be calculated based on the modern theory of polarization. Also known as *Berry's Phase* method, this is a computational tool that relies on the Density Functional Theory (DFT) and

calculates the change in polarization from first-principles [18]. The spontaneous polarization property can be explained by the fact that one of the four bonds in the lattice (i.e. the one oriented along the [0001] direction) is not electronically equivalent to the other three [6]. In this bond, the geometric center of the negative charges (electrons) is slightly displaced with respect to the geometric center of the positive charges (nuclei), causing a lack of a center of symmetry [19]. The spontaneous polarization in wurtzite crystals is thus intimately linked with u_c, the cell internal parameter.

In addition to their particular non-centrosymmetric nature and pyroelectric behavior, III-nitride materials are also among a group of materials known as piezoelectrics. These are materials generating an electrical polarization when placed under an external stress causing strain in the lattice. In these materials, the opposite is also true. Namely, that an external electric field can induce mechanical stress [20]. In these materials, in the same way as a difference in bond ionicity can induce a polarization, an external mechanical stress affecting the physical bond lengths can also trigger a polarization phenomenon. In III-nitrides, in the absence of any other external field, the total polarization $\mathbf{P_{tot}}$ can be presented as:

$$\mathbf{P_{tot}} = \mathbf{P_{SP}} + \mathbf{P_{PZ}}. \tag{2.4}$$

2.2.4 Calculation of polarization in III-nitrides heterostructures

Spontaneous polarization in III-nitrides of wurtzite form is very strong. AlN, among all III-nitrides, exhibits the largest spontaneous polarization. In terms of the piezoelectric coefficients, the piezoelectric polarization is expressed as [21], [22]:

$$P_{PE} = e_{33}\epsilon_z + e_{31}(\epsilon_x + \epsilon_y) \tag{2.5}$$

where e_{13}, e_{33}, and e_{15}[4] are the piezoelectric coefficients. In this expression, $\epsilon_z = (c - c_0)/c_0$ is the strain along the *c* axis and $\epsilon_x = \epsilon_y = (a - a_0)/a_0$ refer to the in-plane strain, where the lattice constants indicated with the subscript of 0 stand for the freestanding lattice constant. Also, the relation between the lattice constants in terms of the elastic constants is given as,

$$\frac{c - c_0}{c_0} = -2\frac{C_{13}}{C_{33}}\frac{a - a_0}{a_0}. \tag{2.6}$$

Combining equations (2.5) and (2.6) with the expressions for $\epsilon_{x,y,z}$ yields an expression for the piezoelectricity along the *c* axis [14] [22], namely:

$$P_{PE} = \frac{2(a-a_0)}{a_0}\left(e_{31} - e_{33}\frac{C_{13}}{C_{33}}\right). \tag{2.7}$$

For AlGaN, the quantity in the second parenthesis in equation (2.7) is always negative inducing a negative piezoelectric polarization for tensile strain, and conversely a positive polarization for compressively strained barrier. On the other hand, the spontaneous polarization for AlN and GaN is always negative, where the positive direction is defined from N to Ga atoms. The polarity then depends on the growth surface of the structure, which as a result switches directions with Ga- or N-face crystals. Figure 2.5 shows the different possible orientations of spontaneous and piezoelectric polarization vectors depending on the growth surface (i.e. Ga- or N-face) and on the strain type of the barrier. In this figure, σ refers to as the polarization sheet charge formed on the AlGaN side of the heterojunction. All the relevant values are summarized in Table 2.3.

[4] e_{15} is the third component of the piezoelectric tensor and relates to shear strain, and in pseudomorphic growth is excluded from (2.5).

In addition to the major differences in terms of the dominant presence of spontaneous polarization, the III-nitrides are different from other III-V semiconductors in that they have piezoelectric constants about 10 times larger than other III-Vs [21]. The piezoelectric constants of III-nitrides also have the opposite sign compared to other III-V semiconductors. This is because of the prevalence of the ionic internal-strain thanks to a higher Born effective charge[5].

Table 2.3 - Pyroelectric and piezoelectric constants. Sources are indicated in the table.

Material	$\mathbf{P_{SP}}$ (C m^{-2}) **[6]**	$\boldsymbol{e_{33}}$ (C m^{-2}) **[5]**	$\boldsymbol{e_{31}}$ (C m^{-2}) **[5]**	$\boldsymbol{e_{15}}$ (C m^{-2})
AlN	-0.0898	1.79	-0.50	-0.48 [16]
GaN	-0.0339	1.27	-0.35	-0.30 [16]
InN	-0.0413	0.97	-0.57	-0.112 [6]

[5] The Born effective charge, denoted Z*, is defined as the variation in polarization when an ion (or a lattice) is displaced from its equilibrium position.

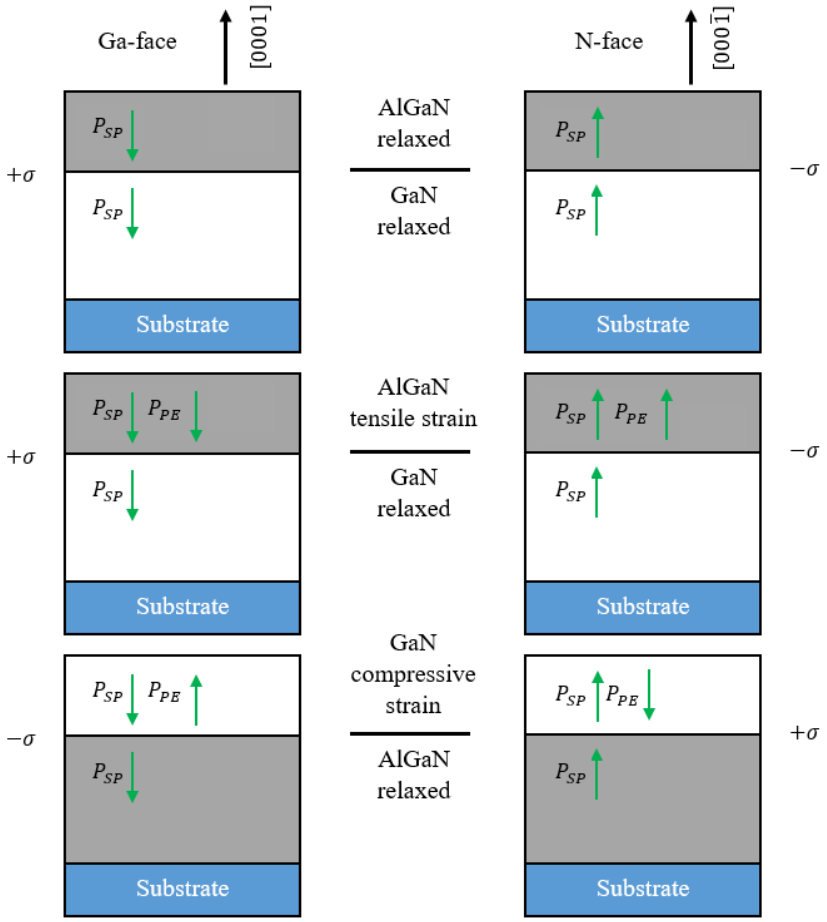

Figure 2.5 - Orientation of the spontaneous and piezoelectric polarization in Ga- and N-face structures where the barrier is relaxed or under tensile or compressive strain. Source: [14].

2.2.5 Nonlinearity in assessing polarization parameters

As it was earlier indicated in Section 2.2.2, the internal-cell parameter, u_c, scales non-linearly with the aluminum content of the ternary AlGaN. Since the macroscopic polarization depends highly on the geometry of the structure, it is correct to anticipate that this property could also present a nonlinear behavior [23]. The impact of the resulting spontaneous polarization nonlinearity is approximated by a parabolic function [16] [23]:

$$P^{\mathrm{SP}}_{\mathrm{AlGaN}}(x) = xP^{\mathrm{SP}}_{\mathrm{AlN}} + (1-x)P^{\mathrm{SP}}_{\mathrm{GaN}} + bx(1-x) \tag{2.8}$$

$$P_{\mathrm{AlGaN}}^{\mathrm{SP}}(x) = -0.090x - 0.034(1-x) + 0.021x(1-x) \tag{2.9}$$

where the bowing parameter b is defined as:

$$b = 2P_{\mathrm{AlN}}^{\mathrm{SP}} + (1-x)P_{\mathrm{GaN}}^{\mathrm{SP}} - 4P_{\mathrm{Al_{0.5}Ga_{0.5}N}}^{\mathrm{SP}}. \tag{2.10}$$

Apart from the non-linearity due to the internal-cell parameter, alloy composition also influences the bowing parameter [23]. Hence, when the mismatch between the atoms is the largest[6], the bowing is also more prominent.

Piezoelectric polarization also manifests non-linearity. The root cause of this observation is the nonlinear strain dependence of the bulk piezoelectricity. In evaluation of this, although basal strain $\epsilon(x)$[7] is calculated using Vegard's law, the nonlinearity of the piezoelectric polarization constants from the binaries is considered in the following formula:

$$\mathrm{P_{pz}} = \mathrm{e}_{33}\epsilon_z + 2e_{31}\epsilon_x. \tag{2.11}$$

2.2.6 Calculation of polarization induced sheet charge concentration

The sheet charge density at the III-nitride heterointerface is predominantly calculated in terms of the divergence of the polarization fields: $\rho_p = -\nabla \cdot \mathbf{P}$. In terms of the direction of the two polarization fields, when the heterostructure is grown on the c-plane, the sheet charge density can be simply presented as:

[6] AlInN and InGaN, for example, compared to AlGaN are more unideal.
[7] The basal strain for an alloy layer is $\epsilon(x) = (a_{subs} - a(x))/a(x)$. Here, a_{subs} is the lattice constant of the substrate and $a(x)$ is the lattice constants of the unstrained alloy.

$$\sigma = P_{\text{bottom}} - P_{\text{top}}. \tag{2.12}$$

Provided the polarization induced sheet charge density is positive, then free electrons in the structure will accumulate near the interface. This will result in the creation of a 2DEG at the quasi-triangular quantum well formed between the barrier AlGaN and the channel GaN layer. For an undoped Ga-faced device, the total carrier concentration is given by [14]:

$$n_s(x) = \frac{\sigma(x)}{q} - \left(\frac{\varepsilon_0 \varepsilon(x)}{d_{\text{AlGaN}} q^2}\right)\left(q\phi_b(x) + E_F(x) - \Delta E_C(x)\right). \tag{2.13}$$

Here, d_{AlGaN} is the thickness of the $Al_xGa_{1-x}N$ barrier, $q\phi_b$ is the height of the Schottky barrier at the gate contact which varies depending on the alloy composition and the gate metal, E_F is the Fermi level, ΔE_C is the conduction band discontinuity and $\varepsilon(x)$ is the relative dielectric constant of the barrier, ε_0 is the permittivity of the air, and q is the charge of an electron. In the simulations presented later in this thesis, a typical Ni Schottky barrier contact is assumed. In terms of the Al composition of the barrier, *x*, this choice relates to [14]:

$$q\phi_b = (1.3\,x + 0.84)\ \text{eV}. \tag{2.14}$$

2.3 Polarization engineering

Since the piezoelectric effect can immensely influence the sheet charge density and distribution across a III-nitride heterointerface, the study of the development and propagation of strain through these heterojunctions is quite vital to understanding the capacities of this material system.

The high carrier concentration induced by piezoelectric polarization and the difference in spontaneous polarization across the heterointerface leads to the problem of standby power

consumption, when one wants to fabricate an AlGaN/GaN HFET especially suitable for switching applications. It is thus important to find ways for realizing normally-off III-nitride HFETs (i.e. of positive threshold voltage). Reducing the aluminum mole fraction in the barrier, is one of the ways leading to less negative threshold voltage. This approach, however, due to the smaller conduction band discontinuity between the channel and the barrier layer offers a reduced carrier confinement in the channel and a greater gate-leakage current. Over the past two decades, several alternative approaches have been studied for realization of normally-off GaN HFET switches.

Barrier-thinning, fluoride-based plasma treatment, employing lattice-match III-nitride quaternaries instead of AlGaN as the barrier and exploring the correlation between the piezoelectric polarization and the lateral geometry of the III-nitride heterostructures are some of the methods explored for positive shifting the threshold voltage

In addition to the need for realizing HFETs of positive threshold voltage for switching applications, in these applications the possibility of parallel realization of an HFET serving as a current source with a negative threshold voltage is high on the list of demands. From this perspective, the techniques explored for positive shifting the threshold voltage like the adoption of a lattice-match heterointerface that uniformly affect the threshold voltage across the wafer face a deficiency. In comparison to this technique, polarization engineering via changing the geometry and size of the isolation mesa among the normally-on and normally-off devices allows a major breakthrough. Among III-V integrated circuits, a popular isolation technology is the mesa isolation which relies on removal of the heterostructure and essentially the channel between the devices built on individual mesas.

On the topic of observation of positive shift in threshold voltage of HFETs realized on very small-size mesas, and also on other isolation geometries allowing a higher perimeter-to-area ratio, over

the past five years a number of publications have surfaced [11] [24] [25] [26]. While still to a certain degree unsettled, these observations have been attributed to a combination or the individual effect of two mechanisms: the triple-gate depletion effect and strain relief caused by the reduction of the feature size.

The first of these mechanisms identifies the broader coverage of the channel width by the depletion region width induced due to the presence of sidewall covering portions of the gate electrode, responsible for the observed positive shift in the threshold voltage of the devices realized on very small mesas. This so-called triple-gate effect is illustrated in Figure 2.6. Whereas this depletion mechanism serves as a very viable cause, a certain body of work has so far illustrated that it cannot be the sole culprit [10] [27] [28]. Development of peel forces around the mesa perimeter and eventual reduction of strain and piezoelectric polarization, which have been previously reported in case of SiGe heterostructures, is speculated to be the complimentary cause [29] [30] [31]. A schematic representation of this phenomenon is shown in Figure 2.7. Whereas in case of the SiGe technology theoretical evaluations forecast tangible strain relief even in the center of isolation mesa [32], such an exhaustive theoretical evaluation on the scope and possibilities offered by strain relief in AlGaN/GaN HFETs was up to now missing.

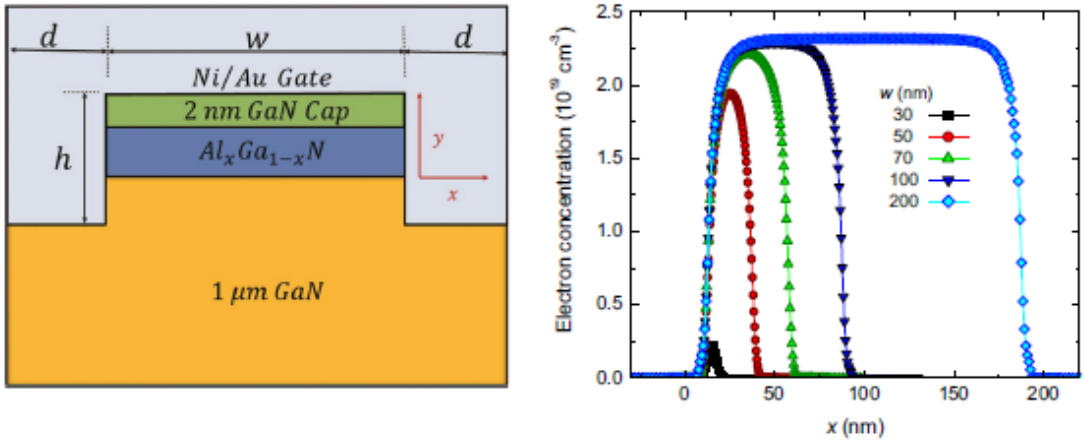

Figure 2.6 - (left) AlGaN/GaN triple-gate device as devised in [27]. (Right) Effect of body width reduction on the electron concentration in the bulk. The triple-gate effect is illustrated by the depletion of carriers near the sidewalls.

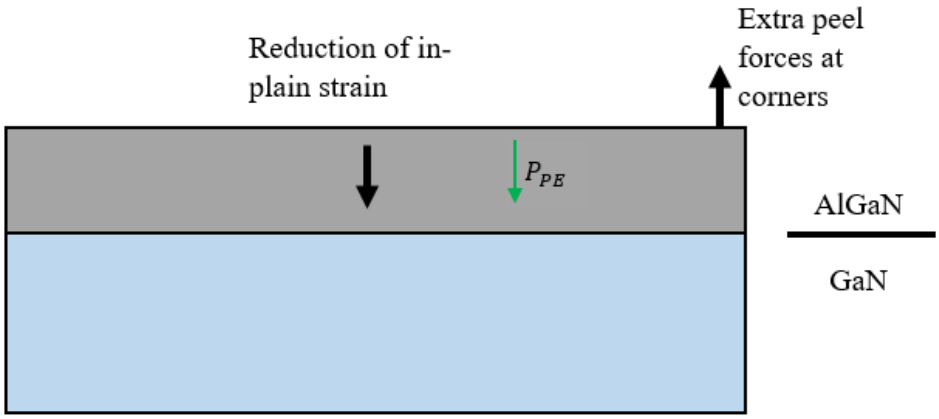

Figure 2.7 - Depiction of the influence of peel forces at corners.

2.4 Surface states

The discussions of this section are crucial to the implementation and determination of boundary conditions in the simulations presented in chapter 5. In here, following a brief discussion on the origins of 2DEG, a discussion on surface states in GaN structures is presented.

It was indicated earlier that AlGaAs/GaAs HEMTs need barrier doping to populate the 2DEG. In the case of polar III-nitride heterostructures, the 2DEG can be formed even in the absence of

intentional barrier doping [22]. This raises a question on the origins of these polarization-induced electrons. One of the early models developed on this topic, proposed that electrons originate from donor surface states of the barrier [33] [34] [35].

According to Ibbetson, the origin of the electrons populating the 2DEG is the uncompensated surface donor states [34]. This is illustrated in Figure 2.8 (a). Ibbetson assumes a deep donor state, with energy E_d. As the AlGaN barrier thickness increases, the unscreened polarization dipole[8] decreases up to the point where the donor energy merges with Fermi level, allowing electrons to populate the 2DEG. This model was refined later to include the effects of distributed surface donor states [36] [37] [38] [39].

These later modifications came to the conclusion that instead of a fixed E_d, the surface donors are spread over a certain range of energy, as illustrated in Figure 2.8 (b). As the AlGaN layer thickness increases, the bottom of the conduction band separates more from the Fermi level and, as a result, the donor states start transferring electrons to the 2DEG. Figure 2.9 shows the existing correlation between the 2DEG density and the bare surface barrier height (BSBH)[9].

Depending on surface polarity and orientations, Segev and Van de Walle identified dangling bonds as the mechanism that pins the Fermi level at 0.5 and 0.7 eV below the conduction-band minimum for the non-polar $(11\bar{2}0)$ and $(1\bar{1}00)$ plane orientations of GaN, respectively and at 0.6 eV below the conduction-band minimum for the polar (0001) plane orientation of GaN [40] [41]. Whereas important to 2DEG induction, as illustrated in the example of Figure 2.10, this pinning also introduces an upwards band bending towards the exposed sidewall surfaces causing 2DEG reduction in their vicinity. The structure shown in this figure, which will be defined in more details

[8] In [34], the polarization dipole results from the polarization-induced charges whose net sum to the total space charge must be zero.

[9] This is the surface barrier height $q\phi_B$ in the absence of a gate metal (bare surface).

in Chapter 5 is a cylinder-shaped AlGaN/GaN heterostructure with 30% aluminum mole fraction, 20 nm thick AlGaN barrier. In here, a 1.0 V surface potential is applied at the top surface and a 0.6 eV Fermi level pinning below the conduction band level is applied to the sidewalls. The one-dimensional cut is taken through the center of the heterostructure.

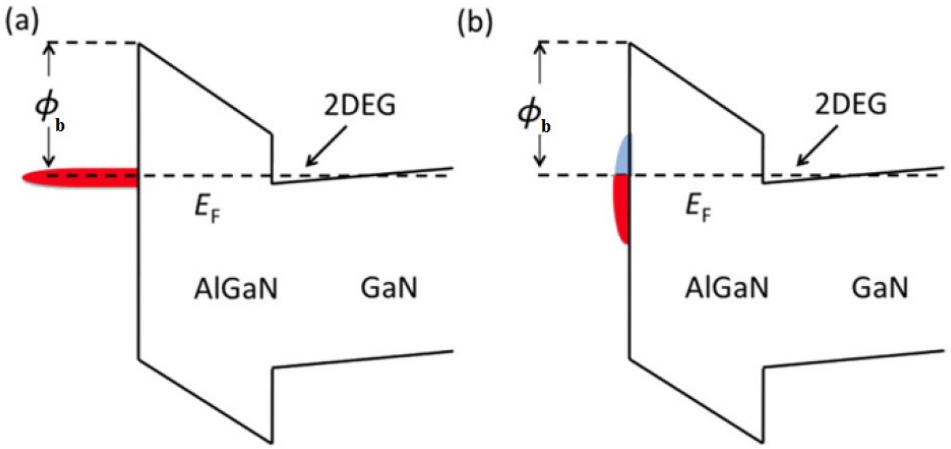

Figure 2.8 – Differences between (a) the single ionized surface donor state model of Ibbetson and (b) the distributed surface donor states model of Gordon. Source: [37].

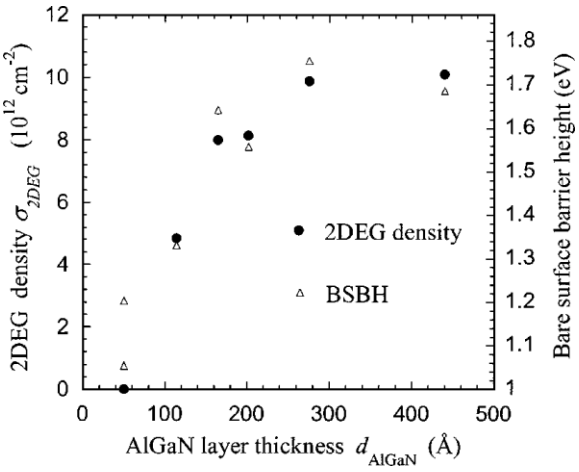

Figure 2.9 - Two-dimensional electron gas density and bare surface barrier height (BSBH) for an $Al_{0.35}Ga_{0.75}N$/GaN heterostructure. Source: [36].

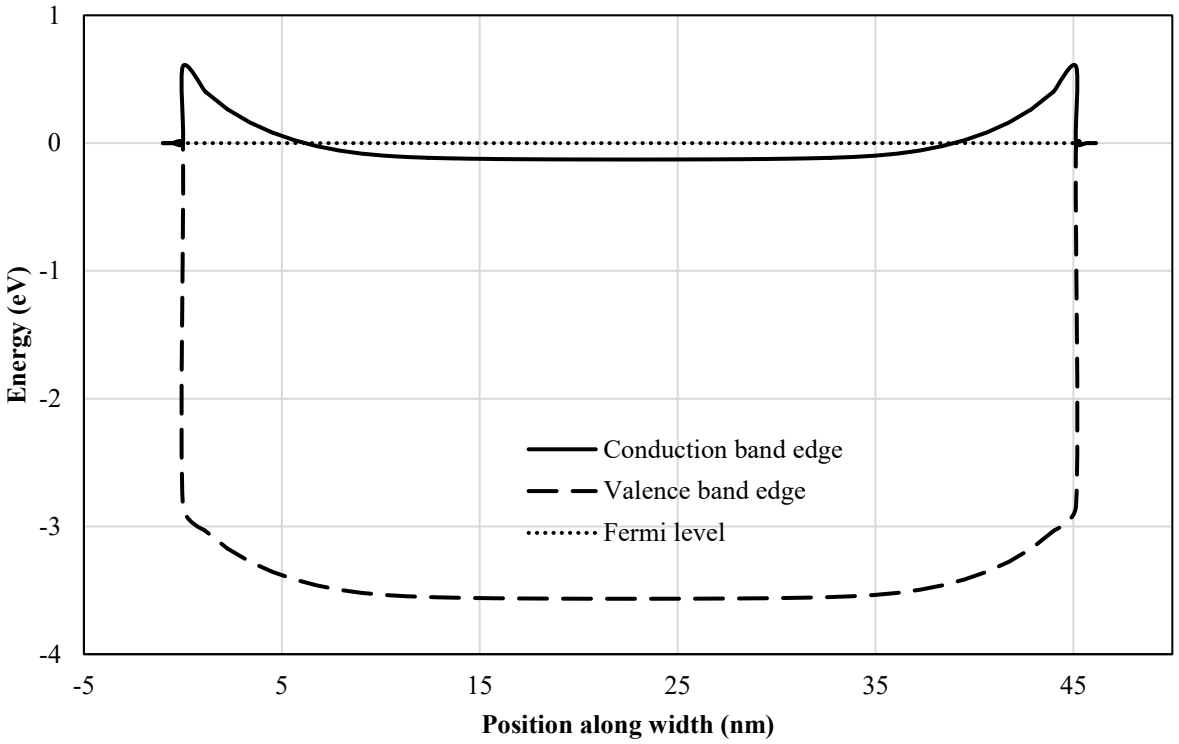

Figure 2.10 – Band diagram for a AlGaN/GaN cylindrical heterostructure whose AlGaN barrier is 20 nm thick and has a 30% aluminum mole fraction. A vertical cut through the mesa is shown with upwards band bending at the sidewalls.

Chapter 3

Nextnano: principles of simulation

This chapter provides insight into the assumptions, principles of calculation, with special attention to strain calculation, and the structure of the codes in *nextnano*, which is the simulation package employed in performing the analyses reported in this thesis.

3.1 Using the software

The *nextnano*^{3} environment (version 3.1.0.0) was used to perform all the simulations that are to follow in this thesis [42]. Another environment, known as *nextnano*++, also exists. Simulation of ternary or quaternary alloys are more efficiently performed in this environment. This is since in nextnano++ materials are more effortlessly combined. However, the material parameters and some boundary conditions were easier to set in *nextnano*^{3}, hence the preference for this version.

In the works reported in this thesis, this simulation package was adopted since it can handle calculation of piezoelectric charges based on realistic strain calculation algorithms with a focus on nanostructures. The package also differentiates between zinc blende and wurtzite crystalline forms. Another advantage in adopting this package is that the only other significant theoretical attempt towards understanding the correlation between mesa geometry and piezoelectric polarization in

III-nitrides HFETs was also performed in the same environment [27], allowing for an easy assessment of the results. Based on this prior work, this thesis via extending to three-dimensional version of simulations leads to a number of novel discoveries.

To start a simulation with *nextnano*, one needs to write an input file. The input file allows the user to define the structure of the device, the applied bias, the doping, the materials used, and their parameters. The gridding mesh for discrete numerical calculations is also defined in the input file. *nextnano* allows the user to choose which regions are subject to quantum calculations. This choice is made to reduce the time required for calculations. The input file serves as an executable for extracting: electron wave functions, space charges, strain, current, and band structure.

To better describe an input file, Figure 3.1 shows the typical structure of such a code. In a given code, words preceded with a percentage sign serve as global variables. For example, in the code shown in Figure 3.1, the variable called "Ignore2DHG" is reused a few times in the body of the program to activate (or deactivate in this case) the quantum region that would be needed in case a two-dimensional hole gas (2DHG) is expected. The quantum computations in this region are turned off if a 2DHG is not expected in order to speed up the calculations. The variable "GaNClusterNumbers" stores the cluster numbers[10] that are devoted to GaN material. It is possible to define them as global variables. Then, "AlloyContent" is more of a traditional variable as one would use in a typical programming language. This variable can be affected by the statement "AlloySweepActive" that triggers a sweep through predefined values. This is like a for-loop. One such a loop is shown in Figure 3.2 (whose parameters are given by "alloy-sweep-step-size" and "alloy-sweep-number-of-steps").

[10] Regions can be clustered into bigger objects by attributing to them a cluster region number. Particular conditions can then be applied to a particular cluster.

```
!+++++++++++++++++++++++++++++++++++++++++++++++++++++++++++++++++++
! For simulations without GaN cap layer
!+++++++++++++++++++++++++++++++++++++++++++++++++++++++++++++++++++
 %Ignore2DHG                          = yes
 %GaNClusterNumbers                   = 4 5
 %AirRegionNumbers                    =     6 7 8
!%AirSidesRegionNumbers               =         8

! For triple-gate action
!%AirRegionNumbers                    =     6 7 8 9
!%AirGaNContactRegionNumbers          =             10

! Also possible to include a GaN cap layer
!%Ignore2DHG              = no
!%GaNClusterNumbers       = 4 5   7
!%AirRegionNumbers        =     6   8   cluster-number = 7  region-numbers = 7

 %AlloySweepActive        = no

 %AlloyContent            = 0.3
!%AlloyContent            = 0.4

!--------------------
! Layer thicknesses
!--------------------

 %ThicknessGaNcap         =  5.0
 %ThicknessAlGaN          = 30.0
```

Figure 3.1 - Portion of an input file in *nextnano*[3] devoted to global variable definition.

```
$alloy-function

 material-number              = 2
 function-name                = constant
 xalloy                       = %AlloyContent


 alloy-sweep-active           = %AlloySweepActive

 alloy-sweep-step-size        = 0.05d0
 alloy-sweep-number-of-steps  = 8

!alloy-sweep-step-size        = -0.025d0
!alloy-sweep-number-of-steps  = 16

$end_alloy-function
```

Figure 3.2 - Example of a structure in a *nextnano*[3] input file. The keyword, "alloy-function" is completely described using the parameters between the $ symbols.

The *nextnano*[3] is built around keywords. Every keyword (“alloy-function” in this case) is organized per the structure between the “$” signs shown in Figure 3.2, and fully describes one

parameter, (in this case the alloy function of the simulated device). In Figure 3.1, the last few lines allow one to see how the thickness of the AlGaN barrier and GaN cap can be altered throughout the input file with only one change to the variables “ThicknessGaNcap” or “ThicknessAlGaN”.

From Figure 3.1 two variables (i.e. “GaNClusterNumbers” and “AirRegionNumbers”) require some attention. This is provided in Figure 3.3. In this figure, three distinct sections are highlighted, namely “regions”, “region-cluster”, and “material”. The first section (i.e. “regions”) describes the first two building blocks, starting from the top of cuboid geometry of a structure grown along the z-axis. Region number one has the lowest priority, one, meaning it can be overridden by any region of higher priority. Priority is a keyword that allows one to control the characteristics of overlapping regions. This region has a geometry described as a cuboid which extends from coordinate z = 0 to coordinate z = “MiddleAlGaN”, whose name suggests that this region covers the top half of the AlGaN barrier up to the air-AlGaN interface, or in the case of GaN / AlGaN / GaN heterostructures, up to the GaN cap – AlGaN barrier heterointerface. Laterally, the region covers the full extent of the heterostructure region comprised between “xmin” and “xmax” and “ymin” and “ymax” along the x- and y-axes, respectively. The simulation region comprises of everything that is inside the predetermined cuboid limits. Meaning that the simulation region can only have a rectangular prism geometry. The simulation region must encompass completely the simulated heterostructure.

In *nextnano*, each region has to be attributed a cluster number. This is done in the second section of Figure 3.3. The sixth cluster on this list is the only one to which many regions will be assigned. These regions are not part of the HFET and are filled with air, surrounding the heterostructure. In the last section of Figure 3.3, each cluster number is assigned a material.

Figure 3.4 shows other important sections of the input file. The simulation-flow-control, for example, a mandatory keyword in every input file allows one to decide if strain is calculated, if

only the Poisson and current-continuity equations are solved, or if the Schrödinger-Poisson current-continuity equations are solved self-consistently. In the "strain-minimization-model" section, a substrate cluster is identified and the boundary conditions are determined. In the "domain-coordinates" section, the extent of the simulation domain is provided as well as the growth direction. This definition introduces the concept of what will be called "filled" and "unfilled" simulation region. In the first case, the heterostructure boundaries are also the simulation region boundaries and in the second case, the simulation region boundaries are larger than the heterostructure boundaries.

Close to fifty different keywords (like "alloy-function") are available, which allow one to completely describe the structure, the quantum regions, the calculation modes, and the boundary conditions. Of course, setting the proper boundary conditions is pivotal to the accuracy of the results. For a full description of these, the interested reader is referred to the user manual available on the website of *nextnano*[11].

Editing and data analysis is often required to take place on a different platform. Depending on the type of analysis, data manipulation might be required. This is since the data is formatted usually in *AVS/Express* (Advanced Visual Systems software package) and a quick transformation to a more traditional x, y, z, f(x, y, z) format is needed to explore the data in *Origin* or *Matlab*.

The *nextnano* requires the definition of a simulation region. This simulation region must be linear for a one-dimensional simulation, rectangular for a two-dimensional simulation, and cuboidal for a three-dimensional simulation. Also, the simulation region can, either fit exactly the simulated structure or encompass a larger region than the structure. These two characteristics of *nextnano*

[11] Link to important *nextnano*[3] keywords :
http://www.nextnano.com/nextnano3/input_parser/keywords/keywords.htm

impact the way conditions are defined at the sidewalls of the simulated structures. In the case where the structure fills completely the simulation region (this is called “closed simulation region” throughout the thesis), the bands are almost flat throughout the structure, converging to the value determined by the deformation potentials introduced by strain fields. A slight upwards band bending is observed in the case of “closed simulation region” simulations with a difference of about 0.05 eV between the center of the structure and the sidewalls at the peak plane[12]. This difference drops to about 0.01 eV in the horizontal plane 1.5 nm deeper than the peak plane. As will be described later, a problem arises when the simulated structure is not of cuboidal geometry. In these cases, inevitably a portion of the simulation region will not be filled by the simulated structure and the conditions at the sidewalls need to be fixed. In chapters to come, two conditions will be examined: the “open simulation region” and the “fixed Fermi level”. In the former, the bands are like the “closed simulation region” while in the latter case, the conduction band is fixed at a particular level below Fermi level.

[12] This is the horizontal plane in which the electron concentration peaks.

```
$regions
 region-number = 1    base-geometry = cuboid  region-priority = 1
 z-coordinates = 0d0    %MiddleAlGaN
 x-coordinates = %xmin %xmax
 y-coordinates = %ymin %ymax

 region-number = 2    base-geometry = cuboid region-priority = 1
 z-coordinates = %MiddleAlGaN    %QRLeft_2DEG
 x-coordinates = %xmin %xmax
 y-coordinates = %ymin %ymax

[...]

$end_regions

$region-cluster
 cluster-number = 1    region-numbers = 1
 cluster-number = 2    region-numbers = 2
 cluster-number = 3    region-numbers = 3
 cluster-number = 4    region-numbers = 4
 cluster-number = 5    region-numbers = 5
 cluster-number = 6    region-numbers = %AirRegionNumbers
$end_region-cluster

$material

 material-number = 1
 material-name   = GaN
 cluster-numbers = %GaNClusterNumbers

 material-number = 2
 material-name   = Al(x)Ga(1-x)N
 cluster-numbers = 1 2 3
 alloy-function  = constant

 material-number = 3
 material-name   = Air-wz
 cluster-numbers = 6
$end_material
```

Figure 3.3 – Another example of a structure in a *nextnano*[3] input file. The above code determines the extent of the simulation region, its structure and composition.

```
$simulation-flow-control
!flow-scheme          = 0
 flow-scheme          = 2
!flow-scheme          = 3
!strain-calculation   = no-strain
!strain-calculation   = homogeneous-strain
 strain-calculation   = strain-minimization-new
$end_simulation-flow-control

$strain-minimization-model
 substrate-cluster-number     = 4
 boundary-condition-x         = Neumann
 boundary-condition-y         = Neumann
 boundary-condition-z         = Neumann
 grown-on-substrate           = yes
$end_strain-minimization-model

$domain-coordinates
 domain-type             = 1 1 1
 x-coordinates           = %xmin %xmax
 y-coordinates           = %ymin %ymax
 z-coordinates           = %zmin %zmax

 hkil-x-direction        =  1  0 -1  0
!hkil-y-direction        = -1  2 -1  0
!hkil-z-direction        =  0  0  0  1
 hkil-z-direction        =  0  0  0 -1

 growth-coordinate-axis = 0 0 1
 pseudomorphic-on        = GaN
$end_domain-coordinates
```

Figure 3.4 – Third example of a structure in a *nextnano*[3] input file. The above code determines the simulation flow, the strain calculation algorithm with the boundary conditions at the sidewalls. It also determines the extent of the simulation region and the crystal growth direction.

3.2 Basic assumptions

In Section 3.1, the keyword simulation-flow-control was quickly alluded to. Setting the *flow-control* enables:

- Strain calculation
- Determination of piezoelectric and pyroelectric charges

- Calculation of the electronic profile in the single-band or multiband k·**p** envelope function approximation
- Solving the relevant Poisson, current-continuity, and Schrödinger equations.

The calculations need to be handled self-consistently. This is since evidently solving for the potential in the charge distribution means incorporating results from the wave functions. Hence, the numerical calculation is done in a closed loop, as shown in Figure 3.5, until the energy converges [43].

It is important to note that all the equations that are to be solved in *nextnano* are partial differential equations (PDEs) in position space. The discretization method chosen is the finite difference, allowing discontinuities in material parameters to be considered easily [44].

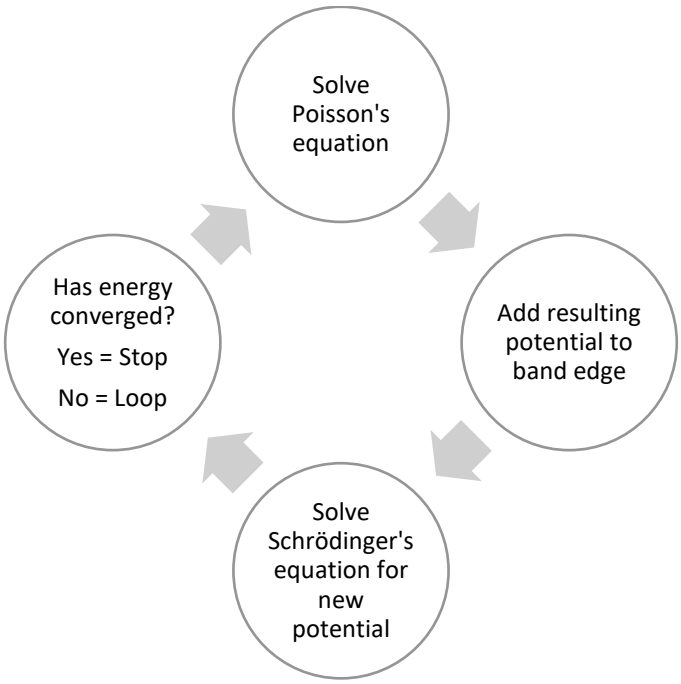

Figure 3.5 - Self-consistent Schrödinger-Poisson solution for the band edge potential. The loop is entered at the "Solve Poisson Equation" step. Figure adapted from [43].

3.2.1 Strain

In *nextnano*, strain is calculated according to the linear continuum elasticity theory [45] [46] [47], which assumes infinitesimal strain[13] and linear stress-strain relationship. Four distinct strain calculation algorithms are available: no-strain, zero-strain-amorphous[14], homogeneous-strain and strain-minimization. As their names suggest, the first two do not involve any strain calculation. In this thesis, since the objective is to study the changes in 2DEG sheet charge density due to strain effects, homogeneous-strain and strain-minimization algorithms are to be used extensively. The former calculates the strain according to the lattice parameters where it is assumed constant throughout the whole region, while the latter minimizes the elastic energy in the structure. A summary of the main characteristics of both algorithms is given in Table 3.1.

[13] The inner displacements are assumed to be much smaller than the dimensions of the body.
[14] Does not take into account strain at all. This is equivalent to *no-strain*. This option has been disabled in the last version of the *nextnano* software.

Table 3.1 - Summary of main characteristics of the most useful strain algorithms in *nextnano*[3].

Strain algorithms	Homogeneous-strain	Strain-minimization (and strain-minimization-new)
How to calculate strain	Applies the same lattice mismatch to the region under strain (appropriate for large pseudomorphically grown epilayers).	Minimizes the elastic energy numerically.
Dimensions	1-D (not recommended for 2-D and 3-D) useful for certain applications, a 1-D well along x-axis, that is homogeneous in (y,z)-plane.	1-D/2-D/3-D
Substrate	Need to specify a substrate that will be unstrained.	Need to specify a substrate that will be unstrained.
Equations	In the crystal coordinate system, the deformation of the unit cell of the strained layer is fixed.	For mechanical equilibrium, the elastic energy density is minimized leading to the derivative of the stress tensor being zero. The unit cell of the strained materials is allowed to deform along all three spatial directions to minimize the elastic energy with respect to the unstrained substrate.
Deformation of unit cell	Deformation in the strained layer is fixed along two spatial directions (according to the growth conditions).	Deformation is allowed along all directions to minimize the elastic energy with respect to the substrate.
Specific strain boundary conditions (BCs)	No control	One of the following two boundary conditions can be set for any direction. Neumann BCs: no external forces acting on the sample – sets the derivative of sigma (stress tensor) to zero at boundaries. Periodic: Only used in the case of superlattices simulations in 3-D.

The software assumes pseudomorphic growth at the heterointerfaces. It also neglects lattice defects. In terms of the strain minimization, all atoms are first placed at the equilibrium positions of the lattice, then they are allowed to relax by energy minimization in the growth direction [45]. In the context of numerical simulations, it would be more exact to talk about material grid points instead of atoms because of the discretized nature of the material grid. This process is illustrated in Figure

3.6. Deformations caused in the crystal by the nonuniform displacements are described by a distortion tensor:

$$g_{ij} = \frac{\partial v_i}{\partial x_j} \quad (i,j = 1,2,3) \tag{3.1}$$

where $v(x) = x'(x) - x$ is a field of displacement vectors. This distortion tensor can be split into a symmetric (i.e. strain tensor described as: $\varepsilon_{ij} = 1/2\,(g_{ij} + g_{ji})$) and an asymmetric part. Since the asymmetric part only describes rotations of the crystal, it does not contribute to the elastic energy written as:

$$E = \frac{1}{2}\int_V K_{ijkl} g_{ij} g_{kl} dV \qquad (i,j,k,l = 1,2,3) \tag{3.2}$$

where K_{ijkl} is the fourth rank elasticity tensor.

To obtain a condition for mechanical equilibrium, the elastic energy is to be minimized. When the external volume forces **f** are included, this leads to:

$$\frac{\partial \eta_{kl}}{\partial x_l} = f_k \tag{3.3}$$

where $\eta_{kl} = K_{klij}\varepsilon_{ij}$ is the linear approximation of the Cauchy stress tensor. To solve equation (3.3), one applies, as mentioned in Table 3.1, Neumann or periodic boundary conditions to the borders of the simulation domain and assumes a completely unstrained substrate area. These assumptions lead to a solution of (3.3) that gives the displacement vectors relative to the reference substrate lattice $\overline{\boldsymbol{v}}(x)$ yielding the total strain tensor:

$$\varepsilon_{ij} = \frac{1}{2}\left(\frac{\partial \overline{v_i}}{\partial x_j} + \frac{\partial \overline{v_j}}{\partial x_i}\right) + \delta_{ij}\frac{a_i^s - a_i}{a_i}. \tag{3.4}$$

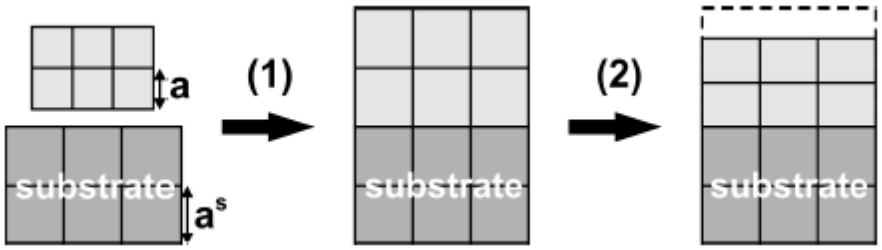

Figure 3.6 – Illustration of the strain calculation process in *nextnano*[3]. First, the material grown epitaxially is adjusted to the substrate's lateral lattice constant and then it relaxes by energy minimization scheme. Source: [45].

3.2.2 Quantum physics

In *nextnano*[3], the global electronic structure is calculated in terms of the **k**·**p**[15] envelope function approximation[16]. In the single-band approximation, one thus wishes to solve the time-independent Schrödinger equation for electrons. In one-dimension, this is:

$$-\frac{\hbar^2}{2m^*}\frac{\partial^2}{\partial x^2}\psi(x) + V(x)\psi(x) = E\psi(x) \tag{3.5}$$

where m^* is the electron effective mass (considering the longitudinal and transverse directions) in the material and $V(x)$ stems from the difference in bandgaps across the heterojunction. Without going through all the derivations involved in the **k**·**p** Hamiltonian[17] of the wurtzite structure, it suffices to indicate that in the effective-mass approximation, the single-band Hamiltonian is:

[15] The **k**·**p** approximation relies on the fact that, in many cases, the parameters of a semiconductor are well described by the position and shape at the extremum points of the conduction and valence bands in the E-**k** diagram. This approximation allows one to calculate the relation between the wavevector **k** and the energy of the state, $E_{n,\mathbf{k}}$ also known as the band dispersion.

[16] For heterojunctions, the envelope function approximation signifies that the heterojunction can be described by a potential that originates from the difference between the bandgaps of the materials [43]. Also, the envelope function is slowly varying compared to the lattice constant. The envelope function approximation makes use of Bloch functions.

[17] The Hamiltonian corresponds to the total energy of the quantum system. It allows for a very compact version of the Schrödinger equation.

$$H(\mathbf{k}) = E^{\Gamma} + \frac{\hbar^2}{2m^*}\mathbf{k}\cdot\mathbf{k}^{\mathrm{T}}. \tag{3.6}$$

This is evaluated at the Γ-point ($\mathbf{k_0} = 0$). Even though the 8-band **k·p** model gives more accurate results, the single-band model was used throughout the thesis. This is since this approximation has been proven accurate enough in the case of wide band gap semiconductors when hot-carriers and high electric fields are not considered [45]. This approximation also allows conserving of the computational time. The 8-band **k·p** model is an extension of the 4-band **k·p** model, where spin-orbit coupling is considered [48]. In the 4-band model, coupling between one conduction band and the three valence bands is considered.

In *nextnano*[3], the potential $V(x)$ in equation (3.5) is shaped by the discontinuities in the band diagram, local excess charges, and external electric fields[18]. Regarding this situation, the charge-density ρ(x) is expressed as:

$$\rho(x) = q[p(x) - n(x) + N_D^+(x) - N_A^-(x) + \rho_{\mathrm{pol}}(x) + \rho_{\mathrm{fixed}}(x)] \tag{3.7}$$

where, $p(x)$ and $n(x)$ are the concentration of holes and electrons, and $N_D^+(x)$ and $N_A^-(x)$ represent the concentration of ionized donors and acceptors, respectively. $\rho_{\mathrm{pol}}(x)$ and $\rho_{\mathrm{fixed}}(x)$ represent the concentration of polarization and fixed charges.

As mentioned earlier, *nextnano*[3] considers two different types of regions in the structure: the *quantum-mechanical* region and the *classical* region. These regions must be clearly identified in the input file. This is because between the two, different computational schemes are used. In classical regions, a Thomas-Fermi approximation is used [20] [49]. The Thomas-Fermi model

[18] Neglecting exchange-correlation potential.

provides approximations to the calculation of the total energy and makes the following assumptions: (i) relativity corrections can be neglected, (ii) the potential, V, in the atom is solely dependent on the distance *r* from the nucleus, (iii) electrons are distributed uniformly in a six-dimensional phase space, and (iv) the potential V is determined by the nuclear charge and the distribution of electrons. This model served as a development basis for a more accurate model, the density functional theory (DFT). In the quantum-mechanical region, however, the charge density for electrons is given, for a *d*-dimensional structure (*d* = 1, 2, 3), based on the **k·p** method single-band approach[19]:

$$n_{qm}^{\mathrm{EMA}}(x) = \sum_{i \in \mathrm{CB}} g N_i^{(3-d)}(T) |F_i(x,0)|^2 \, \mathcal{F}_{(1-d)/2}\left(\frac{-E_i(0) + E_{F,n}(x)}{k_B T}\right) \tag{3.8}$$

where, g accounts for spin and valley degeneracies, the factor i runs over all states in the conduction band, where F_i's are the envelope function expansion coefficients and the $\mathcal{F}_n(E)$ is the Fermi-Dirac integral of the n-th order:

$$\mathcal{F}_n(E) = \frac{1}{\Gamma(n+1)} \int_0^\infty \frac{\zeta^n}{\exp(\zeta - E) + 1} d\zeta. \tag{3.9}$$

Finally, the charge density from equation (3.7) gives rise to an electrostatic potential $\phi(x)$ that is calculated by the Poisson's equation:

$$\nabla^2 \phi(x) = -\frac{\rho(x)}{\epsilon}. \tag{3.10}$$

This electrostatic potential needs to be included in the envelope function Hamiltonian in the form of the Hartree potential [45]:

[19] A similar equation exists for holes in the *d*-dimensional structure. EMA stands for the effective mass approximation.

$$V(x) = V_H(x) = -q\phi(x). \tag{3.11}$$

3.2.3 Surface state density

As seen in Section 2.4, surface states are often taken as the source of electrons in the 2DEG of polar AlGaN/GaN heterostructures. The potential barrier formed at the semiconductor surface is in *nextnano*[3] assimilated to a Schottky barrier and can be interpreted by the Fermi level pinning of the conduction band. In mathematical terms, the Schottky barrier sets a Dirichlet boundary condition. In this environment, one could also set an ohmic contact (a Neumann boundary condition) at the source or drain regions. Here, it is possible to define a fixed surface charge density, but fixing the value of the conduction band at the boundary with a Schottky barrier makes it easier when changing parameters in the input file. It is important to note that, as shown by Lymperakis *et al.* in [50], all non-polar surfaces of GaN and AlN are intrinsically pinned[20], thus affecting the potential in the structure.

[20] This is reported in the wurtzite form. The study was performed using nanowires.

Chapter 4

Study of electron profile at AlGaN/GaN heterojunctions through the one- and two-dimensional simulations

The first two sections of this chapter describe the device structure and propose a method to evaluate the accuracy of computations in terms of the number of calculated eigenvalues. The remaining sections deal with analysis of the observations. One of the goals of this chapter is to reproduce the results from the prior published work, mostly Jogai [35] and Alsharef *et al.* [27], whose approaches to study the electron population at the AlGaN/GaN heterojunctions were based on one- and two-dimensional simulations.

4.1 Device structure

The simplest layer structure of an $Al_xGa_{1-x}N$/GaN HFET is shown in Figure 4.1. In this structure, a Schottky contact is defined on the top of the AlGaN barrier[21]. In the reported simulations of this chapter, the epilayer is assumed to be grown in the [0001] direction and the GaN buffer is

[21] Since the goal of this thesis is to study the electron population at AlGaN/GaN heterojunctions, to simplify the matter the top surface is assumed to be fully covered by this Schottky contact (i.e. without appreciating the source and drain ohmic contacts).

considered completely relaxed. In here, a buffer thickness of 300 nm is considered. This value is within the range of usual mesa height in a physical device. This epilayer is assumed to be undoped, a simplification that is also found in [27]. In the two-dimensional simulations, the sides of this structure are subject to Dirichlet boundary conditions (meaning the wave-function to be zero at the boundary). In the simulations to be reported, the lattice temperature is set to 300K.

In these simulations, according to the finite-difference method, a rectilinear grid is defined, which is denser in regions of interests (i.e. to reduce the total number of grid points). The regions of higher interest are the barrier and the section of the GaN buffer close to the heterointerface[22]. These regions are defined as specific regions, as per the code shown in Figure 3.3. Also, throughout this chapter, it is understood that the heterostructure fills completely the simulation region, thus giving rise to a "closed simulation region" as defined in section 3.1.

In the one-dimensional version of simulations, the only option for incorporation of strain is *homogeneous-strain*, (i.e. while the strain minimization scheme is not available). In the two-dimensional version, both strain algorithms: *homogeneous-strain* and *strain-minimization* are available.

[22] This is due to stronger spatial variation of the electric field and the electron population.

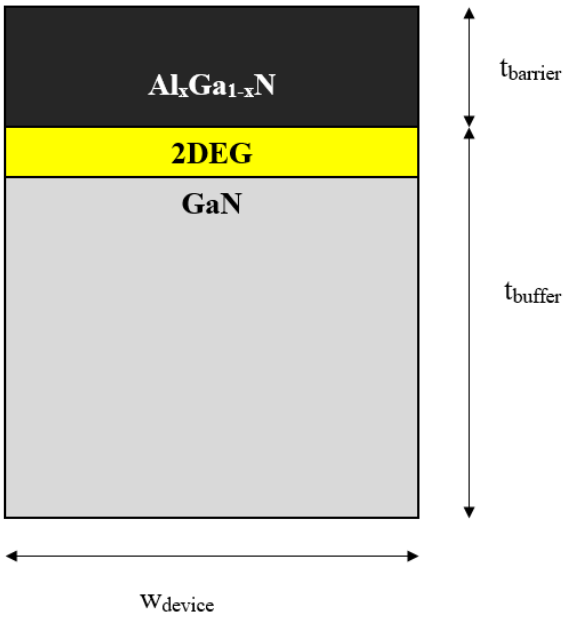

Figure 4.1 – Cross section of a simulated device structure in *nextnano*[3]. A GaN buffer in which a 2DEG forms is topped by an AlGaN barrier. The device width can be adjusted. The one-dimensional simulation is based on a normal cut to the heterointerface of this structure.

4.2 Accuracy of simulation and the selection of the required number of eigenvalues

The number of calculated eigenvalues impacts the degree of accuracy in the calculation of the electron distribution. The metric of accuracy is defined based on the change in the electron concentration with respect to the number of calculated eigenvalues, with respect to which a tentative demarcation is proposed in subsection 4.2.2. Within the keyword section "quantum-model-electrons", *nextnano*[3] requires the definition of the calculated number of eigenvalues per band. To provide a ballpark number, in the one-dimensional simulations reported by Jogai [35] the contributions from 25 electron subbands and 70 hole subbands were considered. Since in the work presented in this thesis the structures were simulated not only in one but also in two and three dimensions, the required number of calculated eigenvalues per band needed to be diligently

adjusted. In the following two subsections, the employed procedure for determining this number for each version of simulation is explained.

4.2.1 Selection of the number of eigenvalues for the one-dimensional version of simulations

As an example, in case of the one-dimensional simulation, a homogeneous 20 nm thick $Al_{0.3}Ga_{0.7}N$ barrier on an unstrained buffer is considered. In Figure 4.2, the calculated electron concentration by *nextnano*[3] is shown for each of the first three subbands. Considering the summation of the 25 conduction band eigenstates, integrating the electron concentration profile normal to the heterointerface produces the $1.179 \times 10^{13}\ \mathrm{cm}^{-2}$ value of sheet charge density. Figure 4.2 shows that the contributions from the third subbands and beyond are negligible [51]. Figure 4.3 illustrates this fact in a different fashion. In this figure, the energy of the first five subbands and their relative importance with respect to the sheet charge density are shown. On this basis, one notices that the third eigenstate makes up only 2.23189% of the total electron density, while the tenth eigenstate is responsible for less than 0.00005% of the total. Thus, for one dimensional simulations, considering 25 eigenstates is more than enough. However, this number is kept at 25 to provide a fair comparison to the results presented in [35], whereas the computation time for the one-dimensional simulations was not an issue.

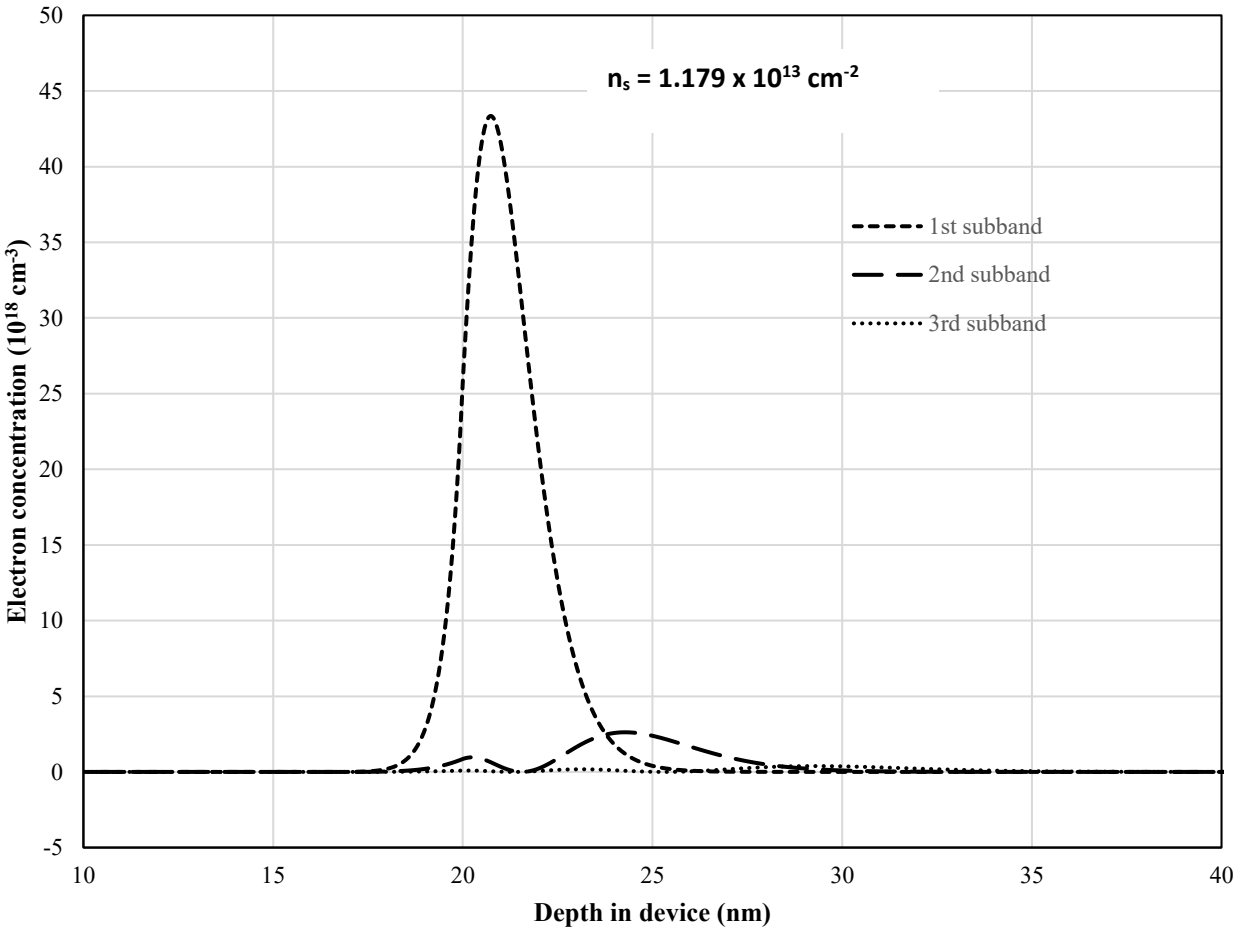

Figure 4.2 - Electron concentration for the first three calculated subbands (eigenstates), in units of 10^{18} cm^{-3}, as a function of device depth for a one-dimensional simulation.

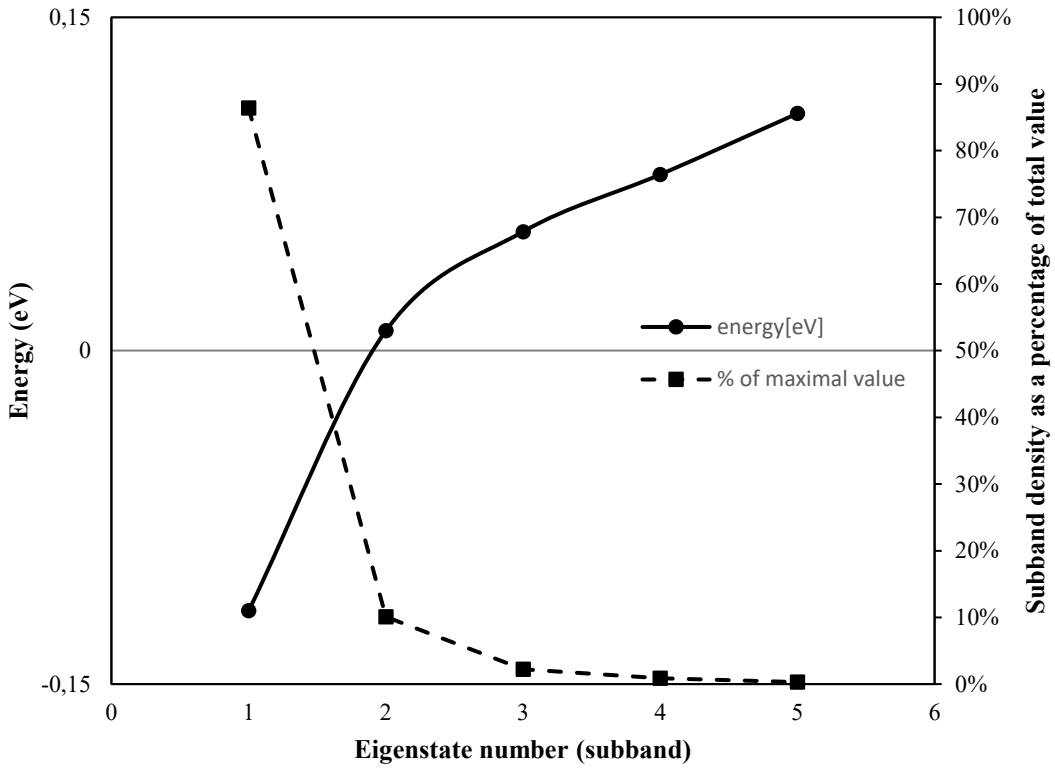

Figure 4.3 - Subband energy (left axis) and eigenstate density (as a percent of the total sheet charge density (n_s) – right axis) versus the eigenstate number. The grey line at $E = 0$ represents the Fermi level.

4.2.2 Number of eigenvalues for simulations of two- and three-dimensional structures

In simulating the higher dimensional structures, the process presented above is repeated. In the 2-D and 3-D versions, simulations are extended along the width from Figure 4.1 and normal to the cross-section of the epilayer. Reaching for wider and deeper devices requires the calculation of more eigenstates. This is shown in Figure 4.4, where the subband density as a percentage of the total value is plotted against the number of calculated eigenstates for various mesa widths in the simulation of two-dimensional structures[23] subject to the strain minimization algorithm. Based on

[23] Other parameters are: 30% aluminum mole fraction, 20 nm AlGaN barrier thickness and a Schottky barrier height of 1.23 eV.

this, the above-mentioned trend is clear. In Figure 4.5, the number of eigenstates required to reach a density that would be less than 0.05% of the first subband is calculated. This is a tentative demarcation value in a compromise between computation time and accuracy. In here, the same procedure is applied to three-dimensional simulations. In this case, a cube whose lateral sides are of equal length is simulated. In the three-dimensional simulations, one should notice how quickly the number of required eigenstates rises. Based on these assessments, the trends displayed in Figure 4.5 served as inputs to our *nextnano*^{3} simulations for all the device structures presented in this thesis. In 2-D, the number of required eigenvalues increased with the width of the device, W, in a linear fashion, while in three-dimensional structures, (a simple cube for example) the trend is more like W^2. As the size of the structure increases, the number of grid points inevitably increases as well and requiring the calculation of a higher number of eigenstates.

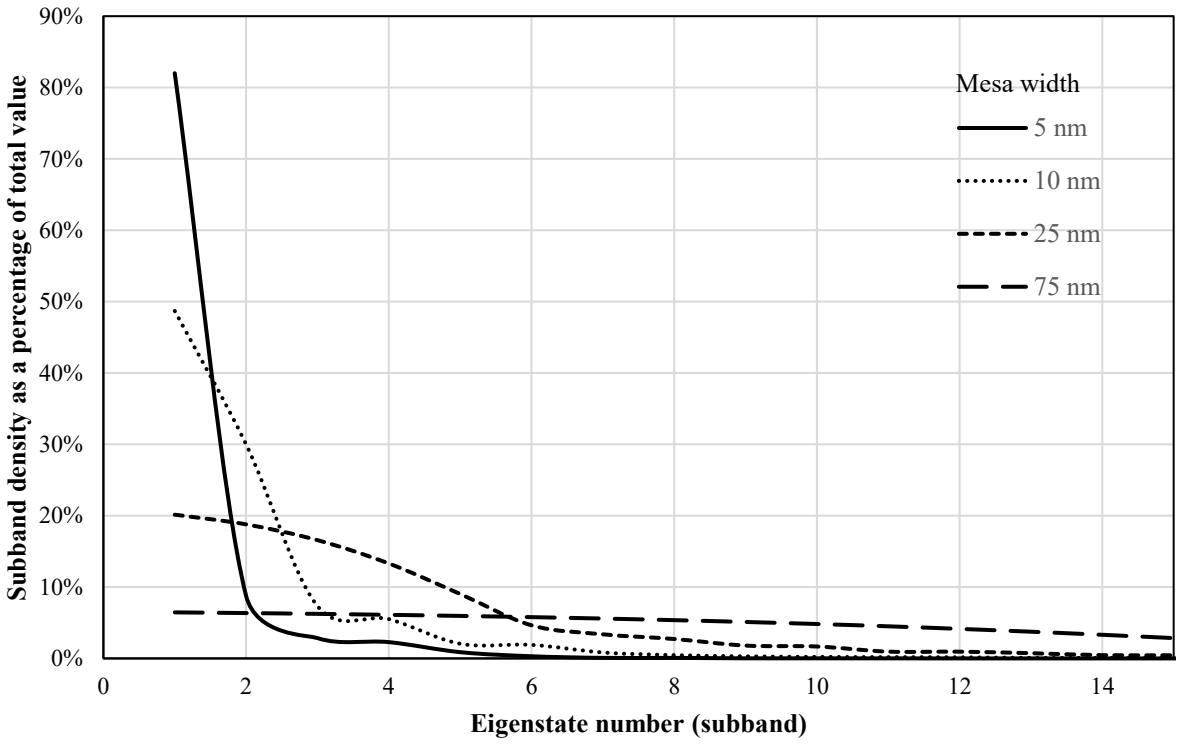

Figure 4.4 – Subband density as a percentage of the total value versus the eigenstate number for two-dimensional version of simulation of a typical AlGaN/GaN HFET of varying width.

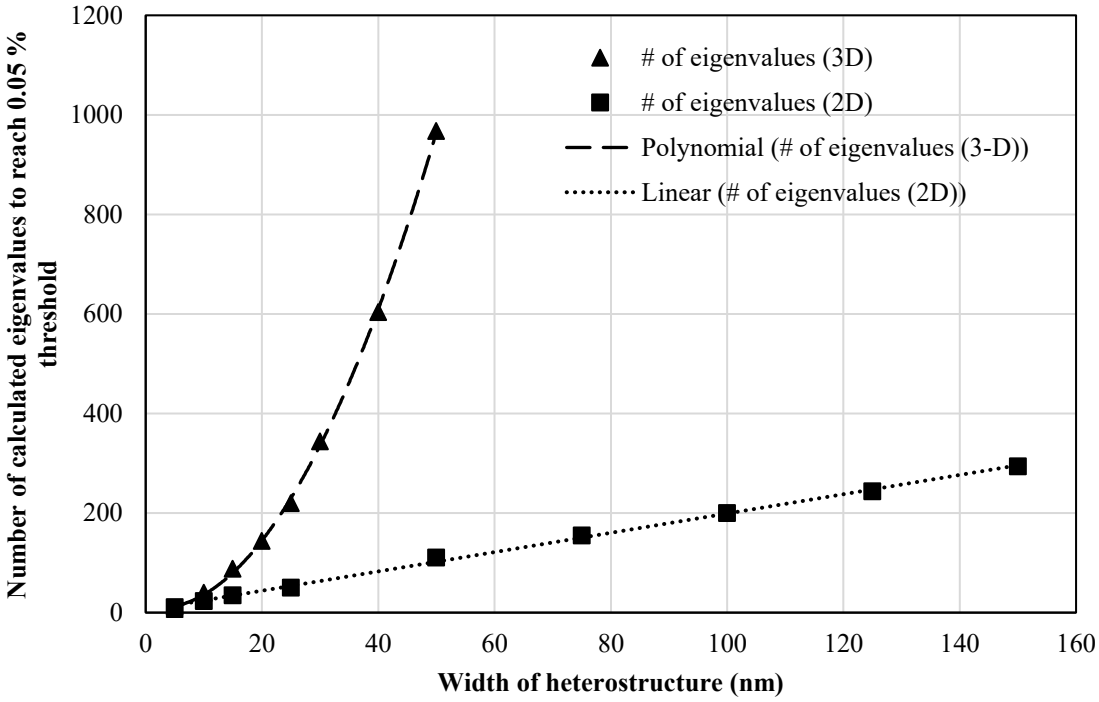

Figure 4.5 - Number of calculated eigenvalues needed to reach the 0.05% threshold as a function of the structure size.

4.3 Wave function solutions and energy levels in 1-D and 2-D simulations

Taking an arbitrary position along the width in the structure presented in Figure 4.1 yields a one-dimensional prototype model for an AlGaN/GaN device. All the simulations presented in this thesis use the parameters presented in Chapter 3. Considering the trends from Figure 4.3, one-dimensional Ga-face undoped HFET structures with barrier thicknesses varying between 6 and 40 nm are simulated. At the barrier / air boundary, the *nextnano*^{3} software offers different ways of handling the interface. The choice made in here, as is common in several *nextnano*^{3} template files [52] [53], is a Schottky contact boundary condition with a Schottky barrier height given by equation (2.14). Figure 4.6 shows an example output for one of these simulations on an AlGaN/GaN mesa whose barrier is 22 nm thick, which boasts an aluminum mole fraction of 30%. In this figure, the Γ conduction band edge is shown as well as one of the valence band edges (i.e.

heavy hole band). On this figure, the electron concentration (in 10^{18} cm^{-3}) is also plotted versus the depth normal to the heterointerface with a peak just below the AlGaN / GaN interface.

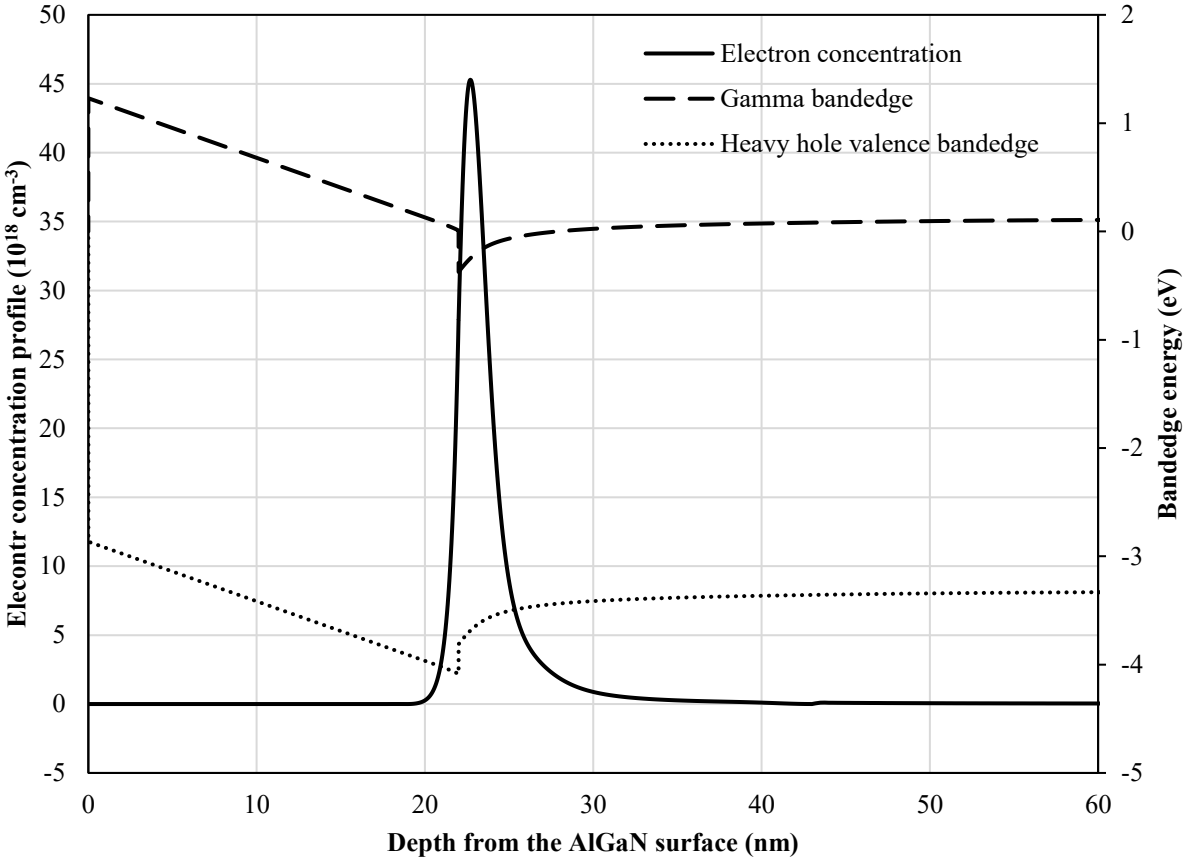

Figure 4.6 - Gamma conduction and heavy hole valence band edges with electron concentration in the quantum well for a one-dimensional $Al_{0.30}Ga_{0.70}N$/GaN structure with 22 nm thick barrier employing the homogeneous strain algorithm.

As already mentioned, the electrons accumulate at the heterointerface because of the discontinuity in the spontaneous polarization and the bandgap, in addition to the presence of piezoelectric polarization. In light of the presence of a quantum well, it is clear from Figure 4.6 that the region of GaN close to the heterointerface must be identified as a quantum mechanical region in *nextnano*[3]. Through these quantum simulations, it is possible to extract the levels of all subbands and the probability density function stemming from the wave function. For the example of Figure 4.6, this

is shown in Figure 4.7, where the probability densities are normalized and shifted with respect to their eigenvalues. In these simulations, the so-called quantum region spanned the interval of 19 to 43 nm from the AlGaN surface.

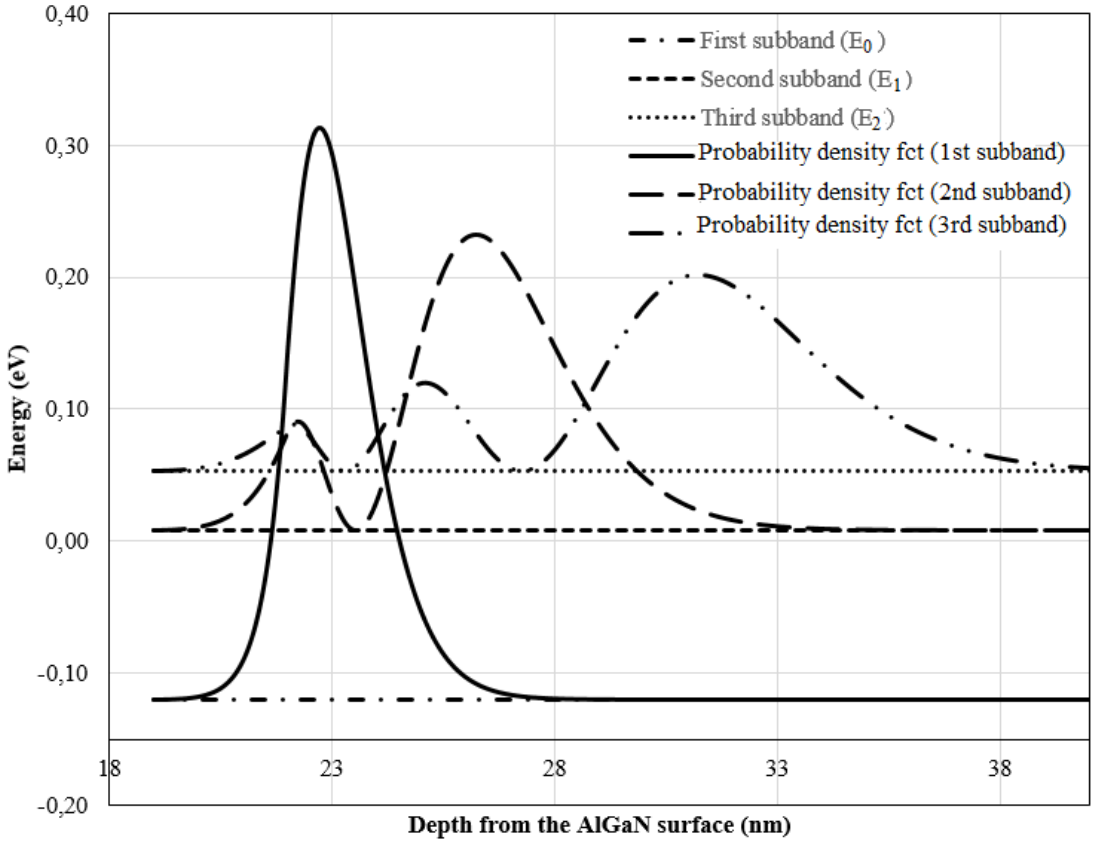

Figure 4.7- Energy levels and probability density functions (shifted with respect to the eigenvalue energy level) for the three lowest subbands of a 22 nm thick barrier $Al_{0.30}Ga_{0.70}N$ / GaN undoped HFET simulated in 1-D using homogeneous strain algorithm. The Fermi level is set at 0 eV.

Extending the simulations to 2-D, employing *nextnano*, Alsharef *et al.* have already reported on the differences between the results obtained with and without considering the quantum effect in triple-gated AlGaN/GaN HFETs (i.e. with tangible side-gating due to the small width of the mesa) [27]. In these studies, quantum mechanical based simulations predicted a lower sheet charge density and a more positive threshold voltage than classical simulations[24]. Since the *nextnano*[3]

[24] In classical solution, no quantum region, even in the quantum-well, is considered.

package allows for such calculations, similar comparisons are performed here. In Figure 4.8, the variation of the sheet charge density[25] is shown versus the mesa width for a two-dimensional structure (as shown in Figure 4.1). In this figure, one sees that the classically obtained results are slightly above the quantum-mechanically calculated densities. Of course, an expected trend, that also confirms observations by Alsharef *et al.* [27], is the fact that as the width of the device decreases, the difference between the classical and quantum mechanical based calculations becomes more tangible.

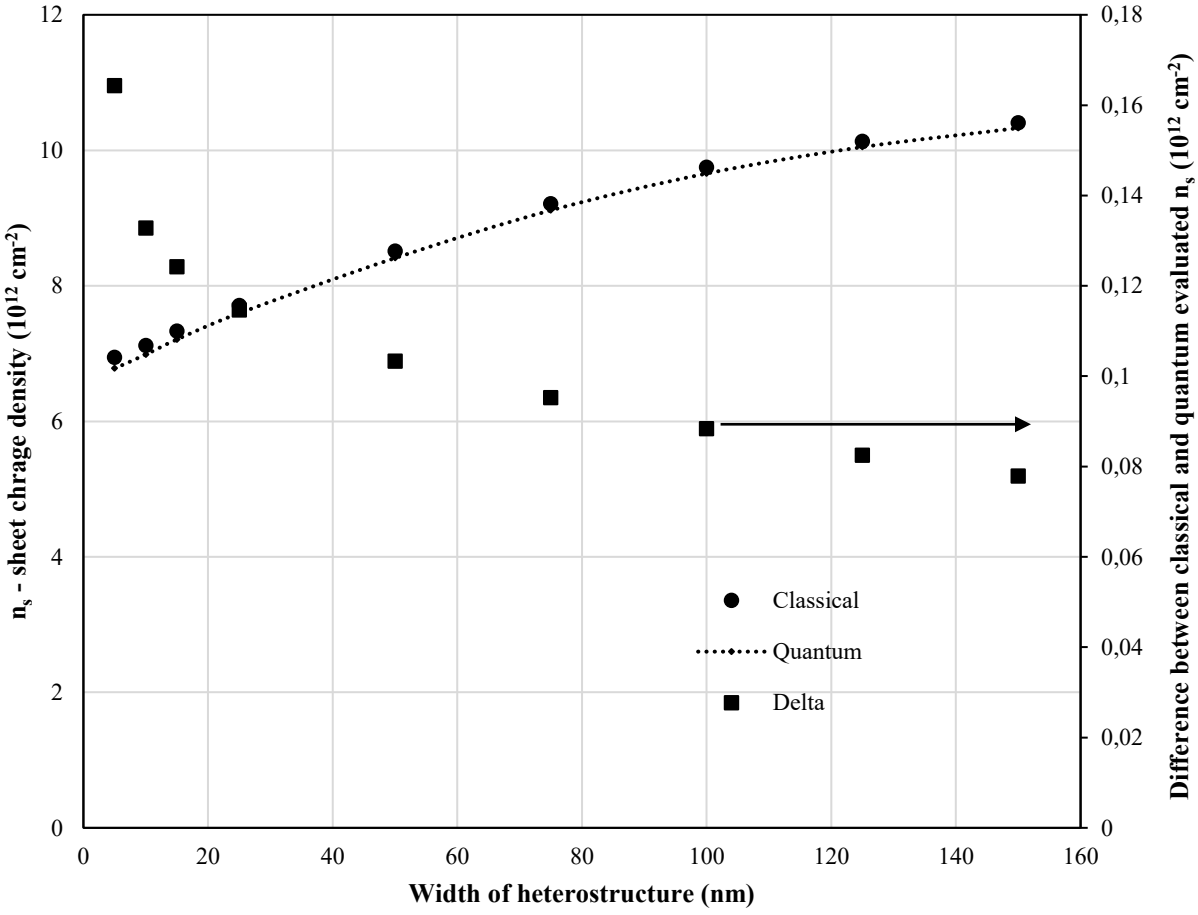

Figure 4.8 - Sheet charge density versus mesa width for two-dimensional simulations of AlGaN/GaN structures under quantum mechanical and classical assumptions for 30% aluminum mole fraction and 22 nm thick barrier. Strain minimization algorithm is used.

[25] To calculate the sheet charge density in this case, we integrated the whole area under the curve for the electron concentration, as given in Figure 4.6.

An even more important part of the reported discrepancy between the two sets of calculations is in the shape of the electron concentration profile. The classical computation does not consider the effect of the AlGaN/GaN heterointerface and gives rise to a carrier concentration that peaks right at the interface. However, in reality the 2DEG peaks slightly away from the heterointerface. This can be seen in Figure 4.9, where the same device has been simulated, once considering quantum mechanical effects (effectively solving the Schrödinger equation) and once by simply solving the Poisson equation. From now on, only quantum mechanical simulations are to be considered.

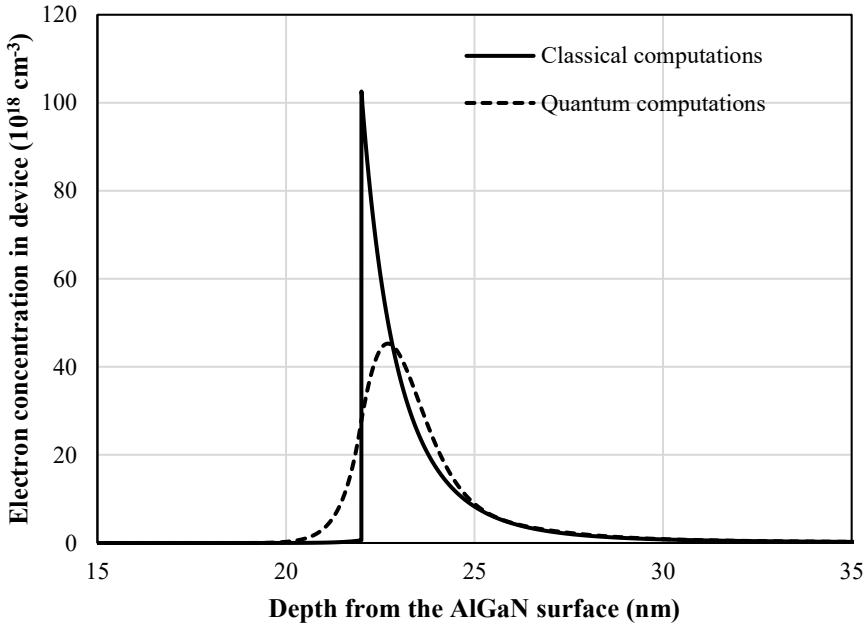

Figure 4.9 - Comparison between classical and quantum based calculations of the electron concentration profile in simulations of an $Al_{0.30}Ga_{0.70}N$ / GaN structure with 22 nm AlGaN barrier thickness.

4.4 Strain evaluation

As indicated earlier, the *nextnano*[3] environment allows the computation of the mechanical strain and verifying its impact on electron concentration based on the first order principles. As a result,

unlike some of the competing simulation environments in employing *nextnano*[3] there is no need to introduce a sheet of charges to mimic the influence of the polarization. In this section, a survey of the "homogeneous-strain" and "minimized-strain" algorithms is provided via comparing their influence on the electron concentration.

As an example, looking at Figure 4.10 one sees the impact of the application of different strain algorithms on the calculated electron concentration in a 2-D simulation of an $Al_{0.3}Ga_{0.7}N/GaN$ HFET mesa of width equal to 25 nm. The per unit-area peak of the carrier concentration for homogeneous-strain algorithm ($n_{s_{homogeneous\ strain}} = 1.0278 \times 10^{13}\ \mathrm{cm}^{-2}$) is observed to be 1.59 times the peak calculated according to the elastic energy minimization algorithm (giving $n_{s_{minimized\ strain}} = 6.4239 \times 10^{12}\ \mathrm{cm}^{-2}$). In addition, it is observed that the difference is even more pronounced near the edges. The inset of Figure 4.10 shows the calculated electron concentrations along the width of the 25 nm wide mesa. The reported slices are taken along the width of the mesa at two different locations: in the middle (x = 12.5 nm) and near the sides (x = 3 nm). In absence of the consideration of a side gate, the electron concentration lowering proposed by the strain-minimization algorithm near the sides of the mesa results from the trends shown in Figure 4.11. This figure shows a flat elastic energy density in the case of the homogeneous strain algorithm evaluation, whereas the energy density resulting from the strain minimization algorithm is shown to lower gradually towards the middle of the mesa while peaking at the heterojunction, especially near the sides.

This non-uniform stress field in the AlGaN was for the first time reported by Mastro *et al*. [54]. They showed that large strain fields altered the electron concentration profiles. In Figure 4.11, the elastic energy density is $0.15824\ \mathrm{eV/nm^3}$ for the simulated heterostructure under homogeneous strain calculation and reaches to $0.15829\ \mathrm{eV/nm^3}$ in the middle of the heterostructure simulated

under the strain-minimization algorithm. This value decreases as one gets further away from the heterointerface.

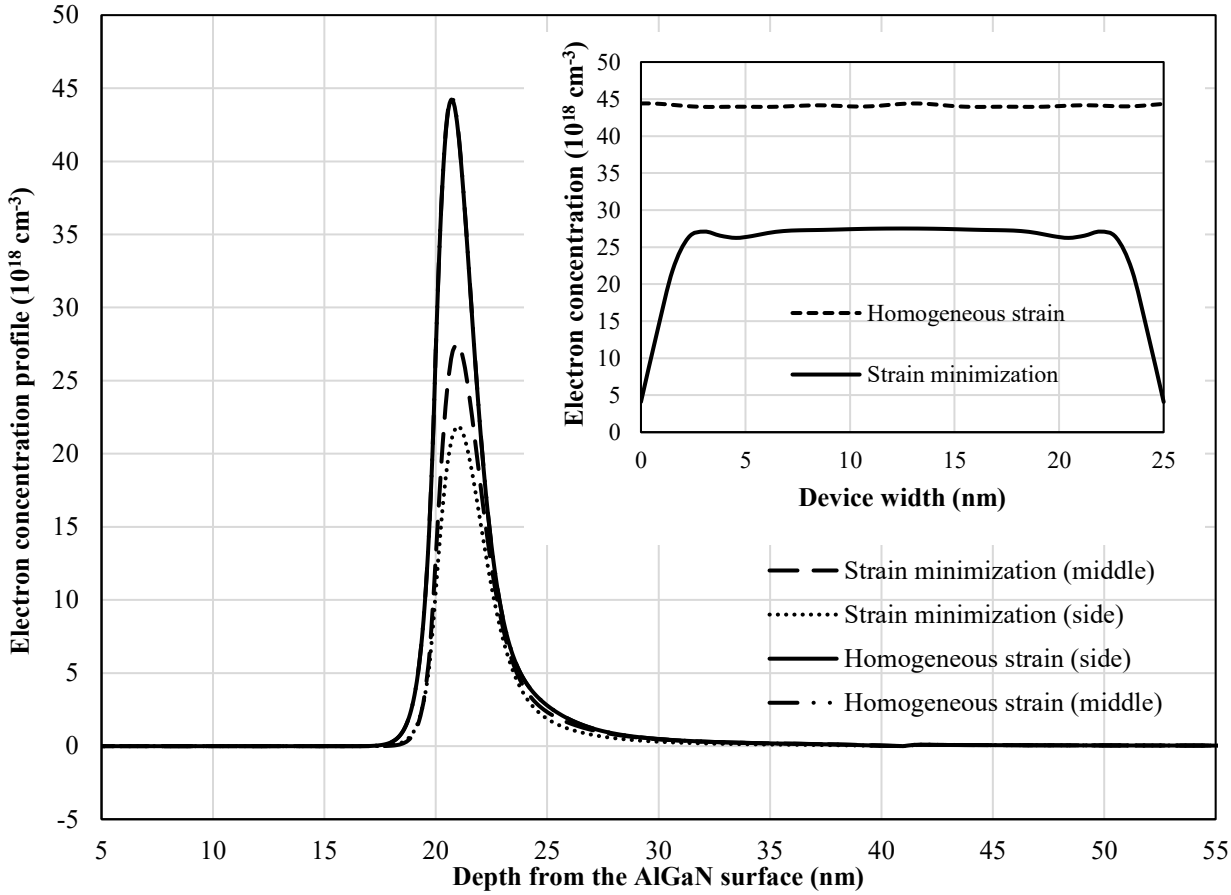

Figure 4.10 – 2-D evaluated electron concentration in AlGaN/GaN structures plotted at different slices of an $Al_{0.3}Ga_{0.7}N$/GaN HFET on a 25 nm wide mesa (middle, x=12.5 nm and side, x=3 nm) using strain minimization and homogeneous strain algorithms. Both homogeneous strain curves overlap. The inset shows the electron concentration (in 10^{18} cm^{-3}) versus width for the peak concentration. Barrier thickness is 20 nm and the structure is simulated under closed simulation region assumptions.

In Figure 4.12, the hydrostatic strain for the strain-minimized structure is plotted. This is the trace of the strain tensor. Again, one observes the spikes at the sidewalls and near the heterojunction. This influences the piezoelectric polarization, which in turn affects the electron concentration at these locations. Similar patterns were also visible in other works involving determination of strain fields in AlGaN/GaN heterostructures [55] [56] [57] [58].

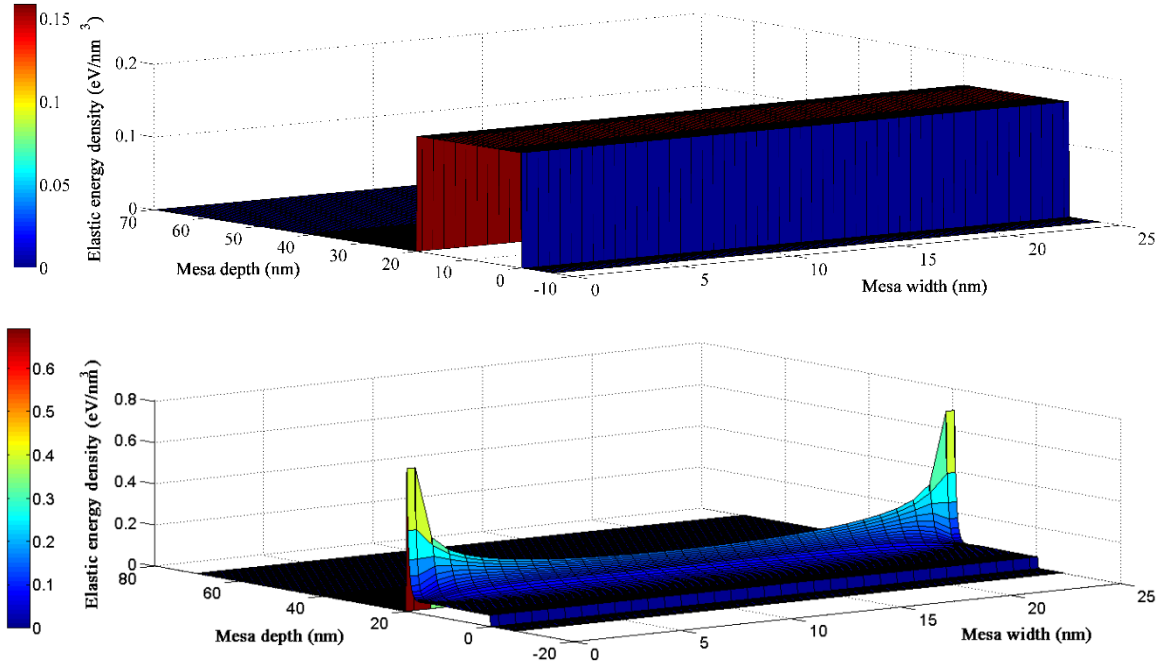

Figure 4.11 - Energy density (in eV/nm^3) of the elastic deformation for (top) homogeneously strained structure and (bottom) minimized strain structure. The GaN buffer (i.e. depth 20 nm and over) is considered completely unstrained.

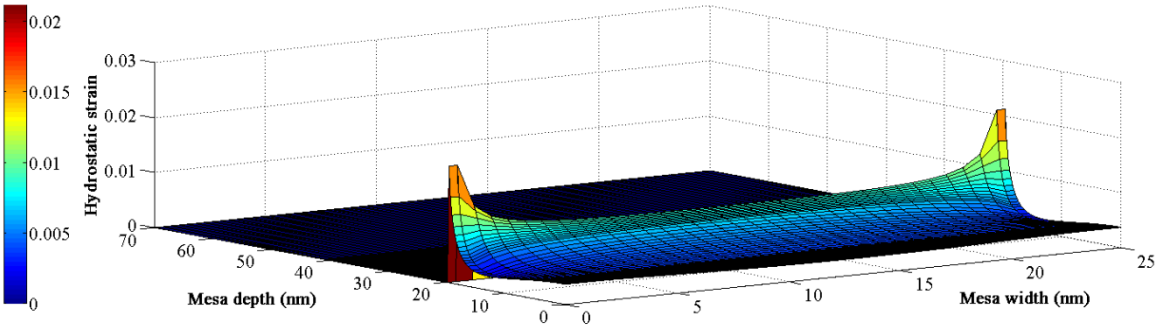

Figure 4.12 - Hydrostatic strain (sum of the diagonal strain tensor components) for the minimized strain structure. The GaN buffer (i.e. depth 20 nm and over) is considered unstrained.

4.5 Sheet charge concentration evaluation

In this section, the data analysis scheme used to extract the sheet charge concentration and the carrier-confinement for two-dimensional structures are presented in further details. Following this, simulation results are shown and trends evolving with varying the aluminum mole fraction of the AlGaN barrier, barrier thickness, Schottky barrier height, mesa width, and boundary conditions at the sidewalls are compared with the reported literature.

4.5.1 Calculating the average sheet charge density

In order to extract the sheet charge density from an electron distribution profile such as the one displayed in Figure 4.10, the average 2DEG sheet charge density $n_{sh\text{-}av}$ of the structure is calculated using:

$$n_{sh-av} = \frac{1}{w}\int_0^w n_{sh}(x)\,dx \tag{4.1}$$

where w is the width of the mesa and $n_{sh}(x)$ is the sheet electron concentration at some value of x. Equation (4.1) is valid for two-dimensional simulations, or in obtaining the average sheet charge density in a slice from a three-dimensional simulation. For three-dimensional simulations, the equation for obtaining the average sheet charge density across a mesa of cross-sectional area $w_x \times w_y$ is similarly calculated as:

$$n_{sh-av} = \frac{1}{w_x w_y}\iint_{(0,0)}^{(w_x,w_y)} n_{sh}(x,y)\,dxdy. \tag{4.2}$$

4.5.2 Influence of the aluminum mole fraction of the AlGaN barrier, mesa width, and barrier thickness

Figure 4.13 shows the calculated sheet charge density against the aluminum mole fraction of the AlGaN barrier, evaluated by the 2-D simulations of heterostructures of three different values of width (50, 100 and 150 nm). A Ni Schottky barrier height that scales with the aluminum composition, x, as $1.3x + 0.84$ was assumed on the top AlGaN surface. Also on this figure, results of a 1-D simulation of these structures, quite identical to the observation made by Jogai in [35], are provided for comparison. Following the assumptions of Jogai, in these 1-D simulations instead of a Ni Schottky gate contact, pinning to a fix surface donor state of 1.4 eV is assumed.

The difference between 2-D simulations and those 1-D simulations resembling the results of Jogai[26] are explained by highlighting two variations in the evaluation setup. First, that a minimized energy scheme was used to compute the strain in the structure of the 2-D simulations, inducing inhomogeneity in the strain field, whereas Jogai considers a discrete strain level and approximates its effect through a piezoelectric charge distribution that is added to his model. Second is the fact that when a two-dimensional structure is simulated (compared to a one-dimensional structure[27]) it spatially constrains the charge carriers and reduces their numbers near the sidewalls [27] because of the depleting nature of the sidewalls [26]. In Figure 4.13, the almost linear trend in the variation of the sheet charge density with the aluminum mole fraction is observed. Wider structures are also observed to have a higher average sheet charge density, where the difference between the 50 nm and the 100 nm wide mesas is higher than the observed variation between the 100 nm and the 150

[26] Simulations in this work and in Jogai both utilize a fix donor state, albeit of different value. AlGaN barrier thickness and aluminum mole fraction in the AlGaN barrier are similar.
[27] This amounts to a structure that is infinite in every horizontal direction.

nm wide structures. As expected, there is also a threshold value of x below which no 2DEG is formed.

Figure 4.14 depicts the sheet charge density as a function of the AlGaN barrier thickness for three different values of mesa width. As expected, the 2DEG enters a saturation phase as the barrier thickness increases. This effect is expected per Ibbetson *et al.* [34] and would be a partial indication that strain relaxation has occurred. Not unlike what is shown in Figure 4.14, Alsharef *et al*. also observed a smaller 2DEG density in devices of smaller mesa width [27]. They attributed this to the triple-gate effect around the structure. In that case, they forecasted a positive threshold voltage for mesa width under than 30 nm. The effect of body size reduction on the electron distribution is investigated in more details in the next section.

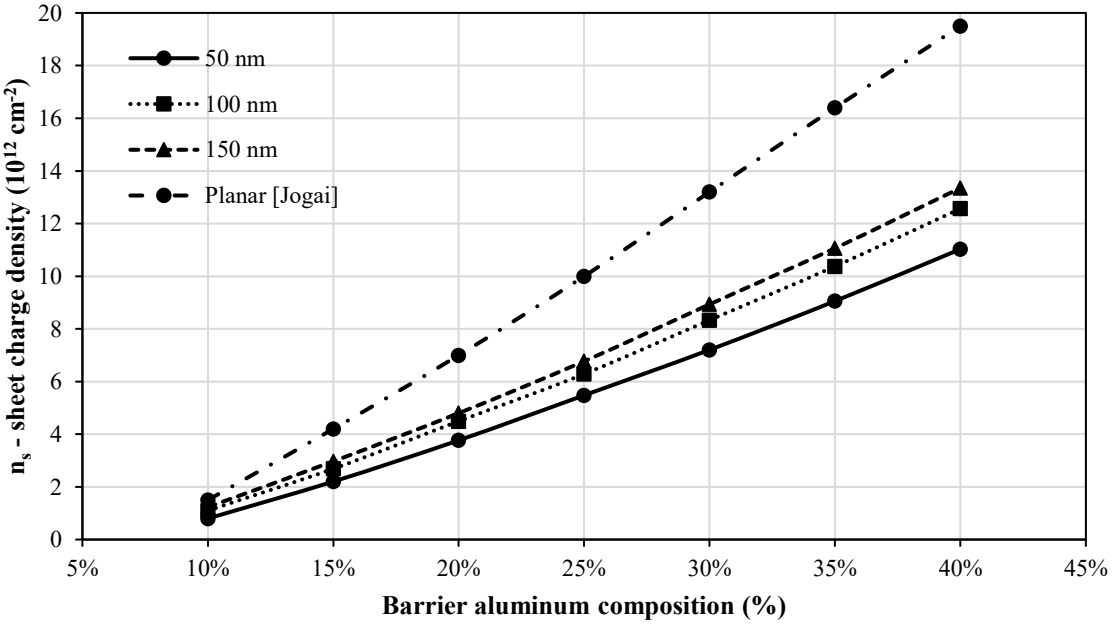

Figure 4.13 - Influence of the aluminum mole fraction of the barrier on the average sheet charge density in 2-D evaluated mesas of different widths and with a 20 nm thick AlGaN barrier. Comparison with data from *[35]* for a one-dimensional simulation is also made. Jogai assumes $q\phi_b = 1.4$ eV for a fix surface donor state, whereas we assume that $q\phi_b$ follows $(0.84 + 1.3x)$. The mesas were subject to the strain-minimization algorithm and simulated under closed simulation region assumptions.

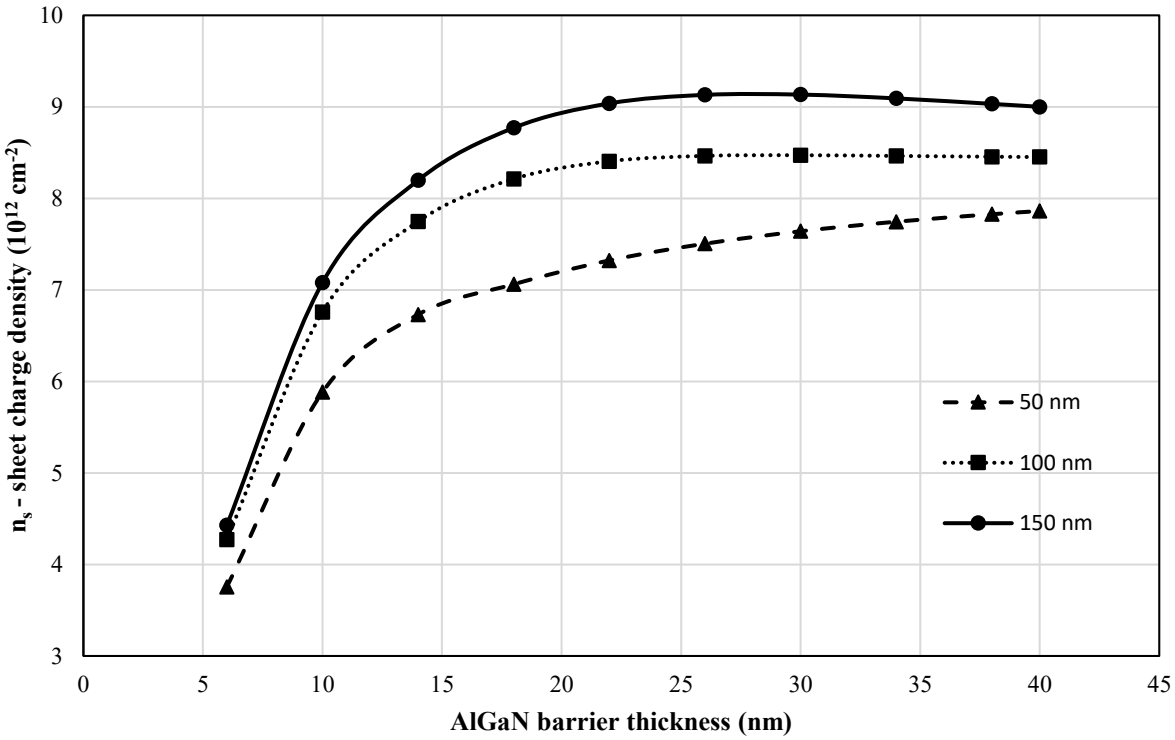

Figure 4.14 - Influence of AlGaN barrier thickness on the average sheet charge density for epilayers of different widths (for two-dimensional version of simulation). Aluminum mole fraction is constant at 30%, we thus assume $q\phi_b = 1.23$ eV. The structures were simulated under closed simulation region assumptions and the strain minimization algorithms.

4.5.3 Interpretation of the influence of the mesa's dimensions on the electron distribution profile

This section heavily rotates around a comparison with the prior work of Alsharef *et al.* [27]. Before comparing the results, the major differences among the sets of assumptions in that prior work and the present thesis are detailed. These are summarized in Table 4.1. The differences among these entries explain the observed differences among the numerical results. While trends remain identical, it should be noted that Alsharef *et al.* considered only the two extreme cases of strain in the barrier, namely: fully strained barrier and fully relaxed barrier. In their simulations, the strain coefficients were calculated theoretically and then entered as inputs into *nextnano* using zero-strain-amorphous as the algorithm. This algorithm considers either no applied strain or allows the

user to define the strain for every grid points. The bound polarization charge density, σ, was also imported directly. Since in the present thesis the author seeks to understand not just the effect of sidewalls but also the effect of strain relaxation, this work proposes an approach in which considering the energy minimization strain algorithm is paramount.

Table 4.1 – Assumptions adopted in this work and in *[27]*.

Parameters	**This work**	**Alsharef *et al.* [27]**
ϵ_r **($Al_{0.3}Ga_{0.7}N$)**	9.1	10.3
ϵ_r **(GaN)**	9.28	10.28
$q\phi_b$	1.3 x + 0.84	1 eV
Strain algorithm	Strained barrier using elastic energy minimization; unstrained buffer.	Two extreme cases considered (zero and full relaxation) under amorphous strain algorithm calculations.
GaN cap	0 to 10 nm	2 nm
Barrier thickness	Variable	14 nm
Aluminum mole fraction	Variable	30%
Dimensionality	1-D, 2-D and 3-D (to be reported in the next chapter)	2-D only
Body width	Variable	Variable
Doping	Undoped	Undoped

To look at the impact of mesa width under a better light, one should refer to Figure 4.15. The graphs show the profile of the electron concentration across the epilayer width when strain minimization is allowed. There are various points to notice in this depiction. First, as the mesa widens, the maximum electron concentration increases. Second, the electron concentration drops near the sidewalls. Third, the distributions shown in Figure 4.15 are, unlike the forecasts of Alsharef *et al.* in [27], not flat in the central part of the mesa width. While Fermi-level pining was absent among these assessments, the triple-gate effect is expected not to have participated in the depletion of the carriers close to the sidewalls. Hence, the third indicated observation on the data presented in Figure 4.15 allows attributing the observed reduction in carrier concentration to a

strain relaxation effect. Here, the relaxation of mechanical stress at the sidewalls directly influences the carrier density near the sides. As the epilayer width reduces, a larger portion of the epilayer will be affected by this stress relaxation, thus inducing a greater reduction in charge carrier density not only at the edge but throughout the mesa width. This effect was also investigated in nano-ribbons of varying widths [24]. In chapter 5, the same effect with respect to three-dimensional evaluation of epilayers is considered, where the hypothesis is confirmed on the effect of strain relaxation at the edges and its impact on the charge carrier density.

In Figure 4.16, the 2DEG region is represented under different angles for a 100 nm wide epilayer ($Al_{0.30}Ga_{0.70}N$/GaN) with an 18 nm thick barrier. It can be observed that most of the carriers are within 2 to 3 nm from the interface. The bottom left panel shows horizontal distribution of the carriersy at the peak concentration.

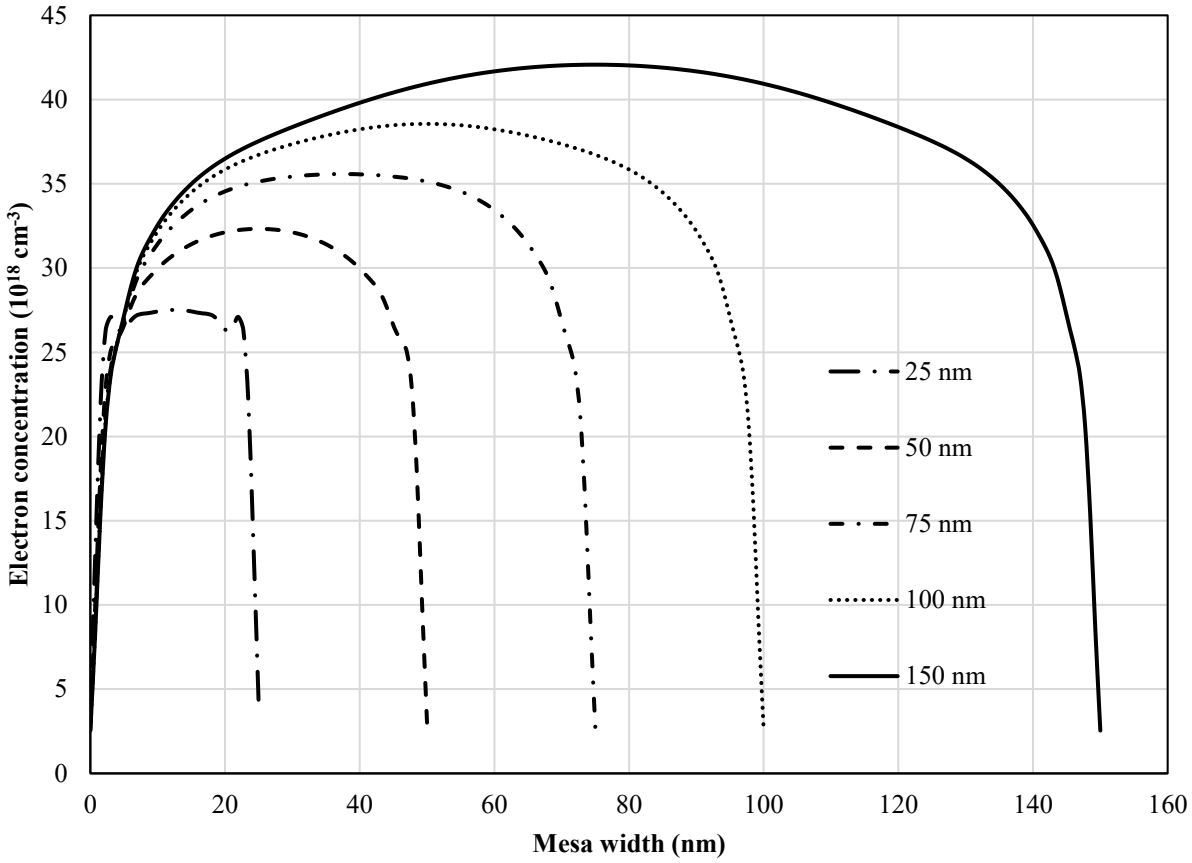

Figure 4.15 - Electron distribution in the 2DEG of the structure from Figure 4.1, showing the influence of body width. The electron distribution versus width is shown at the depth from the AlGaN surface where the maximum electron concentration occurs. The $Al_{0.30}Ga_{0.70}N$/GaN heterostructures (with AlGaN barrier of 20 nm) were simulated under closed simulation region assumptions and with energy minimization.

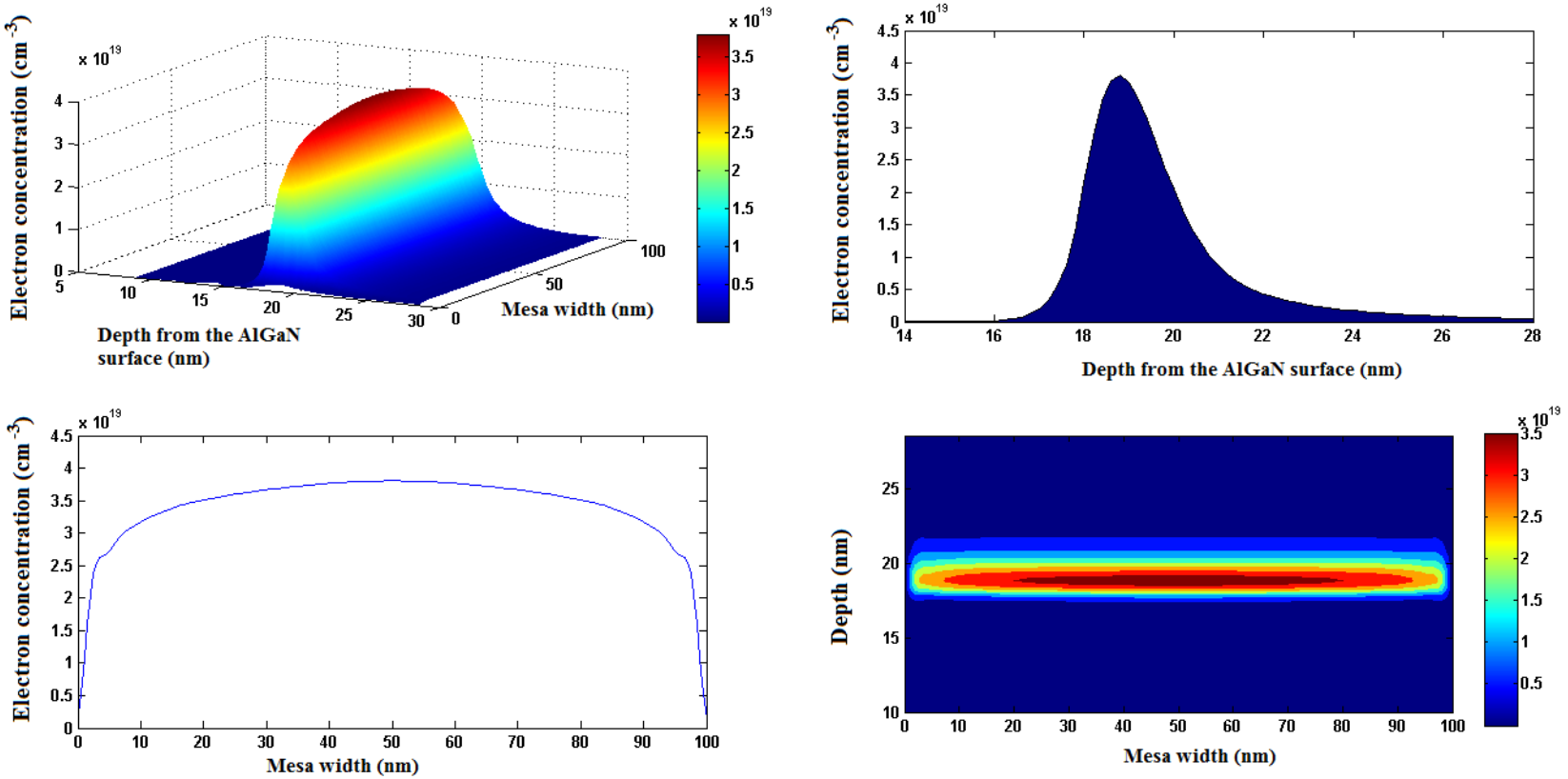

Figure 4.16 – Electron distribution in the body of a 100 nm wide $Al_{0.3}Ga_{0.7}N$/GaN structure with an 18 nm thick barrier obtained using the strain minimization algorithm and under the closed simulation region assumptions. Upper left: 2-D view of the carrier distribution. Upper right: 1-D side view showing the extent of the carrier confinement. Lower left: 1-D front view at the peak plane. Lower right: 2-D top view.

4.5.4 Carrier confinement

Based on the 2-D simulation results obtained from *nextnano*, this section considers the question of carrier confinement in the quantum well. The carrier confinement is influenced mainly by the polarization induced charges and the depth of the quantum well. Figure 4.17 and Figure 4.18 show the vertical distribution extent of the 2DEG for different epilayers. In both figures three points are highlighted, Z_P, the peak position of the concentration profile, Z_L, and Z_H that define the range of the region which contains 68% of the total electron concentration (tentatively taken as a demarcation value, where the electron concentration at Z_L and Z_H are equal). Accordingly, the larger the distance between Z_L and Z_H, the smaller is the depth of the quantum well (and likewise the smaller is the polarization), corresponding to a weaker carrier confinement.

While Figure 4.17 shows the carrier confinement range versus the aluminum mole fraction, Figure 4.18 shows the carrier confinement range as a function of the AlGaN barrier thickness. Based on Figure 4.17, for aluminum mole fraction ranging from 0.1 to 0.4, the carriers are observed to be confined within a depth of more than 6 nm for 0.1 aluminum mole fraction to about 2 nm for 0.4 aluminum mole fraction. In addition, it is observed that the centroid of the distribution gets closer to the heterointerface as the aluminum mole fraction increases (varying from 1.6 nm to 0.8 nm away from the heterointerface).

Comparing both graphs, one notices how the aluminum mole fraction impacts the carrier confinement range. Going from 0.4 to 0.1 aluminum mole fraction in AlGaN/GaN epilayer results in a multiplication by three of the 2DEG thickness, whereas the variation of the barrier thickness above 14 nm induces, at most a 0.5 nm change in the carrier confinement.

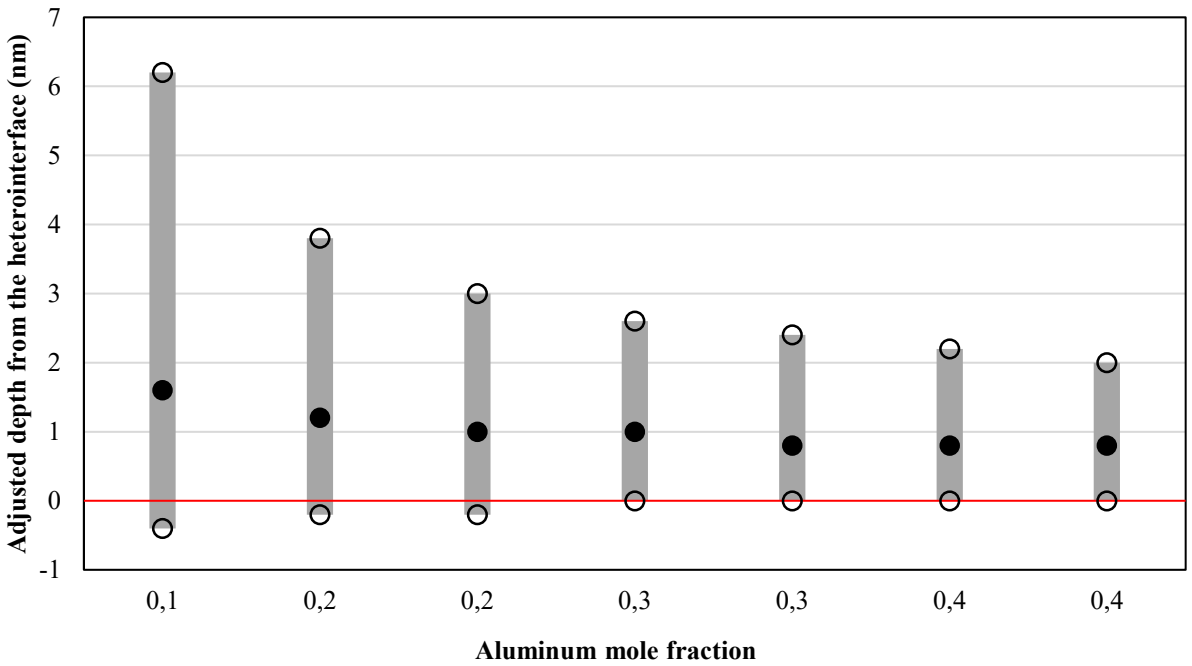

Figure 4.17 - Carrier confinement of the 2DEG for a 50 nm wide mesa whose AlGaN barrier is 20 nm thick (indicated by the horizontal red line). The full circles represent the peak of the distribution profile, while the open circles highlight positions Z_L and Z_H as identified in the text. The structures were simulated under closed simulation region and with energy minimization algorithm.

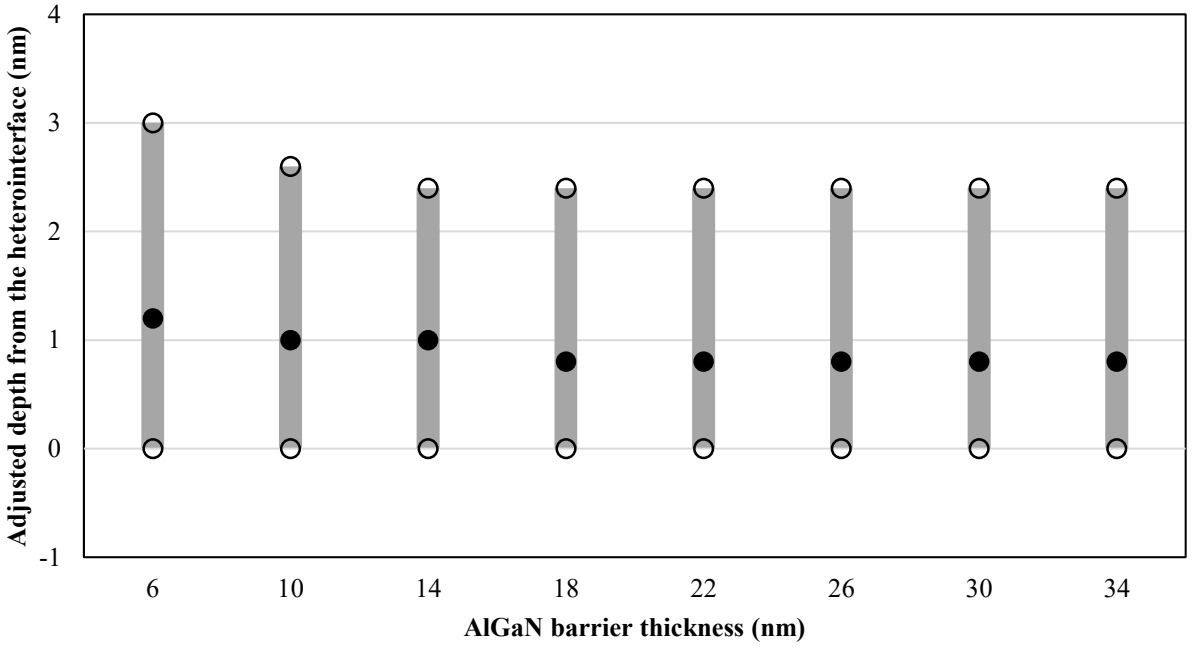

Figure 4.18 - Carrier confinement of the 2DEG for a 50 nm wide mesa whose aluminum mole fraction is fixed at 30%. The barrier thickness varies but the scale is with respect to the heterointerface. The circles have the same representation as in Figure 4.17. The structures were simulated under closed simulation region and with energy minimization algorithm.

4.6 Coexistence of 2DEG and 2DHG

As a matter of interest to GaN-capped HFETs, using *nextnano* 2-D simulations, this section looks into the factors leading to the coexistence of a two-dimensional hole gas (2DHG) and a 2DEG in a GaN/AlGaN/GaN heterostructure. Through a modification of the *nextnano* input files, it is possible to add a GaN cap to the epilayer shown in Figure 4.1.

Figure 4.19 shows the simulated band diagram, the electron, and the hole distributions in a one-dimensionally evaluated GaN/AlGaN/GaN epilayer with a 15 nm thick GaN cap and a 20 nm thick $Al_{0.30}Ga_{0.70}N$ barrier. Here a 1 eV Schottky barrier height and an applied surface potential bias of – 2 eV is considered. This figure depicts a 2DEG formation at the barrier/buffer heterointerface as well as a 2DHG at the cap/barrier heterojunction.

Figure 4.20 shows the relationship between 2DEG and 2DHG sheet charge densities (n_S and p_S) and the surface potential for two different cap layer thicknesses (5 nm and 15 nm). It can be noted that, for an identical surface potential, increasing the cap layer thickness lowers the 2DEG while increases the 2DHG density. However, when the 2DHG starts to form, the 2DEG sheet charge density approaches a saturation level (which happens at 2 eV surface potential for the 15 nm thick GaN cap epilayer example), while p_S still rises. The 2DHG being closer to the gate shields the 2DEG, resulting in the observed saturation.

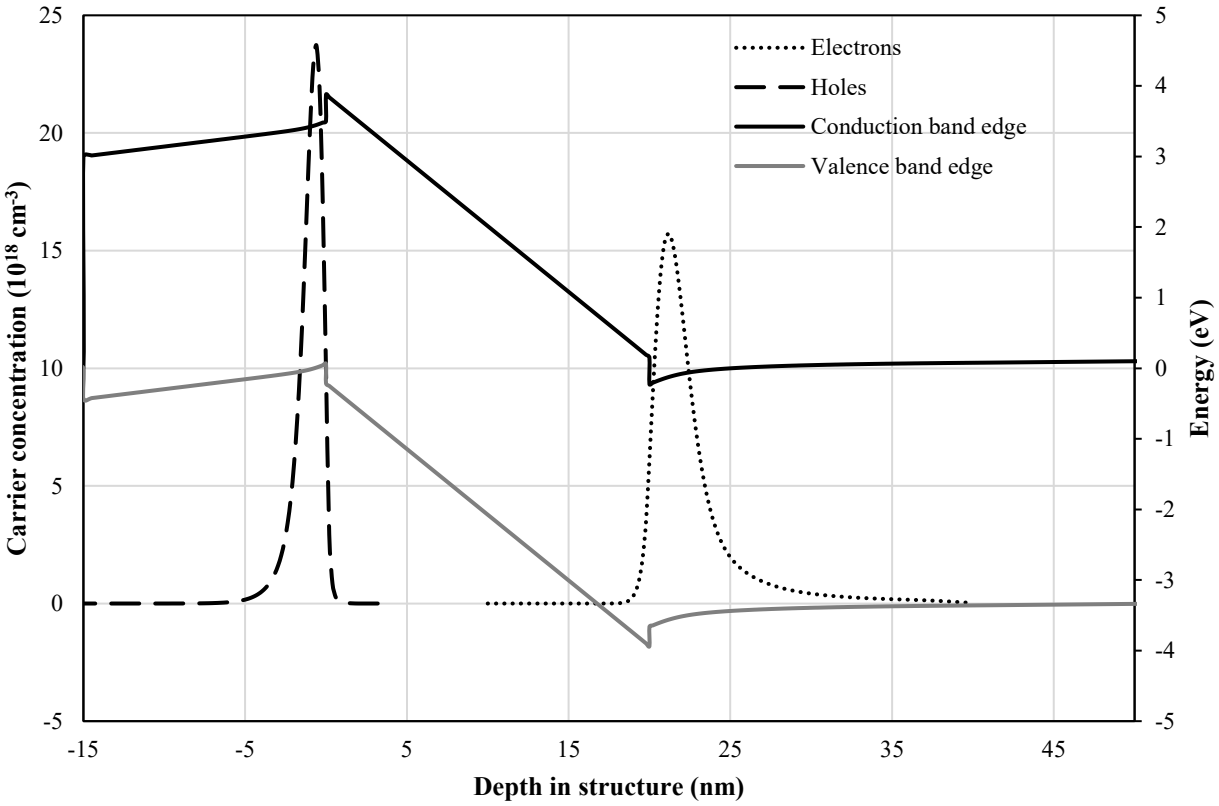

Figure 4.19 - Band diagram and free carrier concentration along the depth of a 1-D simulated GaN/AlGaN/GaN epilayer with a 15 nm GaN cap, 20 nm $Al_{0.3}Ga_{0.7}N$ barrier and 2 eV applied surface potential.

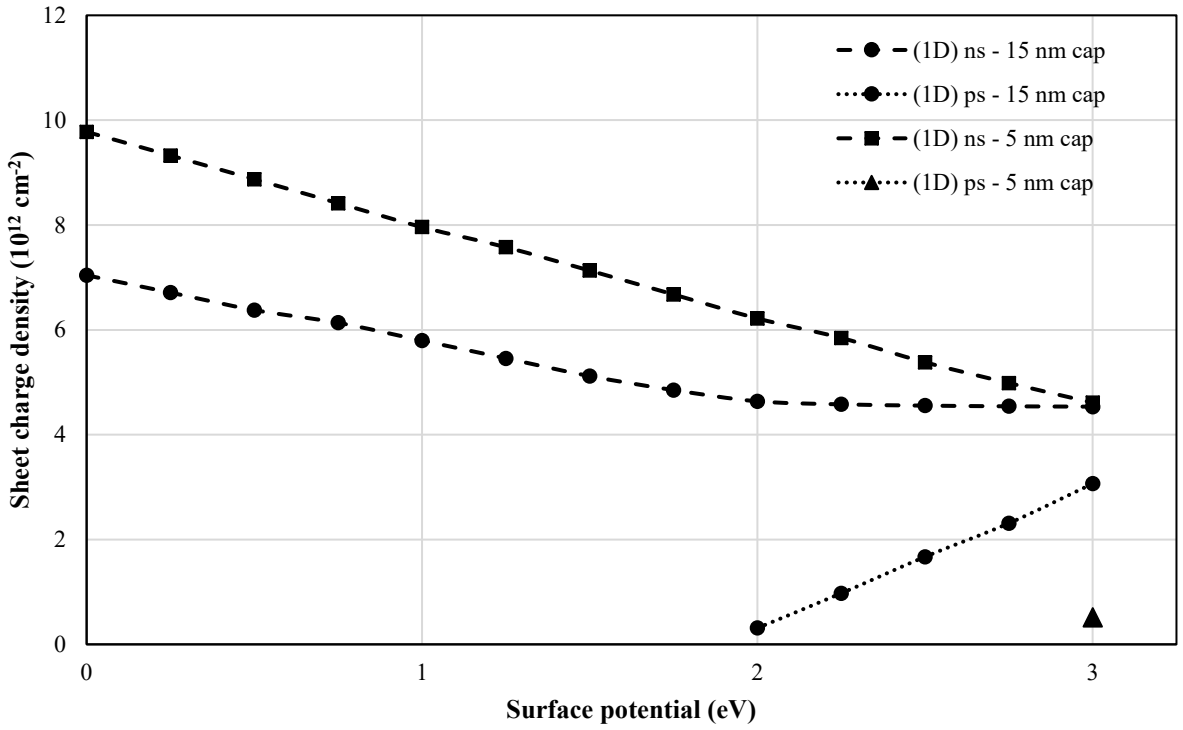

Figure 4.20 - Calculated 2DEG and 2DHG sheet charge densities (n_S and p_S) versus barrier height ($q\phi_b$) for one-dimensionally evaluated version of GaN/AlGaN/GaN epilayers under the homogeneous strain calculation algorithm with a 20 nm thick AlGaN barrier and 30% aluminum mole fraction. As shown for the 5 nm cap a 2DHG is only formed for higher values of surface potential.

In the data presented in Figure 4.21, the GaN cap thickness is kept to two values of 5 and 15 nm, while the sheet densities are calculated for varying AlGaN barrier thicknesses. In this figure, the case of a two-dimensionally evaluated GaN/AlGaN/GaN epilayer of 25 nm wide mesa is also presented. In this latter case, the GaN cap is 5 nm thick and is assumed to be unstrained. The barrier is, however, assumed to be homogeneously fully strained. As is the case for epilayers without GaN cap, thicker barriers are observed to lead to higher electron sheet densities. Following from observation of Figure 4.20, a thicker GaN cap results in a lower n_S while, for the same GaN cap thickness, the two-dimensional epilayer displays a lower electron sheet charge density. Only for the 15 nm thick GaN cap does a 2DHG appear for the thicker barriers.

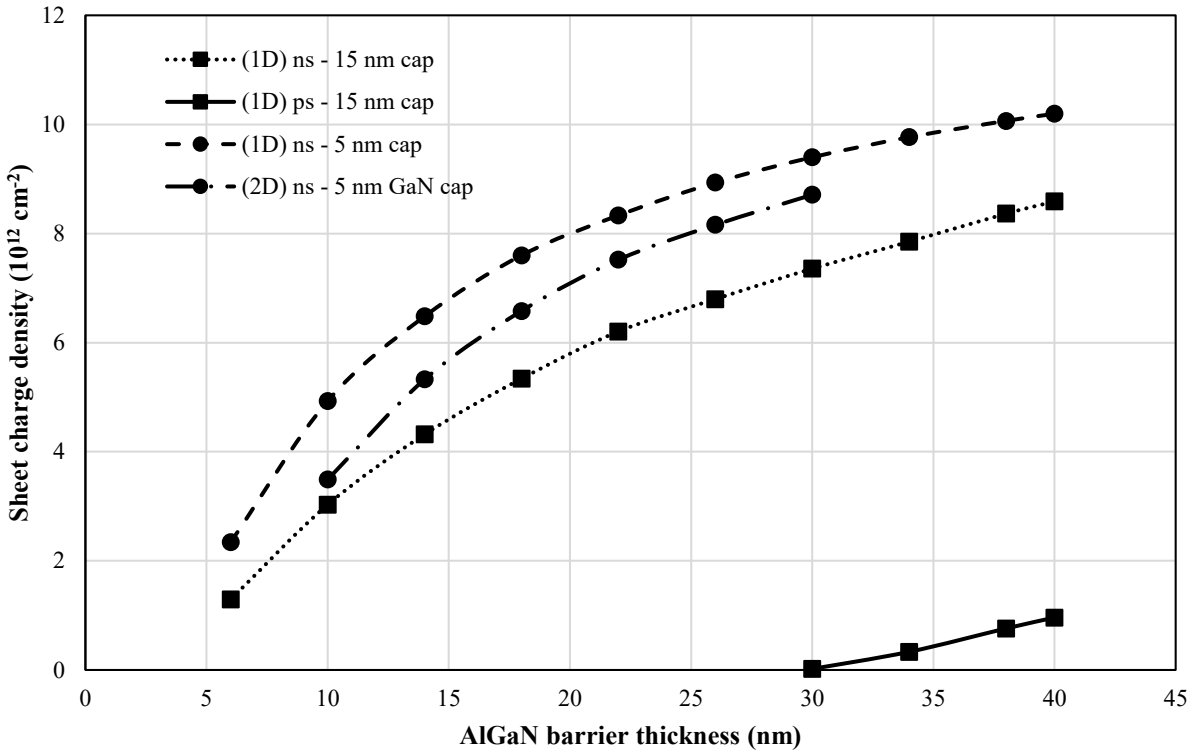

Figure 4.21 - Calculated 2DEG and 2DHG sheet charge densities (n_S and p_S) versus AlGaN barrier thickness for one- and two-dimensional versions of simulation of GaN/AlGaN/GaN epilayers (25 nm wide mesa) under homogeneous strain calculations with 5 or 15 nm thick GaN cap, 30% aluminum mole fraction and fixed 1 eV applied surface potential.

4.7 Conclusion

In this chapter, the *nextnano* environment was used to reproduce the results from the prior published works on electron population in AlGaN/GaN heterostructures. One- and two-dimensional versions of simulations were implemented and results were compared to accepted trends and values. While the trends similar to the prior work were observed, here it was also shown that strain relaxation can cause a reduction of the electron concentration even in the absence of such triple-gate effect. Also attention was paid to the relevance of 2DHG formation and saturation of 2DEG density when a GaN cap layer is used.

Chapter 5

Evaluation of electron concentration in terms of three-dimensional simulation of AlGaN/GaN heterostructures

In this chapter, the need for three-dimensional assessment of the electronic behavior of polar AlGaN/GaN heterostructures is substantiated. In section 5.1, the typical challenges in three-dimensional simulation of island-like mesa structures are described, where relevant results are presented for island-like and fin-like structures in section 5.2. In section 5.3, 2DEG profiles are presented for a variety of other isolation feature geometries, where conclusions are drawn concerning the effect of strain on the 2DEG density of three-dimensionally defined epilayers in correlation with feature geometry.

5.1 Typical challenges in simulating the island-like 3-D isolation features in *nextnano*

Looking back at Figure 4.13, it is striking to see a difference among the electron concentrations (and by extension the 2DEG sheet charge densities) of the one- and two-dimensionally simulated polar AlGaN/GaN heterostructures. In Figure 4.15, the lowering of the electron concentration near the sidewalls provided a hint that adding a dimension to the simulation introduces different

parameters that need to be considered when designing an AlGaN/GaN heterostructure, which in this specific case relates to strain evaluation at the side boundaries of the isolation feature.

As naturally expected, considering a larger number of volumetrically distributed nodes, in 3-D the numerical computations take more time to complete than the 1-D and 2-D versions of simulation. In light of this greater computation time, earlier in chapter 4 a trend describing the required number of eigenvalues was provided for three-dimensional simulation of polar AlGaN heterostructures with sufficient accuracy (see Figure 4.5). Even considering this limited number of eigenstates, in the present study each simulation performed in *nextnano* took between 2 to 8 hours to reach convergence. As mentioned earlier, to save on computation time, the gridding was more sparse in regions of lesser importance, such as deep in the buffer.

The simplest of $Al_xGa_{1-x}N$/GaN heterostructures considered in this chapter is shown in Figure 5.1. This structure mimics any of the three mesa geometries described in [10][28]. The full description of the structure and its parameters was given earlier in section 4.1. Considering the results presented in chapter 4, among the reported simulations of this chapter, only the energy minimization algorithm of *nextnano* was considered for strain computation. In section 5.2, the simulated heterostructures completely fill the simulation region as was described before.

[28] Long mesa, also known as fin, small mesa, also known as island, and a regular size mesa of lateral dimensions in the order of 100 μm.

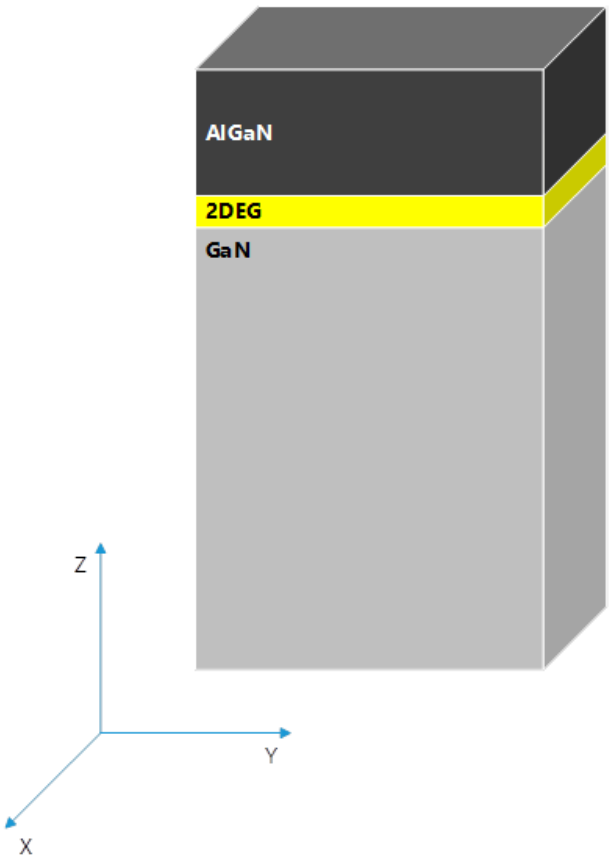

Figure 5.1 – A typical island-like AlGaN/GaN heterostructure. Grown along the [0001] axis, the heterostructure is undoped and a Schottky barrier is defined at the top surface.

5.2 3-D assessment of electron concentration among island-like isolation features

The need for three-dimensional simulation appears clearly to anyone looking at Figure 5.2. This figure compares the electron concentration profile two-dimensionally evaluated for a 50 nm wide AlGaN/GaN epilayer to the 3-D assessed electron concentration profiles for the case of cross-sections into the three-dimensional structure of two isolation features (one of fin-shape of 50 × 98 nm^2 dimension and the other of island-shape of 50 × 50 nm^2 dimension). The electron

concentration along the width of all epilayers is shown at a distance of about 1 nm from the heterointerface, which approximately presents the peak of the profile. The $Al_{0.30}Ga_{0.70}N$ barrier is 20 nm thick for all epilayers and Schottky barrier height is assumed equal to 1.23 eV. For the island- and the fin-shaped isolation feature, the cut is taken in the middle of the heterostructure (i.e. at x = 25 nm and x = 49 nm, respectively) to show the electron concentration only along the fin's short side. As expected from the observations made in chapter 4, the electron concentration is higher for the two-dimensionally simulated epilayer. In parts, the additional quantum confinement introduced by the extra simulation dimension, lowers the electron concentration for the island- and fin-shaped features. Explaining the differences among the electron concentration profiles observed on these two structures is the subject of the remaining parts of the chapter.

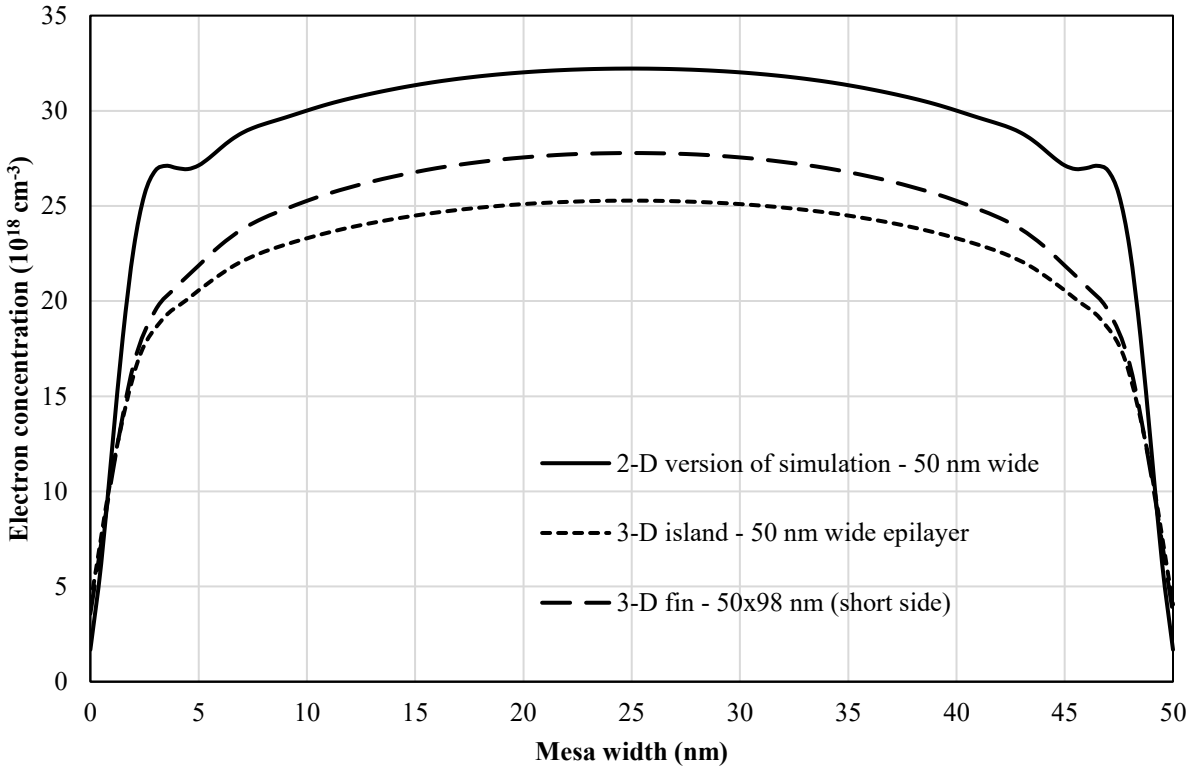

Figure 5.2 - Comparison between the electron concentration profiles along the width of the isolation feature at the peak of the profile for two- and three-dimensionally simulated AlGaN/GaN heterostructures. All three epilayers have a device width of 50 nm and are simulated under the closed simulation region assumptions. The heterostructures are composed of a 20 nm thick $Al_{0.30}Ga_{0.70}N$ barrier with a 1.23 eV Schottky barrier at the top exposed surface, strain minimization algorithm is in effect.

As was confirmed in chapter 4 in case of the one- and two-dimensional versions of the simulations, the 3-D evaluated island-like heterostructure follow an increasing/saturating trend of sheet charge density against the AlGaN barrier thickness. This is shown in Figure 5.3, where two island-like heterostructures were simulated: one with a cross-section of 30 × 30 nm^2 and the other with a 50 × 50 nm^2 surface area. The 50 × 50 nm^2 island-like heterostructure yields an average sheet density that is about two-thirds the value calculated according to the two-dimensional version of the simulations (for a similar width and barrier thickness). Among the two simulated island-like isolation features, for a given barrier thickness, the one of smaller surface area (900 nm^2 compared to 2500 nm^2) is shown to boast a lower sheet charge concentration.

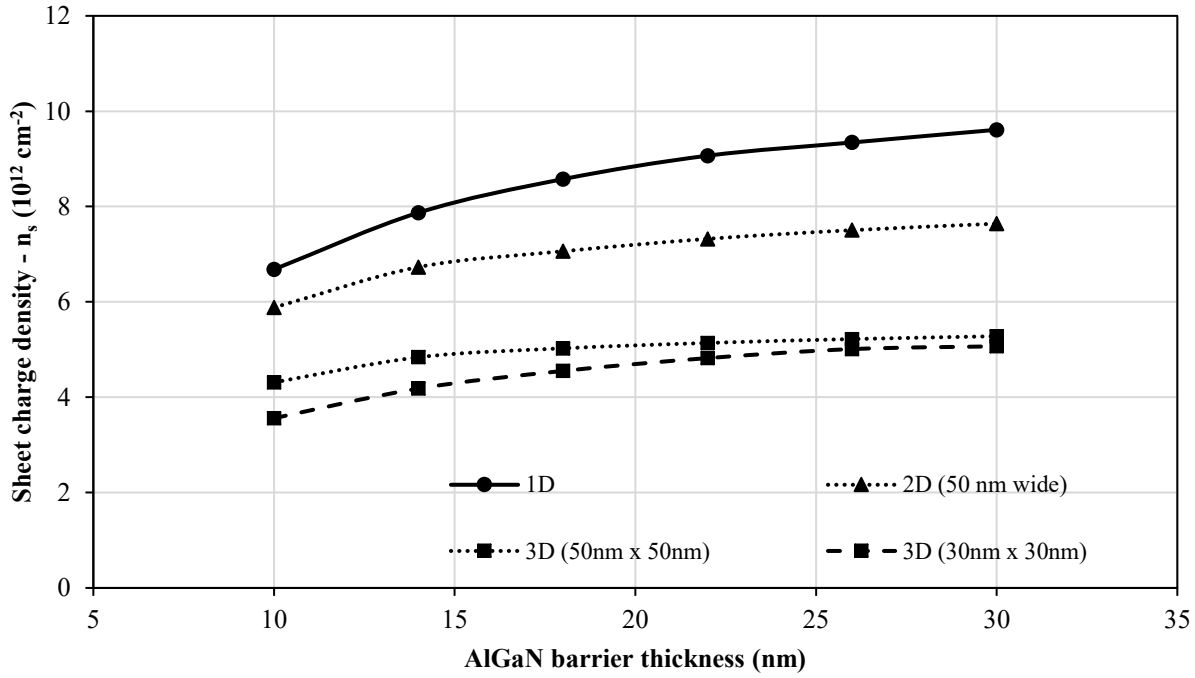

Figure 5.3 – Average sheet charge density versus AlGaN barrier thickness for epilayers simulated in the 1-D, 2-D and 3-D versions of the simulation. Fixed aluminum mole fraction of 30% is assumed as well as a closed simulation region. In the 2-D and 3-D cases, the strain minimization algorithm is in effect.

In Figure 5.4, the average sheet charge density is shown against the aluminum mole fraction for a 50 nm wide two-dimensionally simulated HFET and for two island-shaped HFETs of 30 × 30 nm^2 and 50 × 50 nm^2 top surface area, which were 3-dimensionally simulated. In all these simulations, an AlGaN/GaN heterostructure with a 20 nm thick AlGaN barrier is assumed. The variation in average electron concentration with the aluminum mole fraction is almost linear. Also, it is evident that a threshold value can be reached for each structure below which the 2DEG does not form.

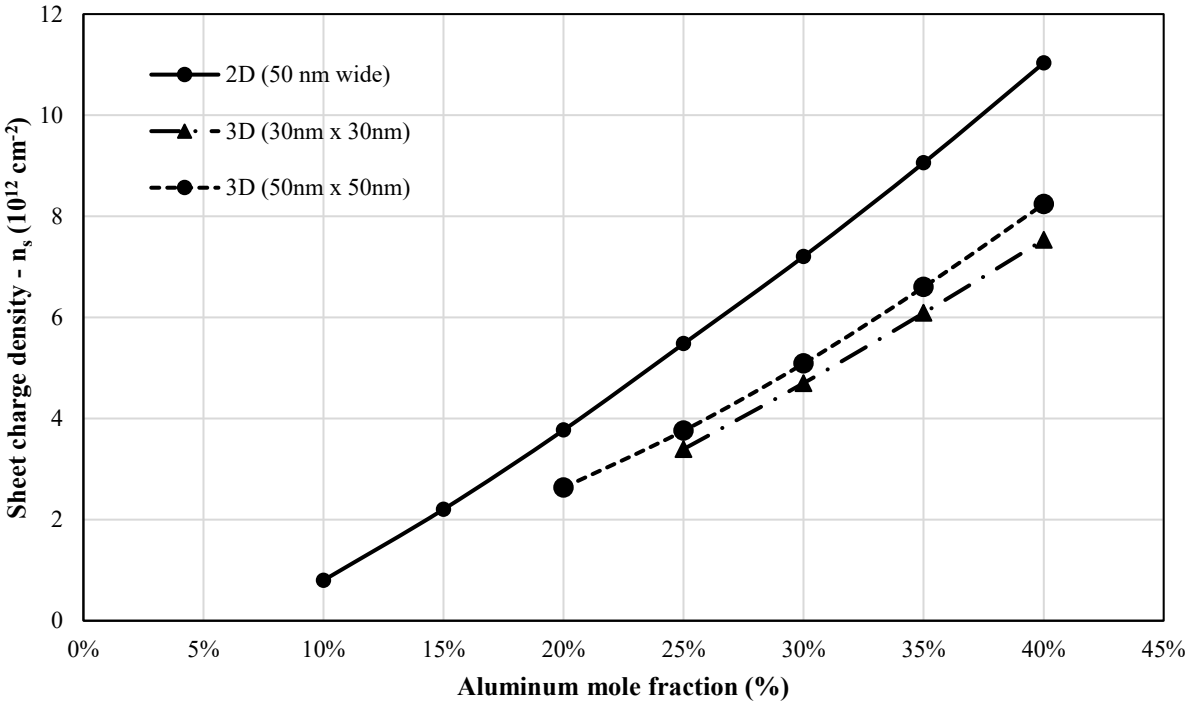

Figure 5.4 - Average sheet charge density versus aluminum mole fraction in the barrier for epilayers simulated in the 2-D and 3-D versions. Among these a fixed AlGaN barrier thickness of 20 nm is assumed as well as a closed simulation region. The Schottky barrier height is given by: $1.3 + 0.84x$ and strain minimization algorithm is in effect.

Figure 5.5 shows the electron concentration in the plane of highest concentration for an island-shaped heterostructure of 50 × 50 nm^2 top surface area. This figure illustrates the distribution of carriers in the plane as if a cut was being made parallel to the heterointerface at the peak of the 3-D profile. The carrier distribution at the peak plane can be seen as a reflection of the speculated

effect of increased strain reduction at the corners of the island-shaped isolation-feature and the depletion near the sidewalls.

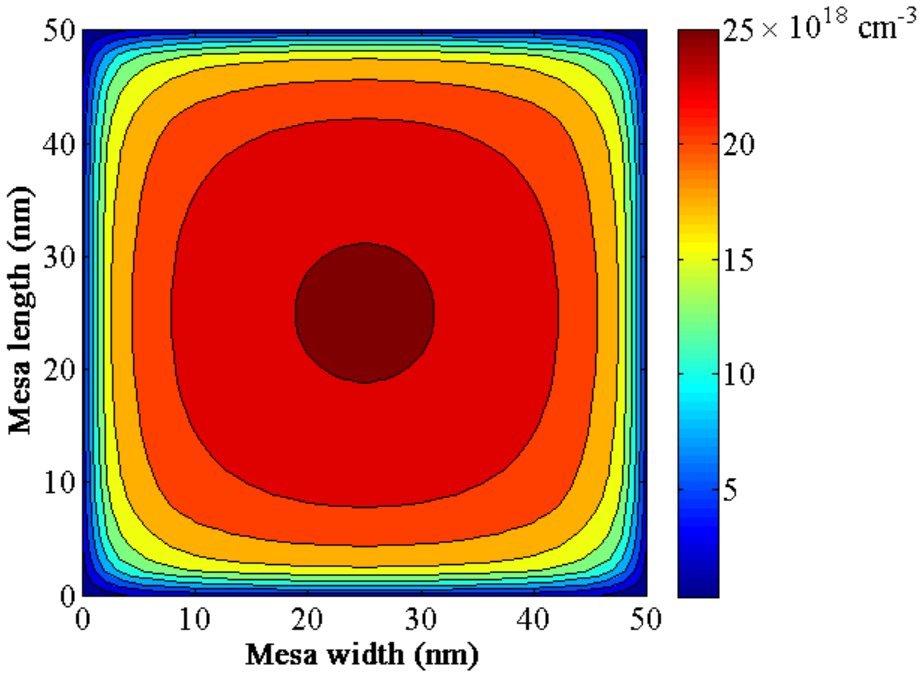

Figure 5.5 – In-plane electron concentration at the peak for the island-shaped polar Ga-face wurtzite AlGaN/GaN heterostructure of 20 nm thick AlGaN barrier of 30% aluminum mole fraction, 50 × 50 nm^2 top surface area where a 1.23 eV Schottky barrier height is considered and the simulation is performed under the closed simulation domain assumptions and strain minimization algorithm is in effect.

In order to compare the effect of geometry on the electron concentration of the so-called peak plane[29], Figure 5.6 is provided. In this figure, one can compare the electron distribution between an island- and a fin-shaped AlGaN/GaN heterostructure, where both have a 2500 nm^2 top surface area. In terms of a comparison between the 2-D profiles shown in Figure 5.6 (a) and Figure 5.6 (b), it is observed that the elongated geometry of the fin-like structure impacts the electron distribution due to narrowing along the width of the fin. For the fin-like heterostructure, vertical and horizontal cuts through the distribution for the peak plane are shown in Figure 5.6 (c). A

[29] This is the plane in which the highest electron concentration occurs.

feature observed in Figure 5.6 (c) is the presence of spikes at the two opposite ends of the short-side profile. It is speculated that this occurs because of a lack of symmetry between the subband solutions at the boundaries for narrow structures when quantum effects come into play. To substantiate this, a better visual depiction of subband probability density function is provided in Figure 5.7 and Figure 5.8 (considering an island-shaped and a fin-shaped heterostructure, respectively). In both figures, the wave function solutions at the centroid of the 2DEG distribution are provided. The figures show the probability density functions of the first four subbands in the plane of highest electron concentration. For Figure 5.7 and Figure 5.8, the top surface area is 2500 nm^2 and all the other composition parameters are equal. Among these, one should note the major difference between the third and fourth wave functions of each geometry. Despite the different scales on which the figures are presented, one clearly sees how the geometry affects the spatial distribution of carriers within the heterostructure. With increasing lateral confinement, the wave function peaks in different locations in the fin-like heterostructure compared to the more symmetric island-shaped heterostructure.

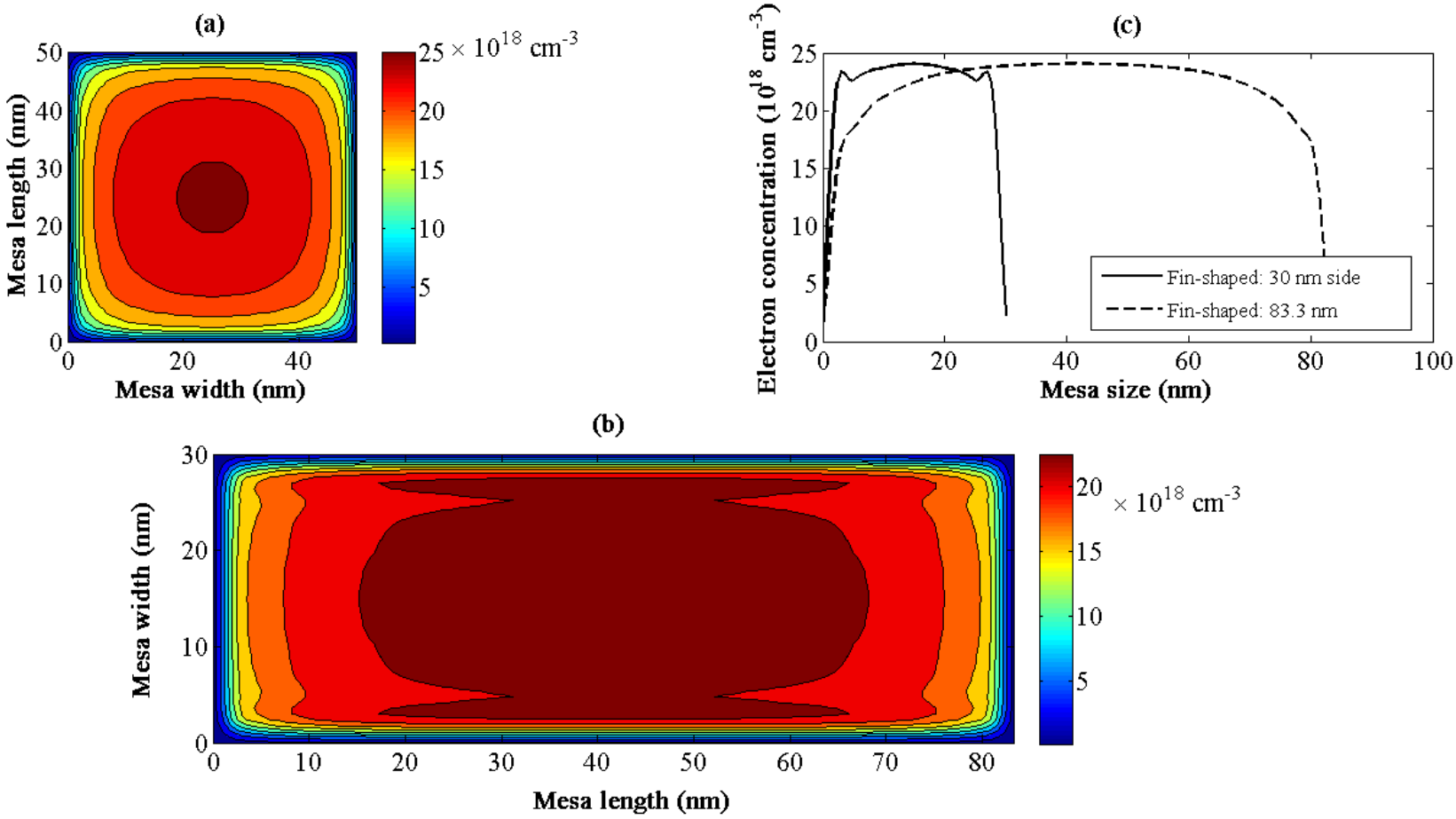

Figure 5.6 – In-plane electron concentration at the peak for the (a) island (50 × 50 nm) and (b) fin-like (30 × 83.3 nm) AlGaN/GaN heterostructures. Note that the x- and y-axes for the inset (b) are on different scales to highlight the spikes. Both heterostructures have a 20 nm thick AlGaN, 30% aluminum mole fraction, 2500 nm^2 top surface area and 1.23 eV Schottky barrier height and are simulated under the closed simulation regional assumptions. (c) Depicts cuts through the electron concentration profile in the fin-like structure along the short and long axis of the fin. The strain minimization algorithm is in effect.

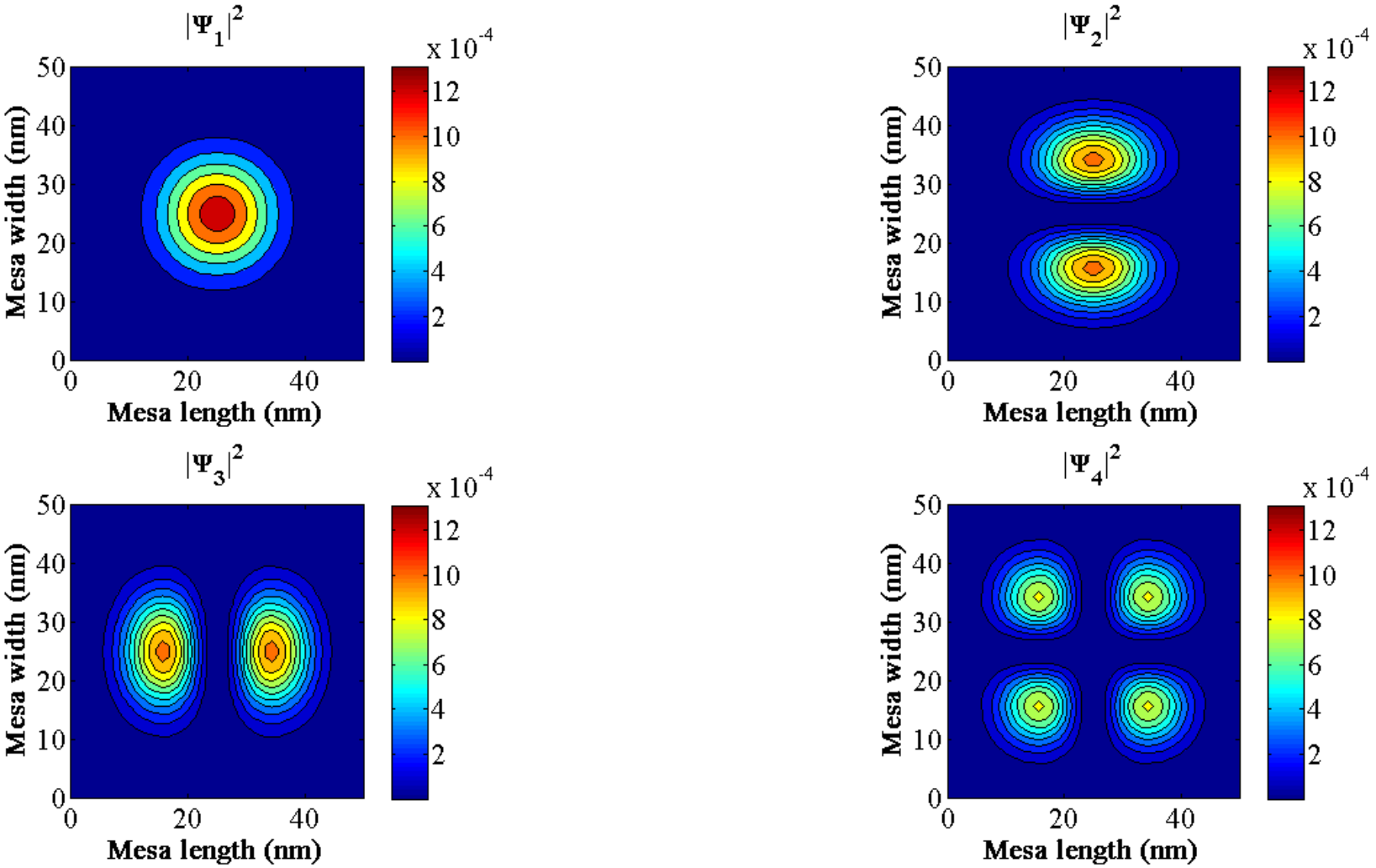

Figure 5.7 – First four wave-function squared solutions for an island-shaped (2500 nm^2 top surface area) $Al_{0.30}Ga_{0.70}N$/GaN heterostructure under energy minimization strain algorithm for simulation domains matching exactly the epilayer structure.

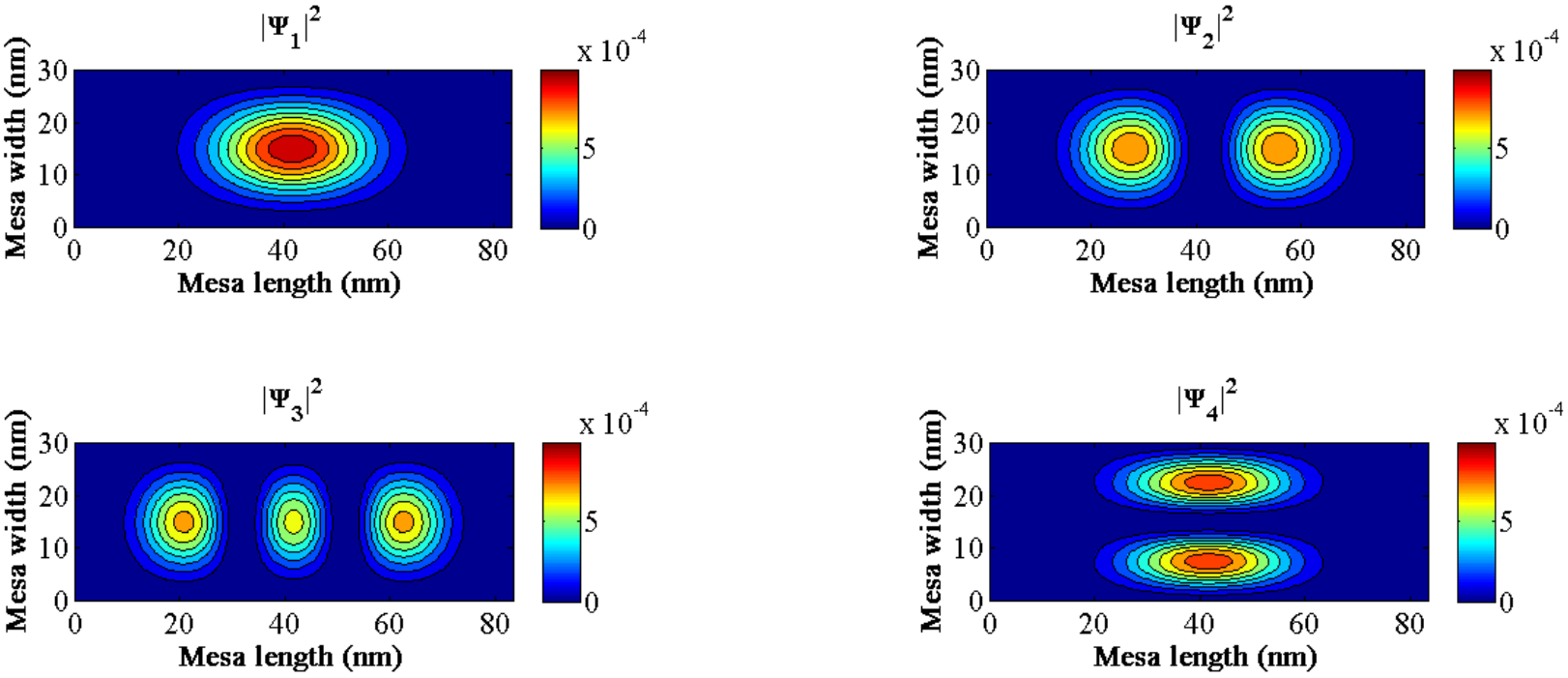

Figure 5.8 - First four wave-function squared solutions for an elongated fin-shaped (2500 nm^2 fin-like top surface area) $Al_{0.30}Ga_{0.70}N/GaN$ heterostructure under energy minimization strain algorithm for simulation domains matching exactly the epilayer structure.

In terms of the observed influence of the geometry of isolation feature on the average 2DEG concentration of a polar AlGaN/GaN HFET, an interesting metric proposed in [11] is to compare different geometries via their lateral perimeter-to-area ratio. In the context of the observed variations in transistor's threshold voltage, this metric was used to show how the positive shift in threshold voltage could not be only attributed to the improved proximity of the gate electrode to the middle of the channel (i.e. via creating a triple-gate effect), but that some explanation had to be linked to the evolution of peel forces around the structure (leading to a reduction of the piezoelectric polarization across the device).

Figure 5.9 shows the average sheet charge density in the epilayers versus the perimeter-to-area ratio for island- and fin-shaped mesas. For the fin-like mesa, one side was held constant at 30 nm, while letting the length of the other side to vary. Thus, as the top surface area grew, the fin was increasingly elongated. In islands, however, both dimensions among the simulated structures are equal. For both types of structures, the AlGaN barrier thickness is 20 nm and the aluminum mole fraction in the barrier is 30%. Based on what is shown in this figure, the trend observed in [11] holds well: the higher the perimeter-to-area ratio, the lower the sheet charge concentration. This trend approaches a similar value, for both geometries, as the device size shrinks indicating a limit in downscaling the size of the isolation-feature. However, what is more interesting is the stark difference between the island- and fin-shaped mesas at smaller values of perimeter-to-area ratio. For a similar perimeter-to-area ratio, the island-shaped structure boasts a smaller average sheet charge concentration than its fin-isolated counterpart. For the simulations presented in Figure 5.9, the simulation domain matched exactly the extent of the simulated heterostructure.

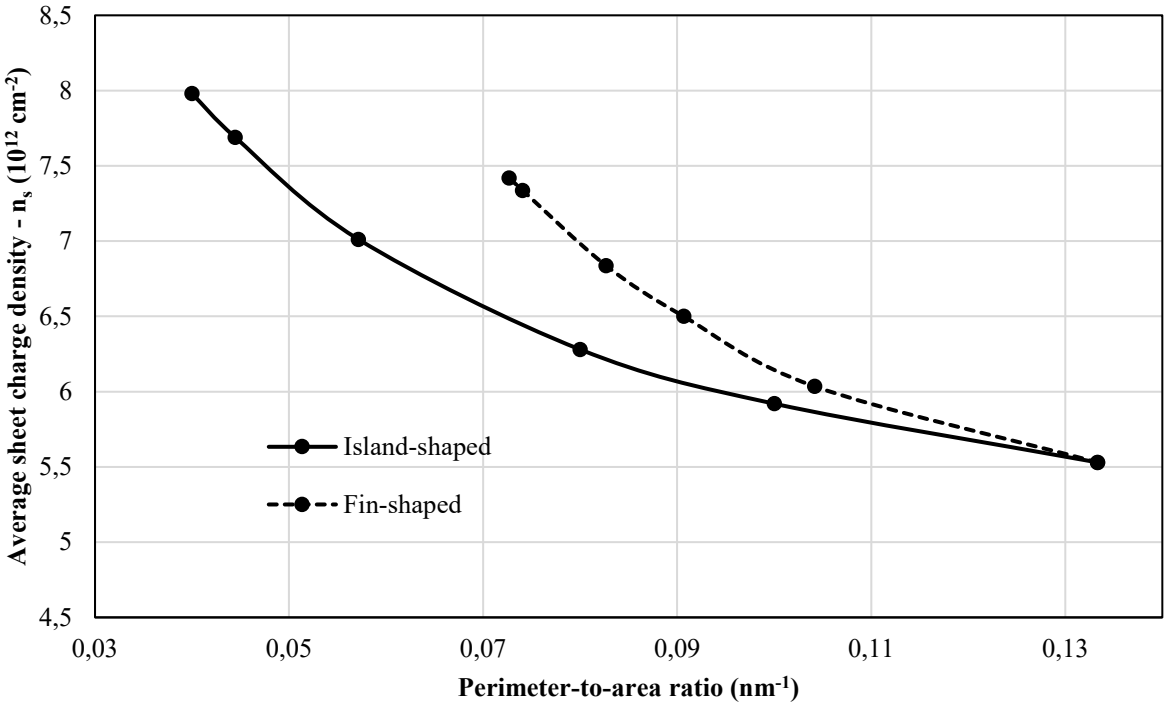

Figure 5.9 – Average sheet charge density versus perimeter-to-area ratio for two types of 3-D simulated epilayers matching exactly the simulation region ("closed simulation"). The aluminum mole fraction is 30% in both cases with a 20 nm thick AlGaN barrier and the strain minimization algorithm is in effect. The fin-shaped epilayer, one side was held constant at 30 nm. The length of the other side was left varying.

In Figure 5.10, to illustrate the impact of strain at the pseudomorphically-grown polar AlGaN/GaN heterojunctions on the electron concentration, the elastic energy density is shown for two island-like structures of different top surface areas (i.e. 1600 nm^2 among the top three panels and 4900 nm^2 among the bottom three panels). One must recall from section 3.2.1 that the elastic energy density is to be minimized in the calculation of strain minimization algorithm. This energy density is presented here in units of eV/nm^2. In the panels (a), (b), (d), and (e) of Figure 5.10, horizontal cuts in a plane slightly above the heterointerface (that is in the AlGaN barrier)[30] are shown. Panels (b) and (e) zoom in the top left corners of each structures to illustrate the impact of corners on the elastic energy density. In terms of the elastic energy density, vertical cuts through the epilayers are

[30] The horizontal cut readouts are taken in the AlGaN barrier at the first grid point from the heterointerface

shown in (c) and (f). Based on these graphs, several observations can be made. Whereas, looking at (a) and (d), the elastic energy density is observed to be almost isotropic with small inflexions at the edges. A more detailed look in (b) and (e) reveals that the elastic energy density is one order of magnitude greater in the corners compared with the center in both structures, while fading in faster for the case of the smaller island. In addition, the vertical cuts presented in panels (c) and (f) confirm a finding which was reported earlier by Joglekar *et al.* in [24], which is that the stress in the middle of a device is smaller for smaller nanowires.

Figure 5.11 places the electron concentration profile next to the hydrostatic strain[31] for the aforementioned two islands of 1600 nm^2 (top panels) and 4900 nm^2 (bottom panels) top surface area. Among these, the electron concentration is taken in the simulated planes of highest carrier concentration, which are 0.9333 nm and 0.8400 nm below the heterojunction, respectively. The hydrostatic strain components are taken in a plane 0.375 nm and 0.250 nm above the heterointerface, (i.e. in the AlGaN barrier). One should notice how the contour levels of the electron concentration closely match those from the hydrostatic strain. Accordingly, the rounder variations are observed for the smaller islands, and more square for the larger islands, highlighting the impact of piezoelectric polarization on the electron concentration.

[31] The hydrostatic strain is the trace of the strain tensor matrix, that is $\varepsilon_{XX} + \varepsilon_{YY} + \varepsilon_{ZZ}$.

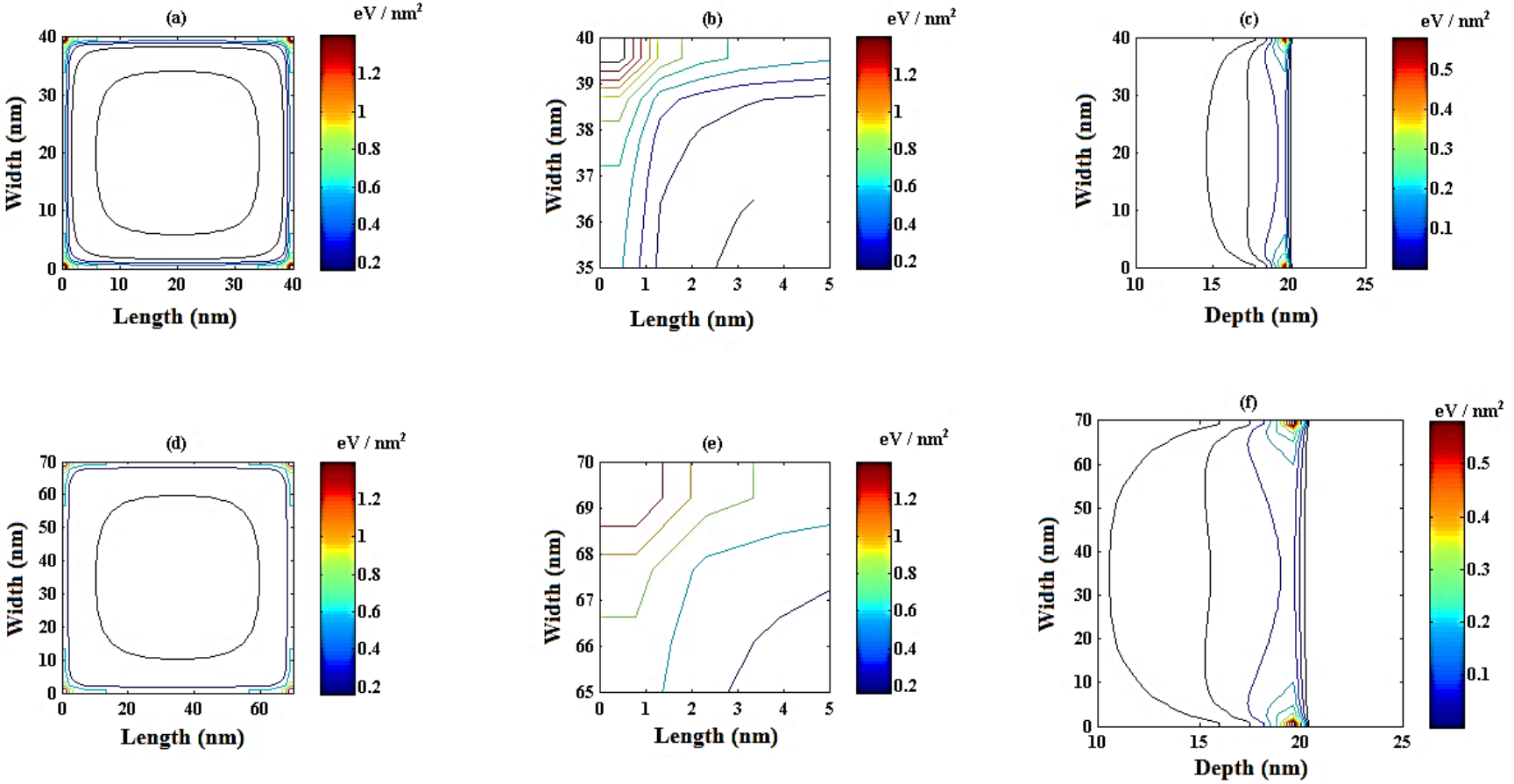

Figure 5.10 – Elastic energy density (in eV/nm^2) for a 1600 nm^2 (a, b, and c) and a 4900 nm^2 (d, e, and f) polar $Al_{0.30}Ga_{0.70}N$/GaN heterostructures of equal lateral dimensions for "closed simulation region". Figures (a) and (d) show a horizontal cut taken at 0.375 nm and 0.250 nm above the heterointerface, in the barrier for the heterostructures of cross-section 1600 nm^2 and 4900 nm^2, respectively. (b) and (e) zoom in the top left corner of each epilayer to show further details while (c) and (f) show a vertical cut through the depth of the device taken in the middle of it (at y = 20 nm and y = 35 nm, respectively). The strain minimization algorithm is in effect.

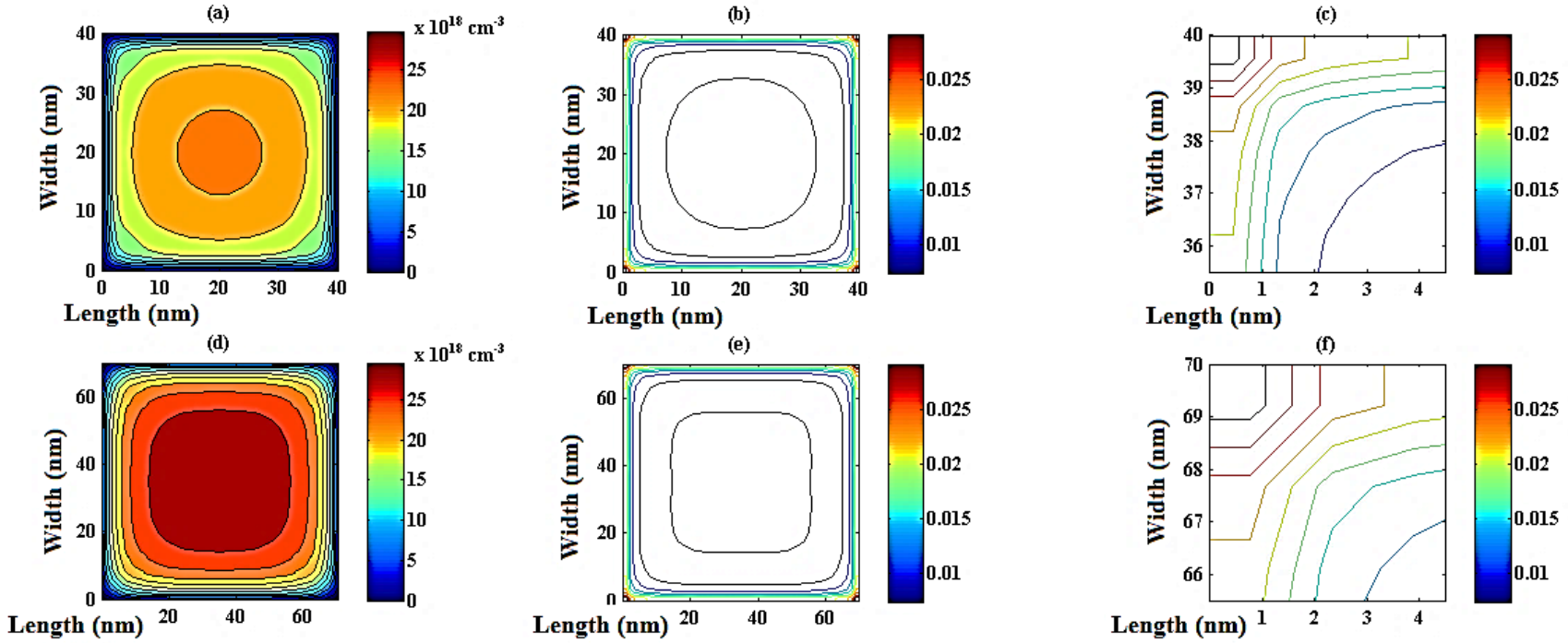

Figure 5.11 – Electron concentration profiles (in (a) and (d)) and hydrostatic strain coefficients (in (b), (c), (e) and (f)) for a 1600 nm^2 (panels a, b, and c) and a 4900 nm^2 (panels d, e, and f) island $Al_{0.30}Ga_{0.70}N/GaN$ heterostructures for "closed simulation region". The electron concentration is taken at the peak concentration for both epilayers, (i.e. at a depth of 0.9333 nm and 0.8400 nm below the heterointerface for the 1600 nm^2 and 4900 nm^2 versions, respectively). Figures (b), and (e) show a horizontal cut taken 0.375 nm and 0.250 nm above the heterointerface, in the barrier for the 1600 nm^2 and 4900 nm^2 versions, respectively. (c) and (f) zoom in the top left corner of each epilayer to show detailed level curves. The strain minimization algorithm is in effect.

5.3 Effect of isolation-feature geometry on carrier concentration

5.3.1 Simulating different geometries of different degrees of roundness

Authors of [10] have discussed the potential influences of peel forces on the 2DEG concentration of polar AlGaN/GaN heterostructures. To isolate this effect, one idea which was developed experimentally in [11] is to increase the perimeter-to-area ratio of the island's top surface while maintaining the surface area constant. To further develop this idea, simulations of polar Ga-face AlGaN/GaN heterostructures were performed for geometries ranging from a triangular prism to a cylinder. To simplify the terminology, the words nanowire or nanorod will be also used going forward. An example of such a nanowire is shown in Figure 5.12. This HFET structure is in every way identical to the island heterostructure described in Figure 5.1, except for its lateral geometry.

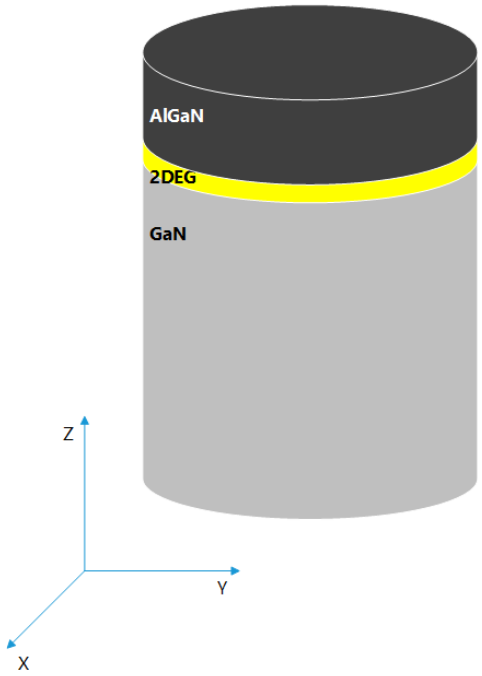

Figure 5.12 - Typical cylindrical AlGaN/GaN heterostructure. Grown along the [0001] axis, the heterostructure is undoped and a Schottky barrier is defined at the top surface. *nextnano* allows adjustments of the top surface area.

The five different top surface geometries considered in this work are shown in Figure 5.13. Among the considered geometries, going from the triangular prism to the cylinder[32] perimeter-to-area ratio of the nanowire is decreased gradually while the surface area is kept constant[33]. Experimentally, avoiding the etching process, nanowires with triangular cross-sections were synthesized in 2009 using n-type Si (100) substrates [59]. Since *nextnano* only allows for a rectilinear gridding, the actual rendering of the cylinder is pixelized, see Figure 5.14. Evidently, increasing the grid density allows one to tend towards a perfect cylinder, at the expense of greater computation time.

Another impact of the rectilinear gridding is a need for a redefinition of the simulation region. Up to this point in our discussion, the epilayers boundaries defined the extent of the simulation region. Figure 5.15 shows how non-cubic nanowires fit within a rectangular simulation domain. In our simulations, the void between the extent of the simulation region and the nanowire is assumed to be filled with air. Thus, as mentioned in chapter 3, for all simulations to come, there is a need to consider surface states emerging at the sidewalls. The discussion in section 2.4 proves helpful in determining the Fermi level pinning due to dangling bonds. In our simulations, originally, levels ranging between 0.5 to 0.7 eV were put forward depending on the surface orientation. Later on, to simplify the matter, an average value of 0.6 eV was taken into account for all side surfaces. Simulations performed under this assumption will be termed pinned. Other simulations were also performed where the value of the Fermi level at the sidewalls was left unfixed. These will be referred to as floating or open simulation domain.

[32] With the island and fin-like structures and hexagonal prism in between.
[33] For the triangular prism, island, and cylinder this proportion is along the order of 2.57 : 2.26 : 2.

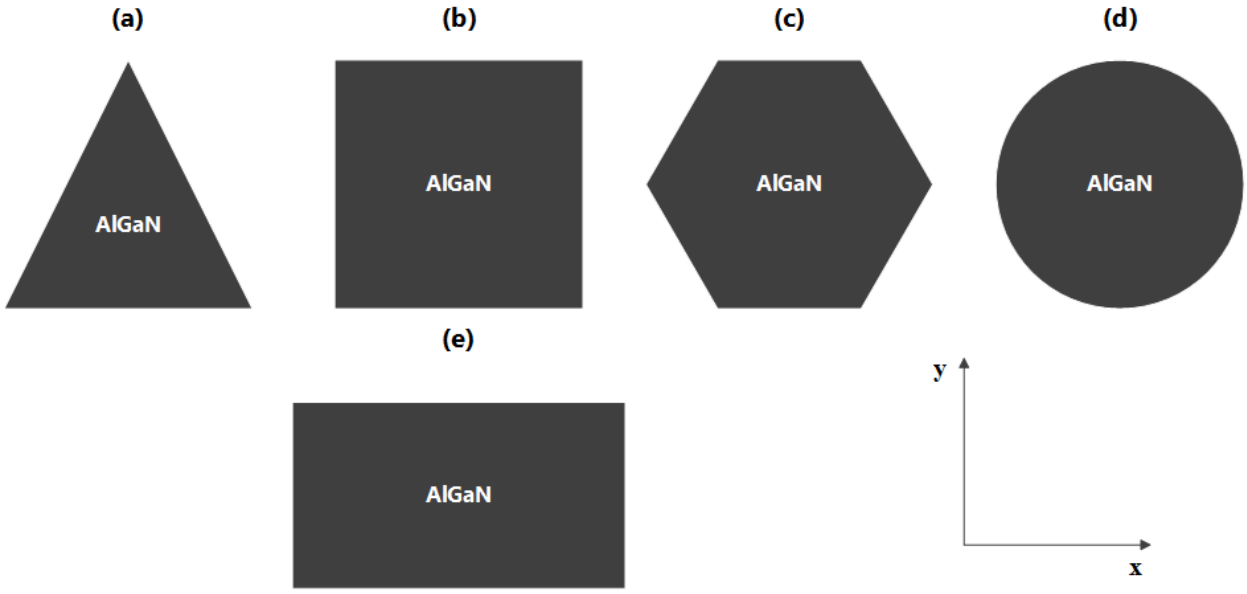

Figure 5.13 – Top view of the five different simulated nanowires. (a) triangular prism, (b) cube, (c) hexagonal prism, (d) cylinder, (e) fin-like structure.

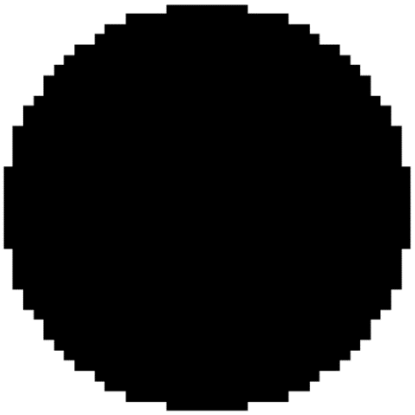

Figure 5.14 - Top view of a 1600 nm^2 (top surface area) cylindrical nanowire as simulated by *nextnano*.

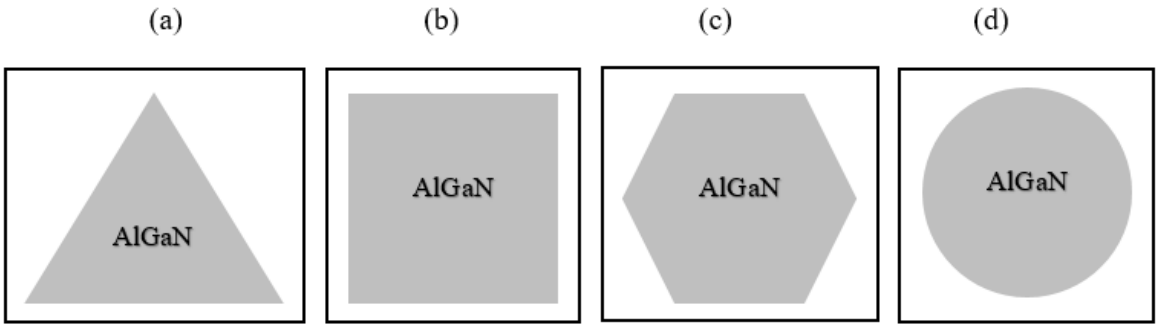

Figure 5.15 – Illustration of the top views of the rectilinear simulation region boundaries compared to the nanowire itself (darker region).

The Fermi level pinning at the sidewalls is characterized by an upwards band bending which is illustrated in Figure 5.16. The conduction and valence band edges are shown for a middle vertical cut through an island-shaped heterostructure whose $Al_{0.30}Ga_{0.70}N$ barrier is 20 nm thick. The cut is made 1 nm below the heterointerface in the GaN buffer, in the plane of highest electron concentration. This Fermi level pinning, as is the case in [27], explains partly the depletion of electrons near the sidewalls. To compare with geometries for which the simulation region boundaries matched exactly the structure, the band edges are calculated assuming both types of boundary conditions: the “closed-simulation-domain” and the “Fermi-level-pinned” at 0.6 eV at the sidewalls. The main difference among the two sets is the side-wall band bending that extends about 10 nm into the device.

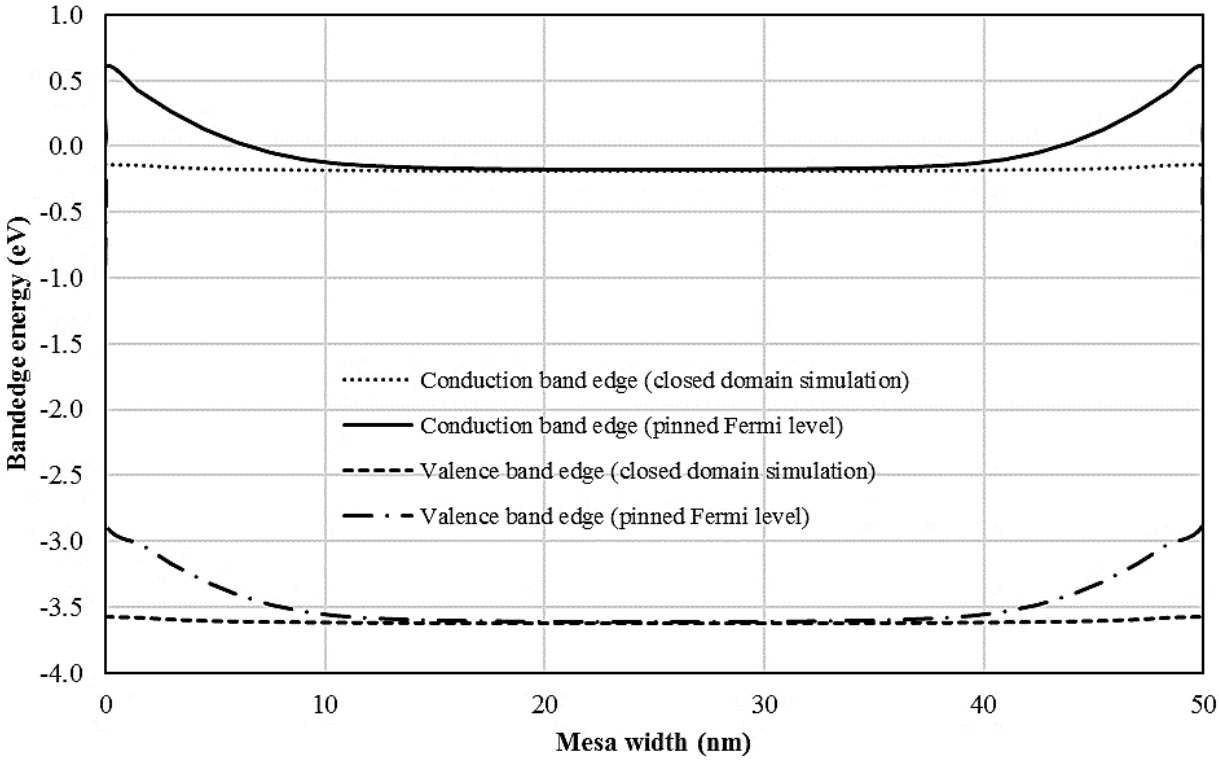

Figure 5.16 - Position of band edges in an island nanowire of 2500 nm^2 top surface area of 20 nm thick $Al_{0.30}Ga_{0.70}N$ barrier, under two different conditions at the sidewalls. This cut is taken 1 nm below the interface in the GaN buffer in the middle of the heterostructure.

Figure 5.17 shows the electron concentration in a horizontal plane taken at the peak of the profile of carrier concentration for the five different top surface geometries of Figure 5.15. All nanowires have a 1600 nm^2 top surface area. All other parameters are kept alike (namely the Al mole fraction is 30%, AlGaN barrier is 20 nm thick and the Fermi level at sidewalls is pinned at 0.6 eV). In this figure, the white line represents the boundaries of the mesa. The lowering of the 2DEG at the sidewalls is evident among all five panels of the figure. Among these, most importantly one sees the difference among the peak concentrations agreeing with the speculations of [11]. Along the order of variation of perimeter-to-area ratio of the top surface are, the triangular prism shows the smallest peak concentration compared to the cylindrical heterostructure. However, at the same time one sees among these geometries that for a fixed surface area as the sidewalls get closer to

center of the mesa a lower electron concentration is observed. This is in agreement with the triple gate effect presented in [27]. As an example, for the same surface area sidewall to center distance of a cylinder and an island-isolation feature keep a ratio of 1 to 0.89, promising further depletion in case of an island. Hence, our job in the simulations to follow is to differentiate these effects.

As was mentioned before, depletion at the sidewalls has been counted as one of the causes for lowering the sheet charge density. The other cause, as in [10] has been speculated of being the lowering of the piezoelectric polarization due to edge effects. The latter cause is highlighted in Figure 5.18 where the hydrostatic strain in the barrier is shown for island-shaped nanowires of 1600 nm^2 and 4900 nm^2 top surface area. The cut is taken at 1.5 nm[34] above the heterojunction in the middle of the respective structures. Here, the hydrostatic strain is depicted since it encompasses the different components coming into the evaluation of the piezoelectric polarization. For both devices, there is a clear spike in the hydrostatic strain at the sidewalls. It is worth noting that the height of this spike is smaller for the 1600 nm^2 heterostructure leading to lower hydrostatic strain near the sidewalls for smaller structures. As speculated in [10] and [11], the simulations show that as the device size shrinks the strain relaxation happening at the sidewalls leads also to a greater reduction of strain in the middle of the device [24].

[34] This distance offers a representative display of the hydrostatic strain in the barrier.

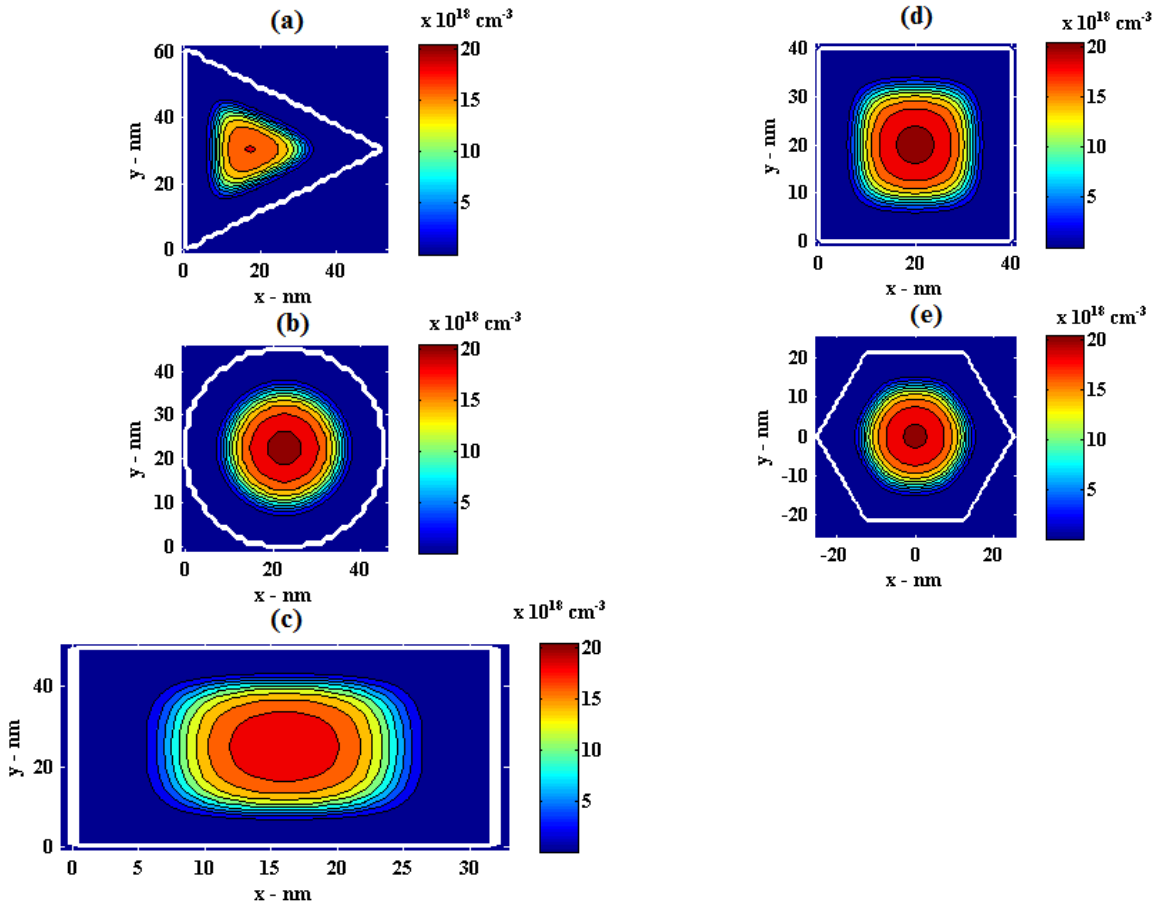

Figure 5.17 - Electron concentration (in 10^{18} cm^{-3}) in the horizontal peak plane below the heterointerface for five geometries. The white lines on each panel represent the extent of the structures. All structures have a 20 nm thick $Al_{0.30}Ga_{0.70}N$ barrier. The Fermi level pinning is set at 0.6 eV below E_c. The nanowires are of (a) triangular prism, (b) cylinder, (c) fin-like, (d) island-isolated, and (e) hexagonal geometries.

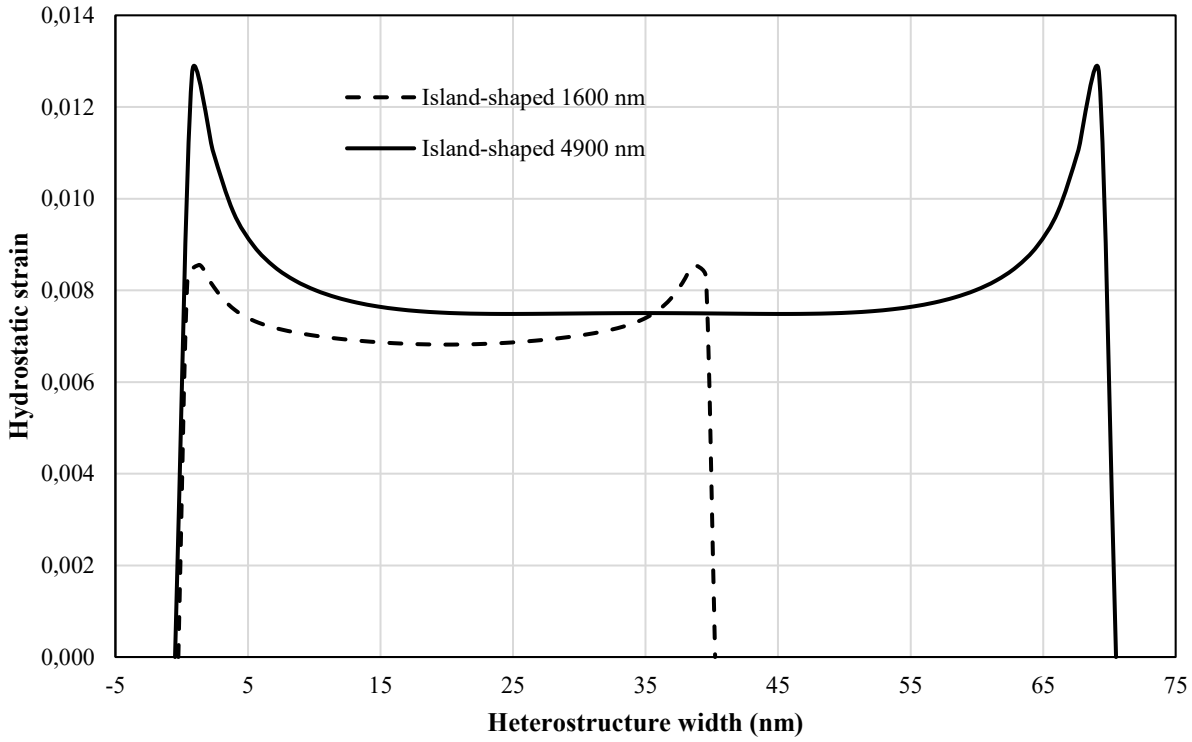

Figure 5.18 - Hydrostatic strain in the barrier for a central horizontal cut 1.5 nm above the heterointerface for two island-shaped heterostructures of different top surface areas. Strain minimization algorithm is in effect and simulation domain is closed (no band-bending due to Fermi-level pinning).

5.3.2 Assessing the impact of conduction band pinning at the sidewalls

In section 5.2, the perimeter-to-area metric was presented and used to compare the island- and fin-isolated HFETs, whose structure region fitted exactly the simulation region. The boundary conditions on the strain algorithm and wave functions stayed the same as was previously defined in chapter 3, namely Neumann[35] and Dirichlet[36] boundary conditions, respectively. The conditions at the sidewalls reflected the "closed domain simulation" as shown in Figure 5.16. In Figure 5.17, however, the Fermi level of all five structures was pinned at 0.6 eV below the conduction band edge. Although this replicates the effect of dangling bonds at the sidewalls, it prevents us from

[35] It implies that there is no external strain applied at the sidewalls.
[36] It implies that the wave functions are confined within the quantum region, namely that $\psi(x_b) = 0$ where x_b is the position of the boundary.

singling out the effect of peel forces at the corners. Since the results shown earlier (i.e. in section 5.2) demonstrate the need for further investigation of a possible link between the peel forces developing at the corners of the isolation feature and the sheet charge density, it is mandatory to use sidewalls boundary conditions that offer such an opportunity. To accomplish this goal, simulations whose simulation domain are termed as "open"[37] are considered along those that are referred to as "close" and "pinned". In case of island isolation features, the results of these simulations are shown in Figure 5.19. On this figure, one notices only a slight disagreement between $y = 0$ and $y = 4$ nm for the conduction band edges calculated according to the closed simulation domain and the "open" simulation domain assumptions where the AlGaN/GaN HFET sidewalls are left to relax into air. This slight disagreement is attributed to numerical simulations singularities. Based on this figure, one readily sees why the effect of corners would be difficult to notice using "pinned" sidewalls when the conduction band edge does not match the "closed" of "open" curves from $y = 0$ to $y \sim 12$ nm.

[37] The term "open" will refer to the simulation features presented in Figure 5.15, where the mesa geometry did not fill completely the simulation domain.

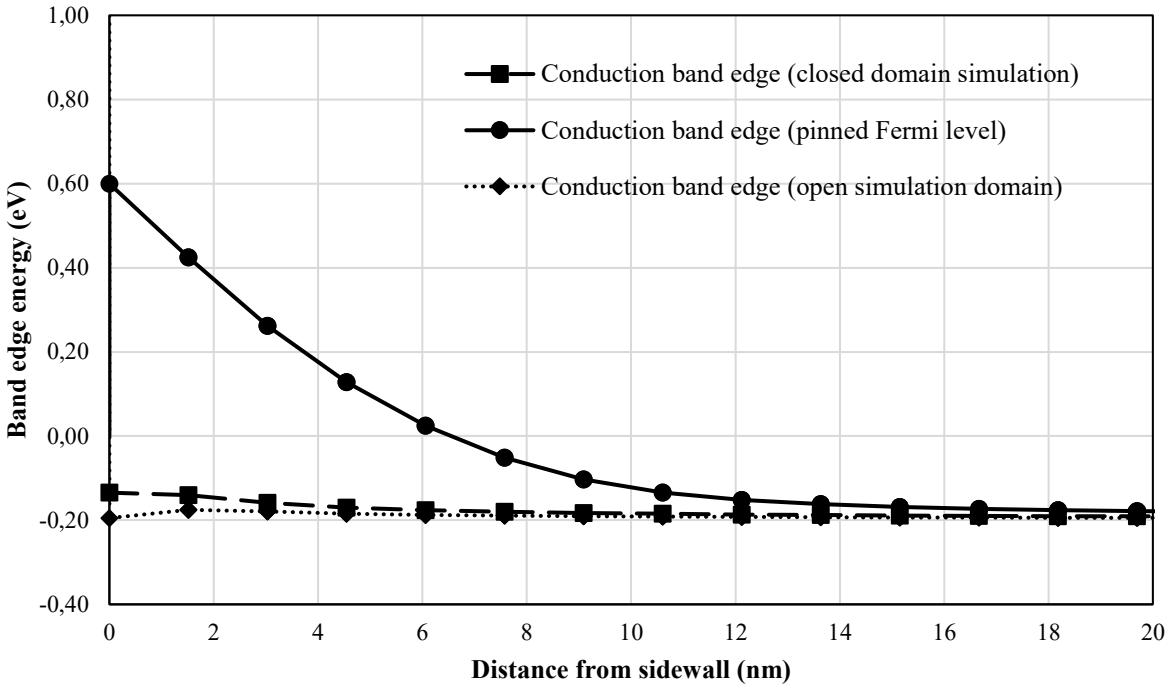

Figure 5.19 - Conduction band edge in an island-shaped AlGaN/GaN HFET, with 20 nm thick barrier whose aluminum mole fraction is 30%. 3-D simulations are presented for three simulation conditions.

The effect of the conduction band bending at the sidewalls due to the Fermi level pinning at 0.6 eV below E_C correlates directly to a drastic reduction of the average sheet charge. This is shown in Figure 5.20, where a vertical middle cut is taken through the island-isolated HFET structure (2500 nm^2 top surface area, 30% aluminum mole fraction, and 20 nm thick AlGaN barrier) under three different conditions at the sidewalls. In this case, the closed simulation domain presents an average sheet charge density of $5.0074 \times 10^{12}\ cm^{-2}$, while the open domain simulation boast a maximum sheet charge density of $6.0606 \times 10^{12}\ cm^{-2}$. The two lateral spikes in the open domain simulation curve are produced through numerical instabilities near the sidewalls. These spikes die out as the mesa size is increased.

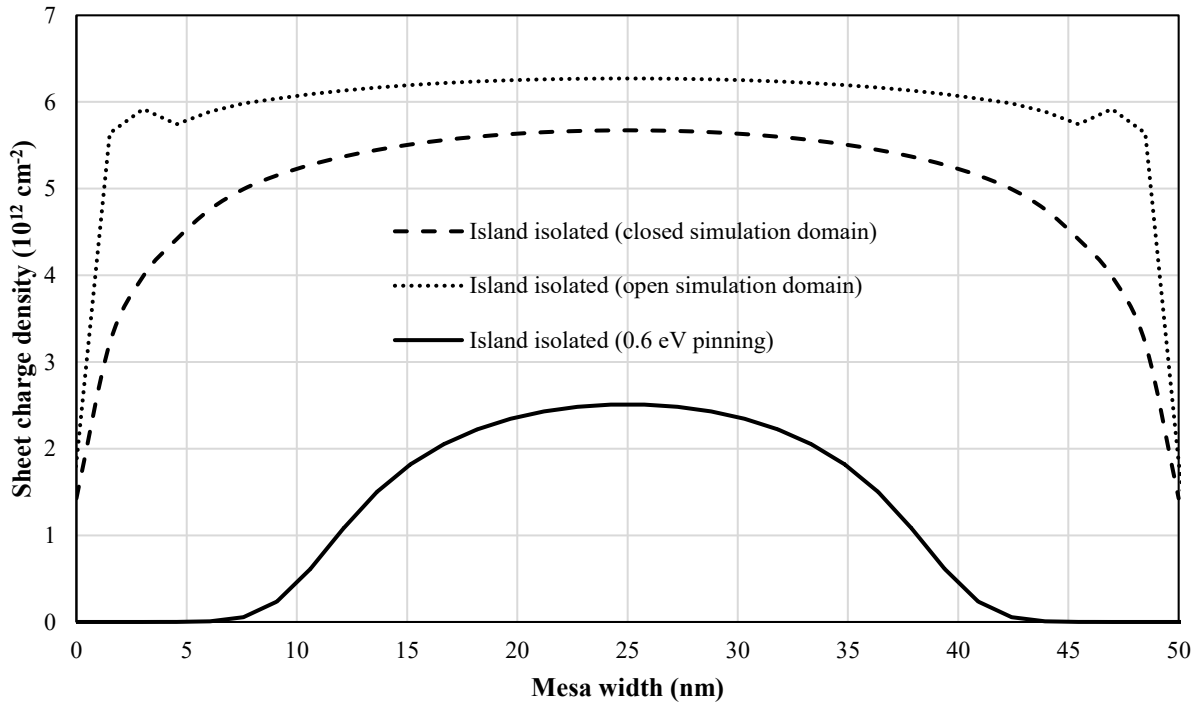

Figure 5.20 - Average sheet charge density for a vertical middle cut through an AlGaN/GaN HFET under three simulation conditions. The AlGaN/GaN heterostructure has a 2500 nm^2 top surface area, 20 nm thick AlGaN barrier and a 30% aluminum mole fraction. Among the three cases, strain minimization is in effect.

Figure 5.21 illustrates the impact of both the mesa geometry and the condition at the sidewalls on the average sheet charge density. In this figure, four heterostructures of similar top surface area (i.e. 1600 nm^2) of triangular-prism-shaped, island-shaped, hexagonal prism-shaped, and cylindrical-shaped are compared under the "pinned" and "open" conditions at the sidewalls. The heterostructures are arranged in the increasing order of perimeter-to-area ratio. The ratio between the average sheet charge density for "open" sidewall conditions and for "pinned" sidewall conditions ranges from 4.25 to 6.65 for the cylindrical-shaped and the triangular-prism shaped heterostructures, respectively. The average sheet charge density for heterostructures whose sidewalls are "open" increases somewhat with perimeter-to-area ratio for an identical cross-sectional area, indicating a possible influence of strain reduction due to peel forces. The average sheet charge density for heterostructures whose sidewalls are pinned, however, conversely

decreases along this order. This is coincidently in agreement with the greater proximity of the sidewall to the center of the isolation-feature. Based on the observations of Figure 5.21, what is of major importance is that, at least for this cross-sectional area, possible effect of peel-forces seems to be just a negligible fraction of the role that the sidewall pinning can play in altering the average 2DEG concentration of polar AlGaN/GaN heterojunctions. This trend indicates the importance of the triple-gate effect for small mesas.

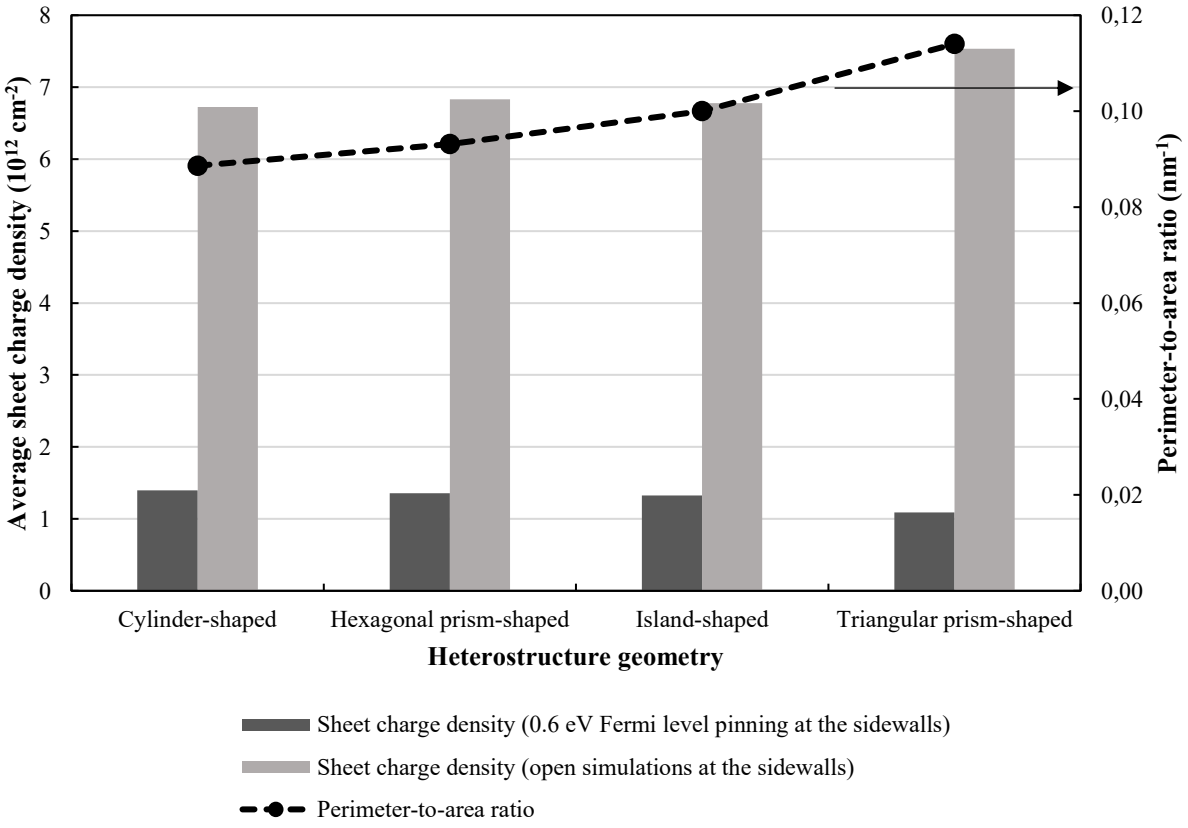

Figure 5.21 - Comparison between the sheet charge densities calculated for AlGaN/GaN heterostructures whose sidewalls are subjected to Fermi level pinning (0.6 eV below E_C) or not ("open"). Four different nanowire geometries of 1600 nm^2 cross-sectional area, are considered. Each structure has a 20 nm thick AlGaN barrier and 30% aluminum mole fraction in the AlGaN barrier. Strain minimization algorithm is in effect.

5.3.3 Reassessing the use of the perimeter-to-area ratio as a metric

In Figure 5.22 the average sheet charge density is shown with respect to cross-sectional area of island-, hexagonal prism-, and cylindrical-shaped AlGaN/GaN heterostructures. The AlGaN barrier is 20 nm thick and the aluminum mole fraction in the barrier is kept at 30%. The conditions at the sidewalls is set as "open". As expected, due to the increasing distance between the sidewall and the center of the mesa, the average sheet charge density increases with the top surface area. Whereas for the data presented in this figure no Fermi-level pinning is in effect, the dependence of the average sheet charge density on the feature geometry among all of the considered cross-sectional areas seem negligible.

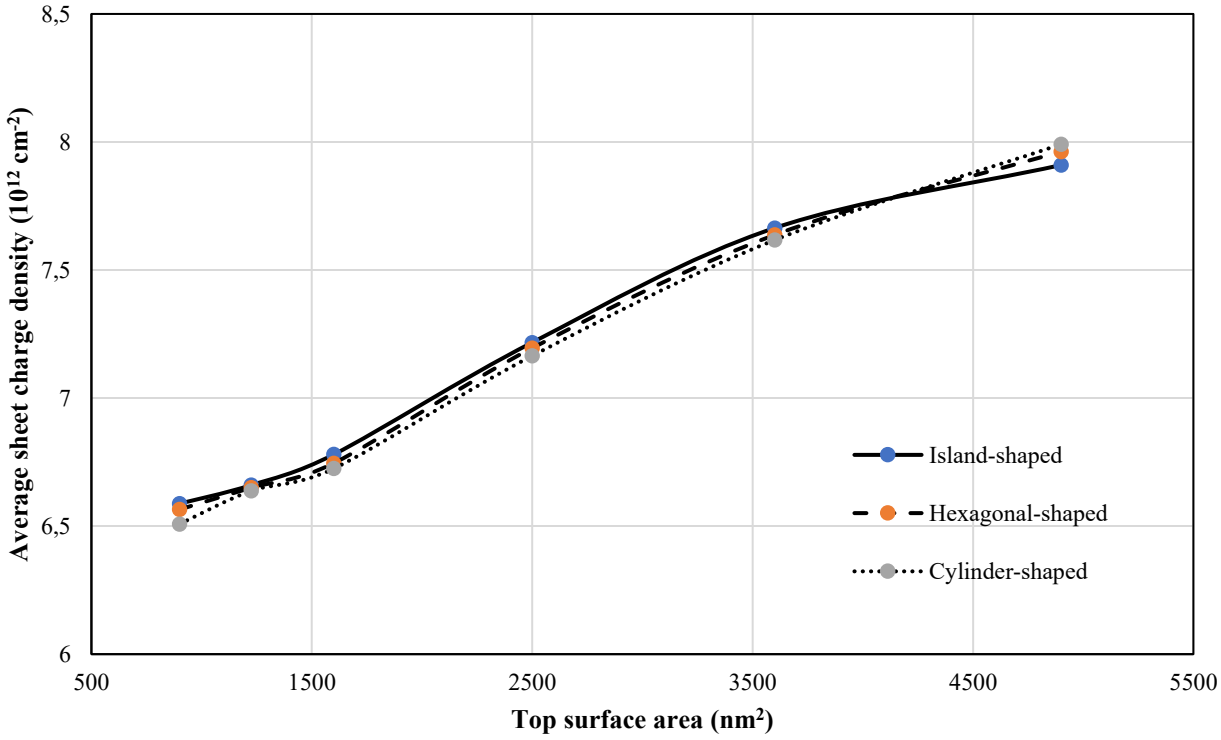

Figure 5.22 - Average sheet charge density versus top surface area for island-, cylindrical-, and hexagonal-shaped AlGaN/GaN heterostructures. The aluminum mole fraction is 30% in all cases with a 20 nm thick AlGaN barrier. The sidewall condition is set as "open". Strain minimization is in effect.

Figure 5.23 shows the average sheet charge density with respect to the perimeter-to-area ratio for island-shaped, hexagonal prism-, and cylindrical-shaped AlGaN/GaN heterostructures whose conditions at the sidewalls are set as "open". The AlGaN barrier is 20 nm thick and boasts a 30% aluminum mole fraction. As in [11], the higher the perimeter-to-area ratio, the lower the average sheet charge density. But what is in addition observed is that the rounding of isolation feature also results in a slight reduction in the average 2DEG concentration. While this observation is made, one should not miss the point that according to what was reported in Figure 5.21 all these factors are negligible compared to the ever more present role of sidewall pinning as the feature sizes shrink.

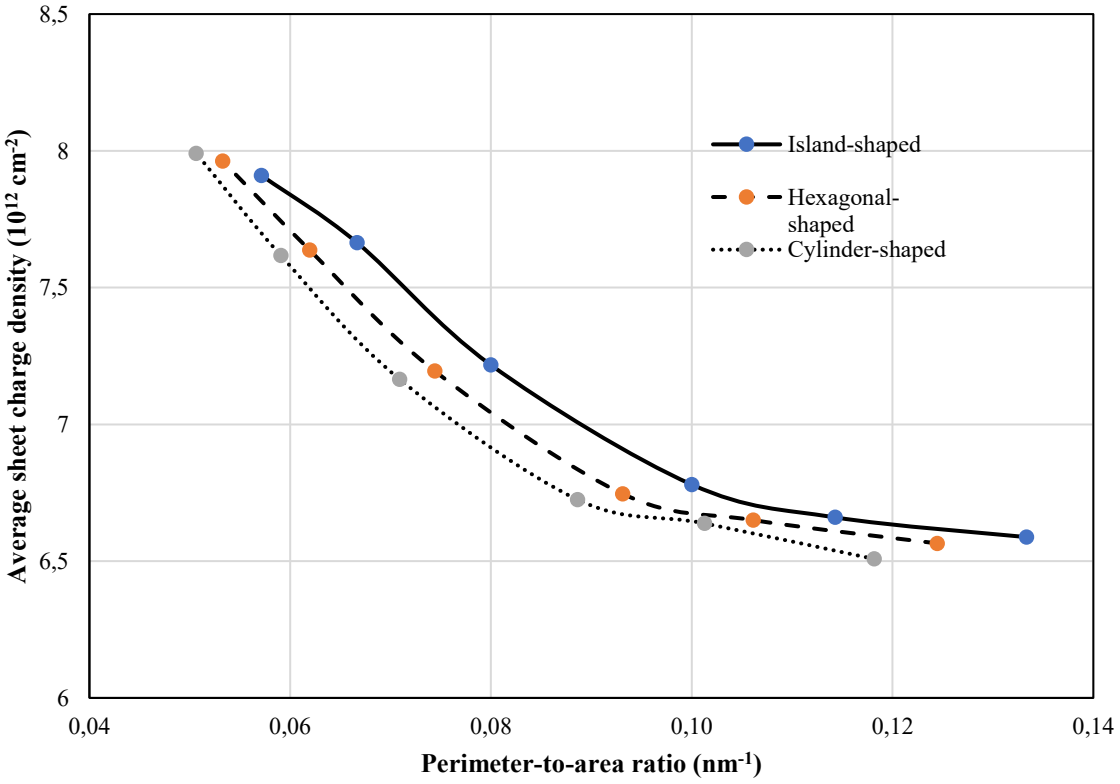

Figure 5.23 - Average sheet charge density versus perimeter-to-area ratio for island-, cylinder-, and hexagonal-shaped AlGaN/GaN heterostructures. The aluminum mole fraction is 30% in all cases with a 20 nm thick AlGaN barrier and sidewalls are set as "open". Strain minimization algorithm is in effect.

5.4 Threshold voltage calculations and results

5.4.1 Extracting threshold voltage from the average sheet charge density

Uncovering a trend between the threshold voltage and the geometry of the heterostructures described in this thesis is the primary goal of the works presented here. Towards this goal, as in [27], the average 2-DEG sheet charge density of the structures are calculated as a function of applied voltage on the top Schottky gate (i.e. V_G). As indicated earlier, since the considered structures in this chapter are three-dimensional, compared to the two-dimensional slices studied in [27], the equation defining this average quantity transforms to:

$$n_{sh-av} = \frac{1}{w_x w_y} \int_0^{w_x} \int_0^{w_y} n_{sh}(x,y)\ dx\ dy. \tag{5.1}$$

In [27], an average sheet charge density threshold of $n_{sh-Th} = 3 \times 10^{11}$ cm^{-2} is used to define the value of the threshold voltage. This criterion is also applied in the following pages. Thus, the threshold voltage will be obtained by extrapolating the linear part of the $n_{s_{av}} - V_G$ curves to the threshold sheet charge density. Figure 5.24 and Figure 5.25 show the calculated average sheet charge density for different heterostructures as the applied potential on the top Schottky barrier is changed. As indicated earlier, among all of the simulations presented in this section the whole top surface area of the heterostructure is subject to the applied potential. The conditions at the sidewall are either termed as “open” or “pinned”.

In Figure 5.24, the average sheet charge density is plotted as a function of the applied top surface potential for heterostructures of different geometries but similar top surface area (i.e. 1225 nm^2) and for sidewall conditions termed as “open”. As explained above, from those curves, it is possible to extract a threshold voltage when the linear portion is extrapolated to reach n_{sh-Th}. From Figure

5.24, one sees that the slopes for all three geometries are extremely close, indicating only a small variation in the threshold voltage among these heterostructures.

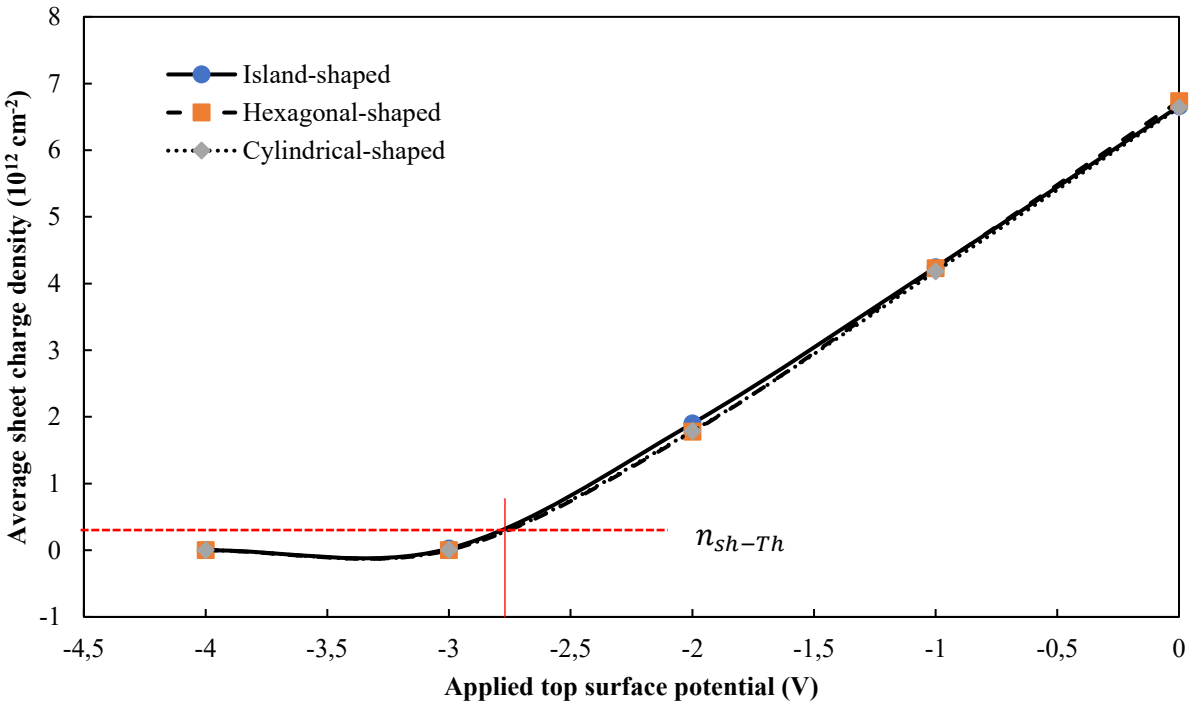

Figure 5.24 – Average sheet charge density versus the applied surface potential on the top gate for island-, hexagonal prism- and cylindrical-shaped AlGaN/GaN heterostructures of 1225 nm^2 top surface area. The Fermi level at the sidewalls is considered floating. Strain minimization algorithm is in effect. Aluminum mole fraction and AlGaN barrier thickness are 30% and 20 nm, respectively.

The average sheet charge density versus the applied top surface potential is shown in Figure 5.25 for island-, hexagonal-, and cylindrical-shaped heterostructures of 14 nm and 20 nm thick AlGaN barriers whose sidewall conditions are “pinned”. Whereas a less negative threshold voltage is expected from the heterostructures of thinner barrier, the difference between the three geometries for the case of pinned sidewall conditions is very negligible. This is not unlike the observations made on Figure 5.24. What is noteworthy is that for an identical top surface area, aluminum mole fraction and barrier thickness, the value of the threshold voltage when the sidewalls are pinned is

substantially less negative, independent of the lateral geometry. This difference is of the order of 0.94 V for 1225 nm^2 top surface area island-shaped heterostructures.

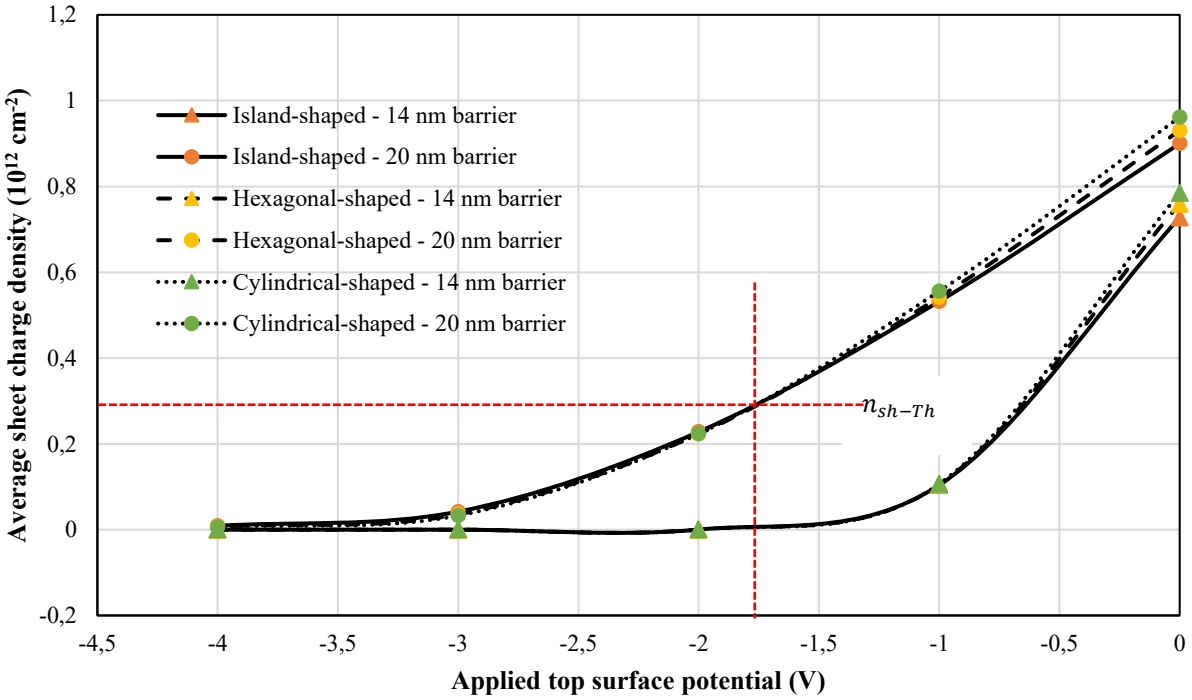

Figure 5.25 –Influence of AlGaN barrier thickness on the threshold voltage. Average sheet charge density is shown as a function of applied surface potential at the top gate for island-, hexagonal-, and cylindrical-shaped heterostructures of 1225 nm^2 top surface area. The Fermi level at the sidewalls is pinned at 0.6 eV below conduction band level. Strain minimization algorithm is in effect and aluminum mole fraction in the barrier is 30%.

5.4.2 Influence of mesa geometry and size, AlGaN barrier thickness, and of aluminum mole fraction on the threshold voltage

Using the extrapolation procedure explained above, it is possible to extract the threshold voltage of the simulated heterostructures. The influence of the mesa-isolation size and geometry is shown in Figure 5.26 and Figure 5.27, where the threshold voltage is plotted versus the top surface area and perimeter-to-area ratio, respectively. As already identified in [27] for the case of two-dimensional version of simulation, with decreasing mesa size comes a less negative threshold voltage thanks to sidewall depletion.

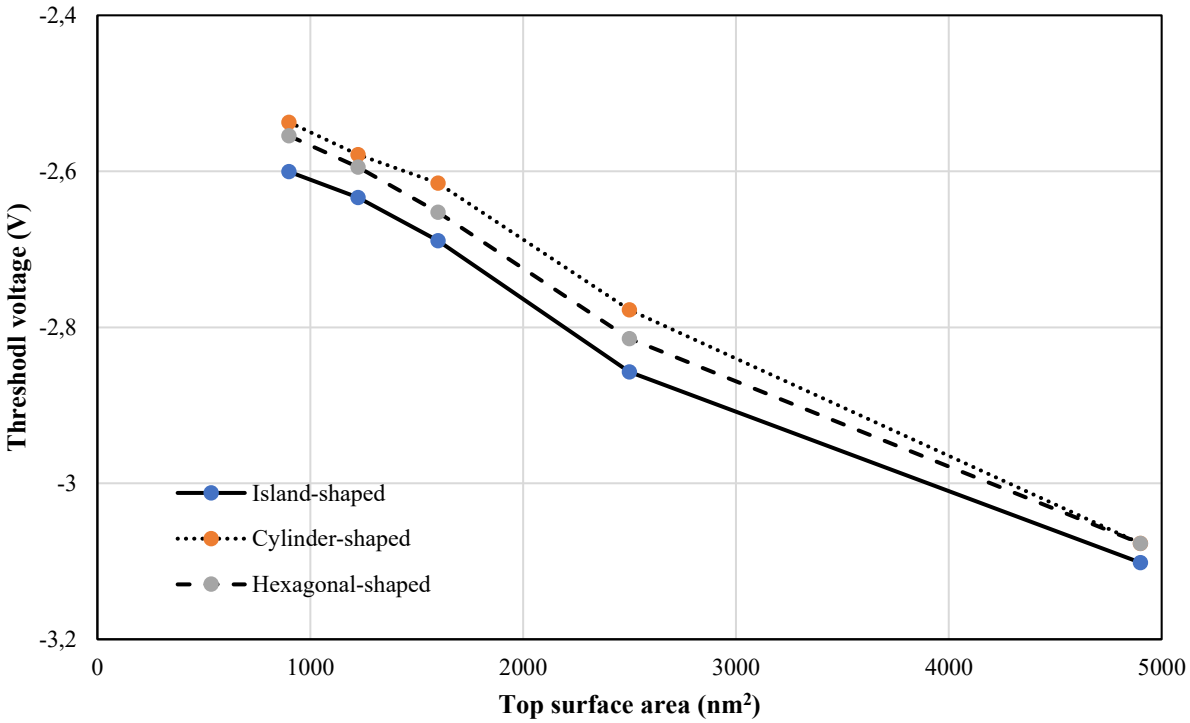

Figure 5.26 - Influence of top surface area on the threshold voltage of island-, hexagonal-, and cylindrical-shaped AlGaN/GaN heterostructures. The sidewalls are set as "open". The AlGaN barrier thickness is 20 nm and the aluminum mole fraction is 30%. Strain minimization algorithm is in effect.

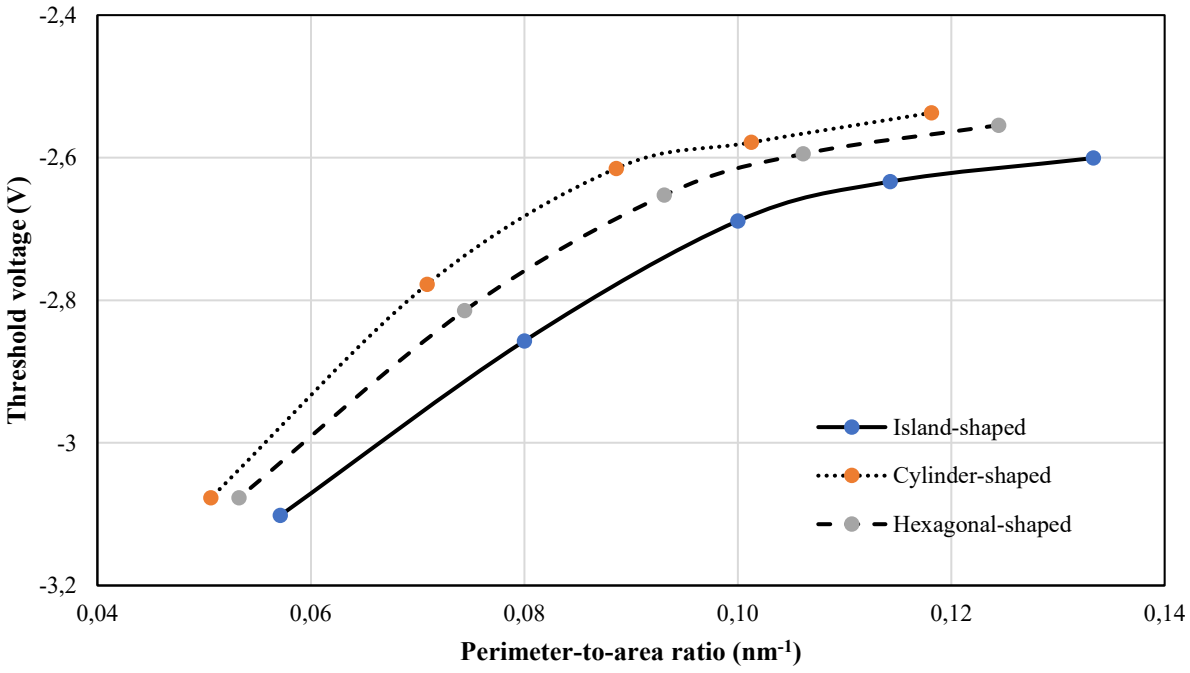

Figure 5.27 - Influence of perimeter-to-area ratio on the threshold voltage for island-, hexagonal-, and cylindrical-shaped AlGaN/GaN heterostructures of different top surface areas. The sidewalls are set as "open". The AlGaN barrier thickness is 20 nm and the aluminum mole fraction is 30%. Strain minimization algorithm is in effect.

To differentiate between the two mechanisms, information is provided in Figure 5.28 and Figure 5.29 when the sidewall depletion (pinning) is allowed to accompany strain relaxation in the form of changes in the mesa geometry and sizes. Once more, the results presented in these figures indicate that the influence of geometry on the threshold voltage is superseded by the influence of Fermi-level pinning at the sidewalls. Moreover, in Figure 5.28, it is possible to observe a bending in the threshold voltage-top surface area curves that is different from the one in Figure 5.26. This bending resembles the one shown in [27] where sidewall depletion was allowed thanks to a triple-gate geometry.

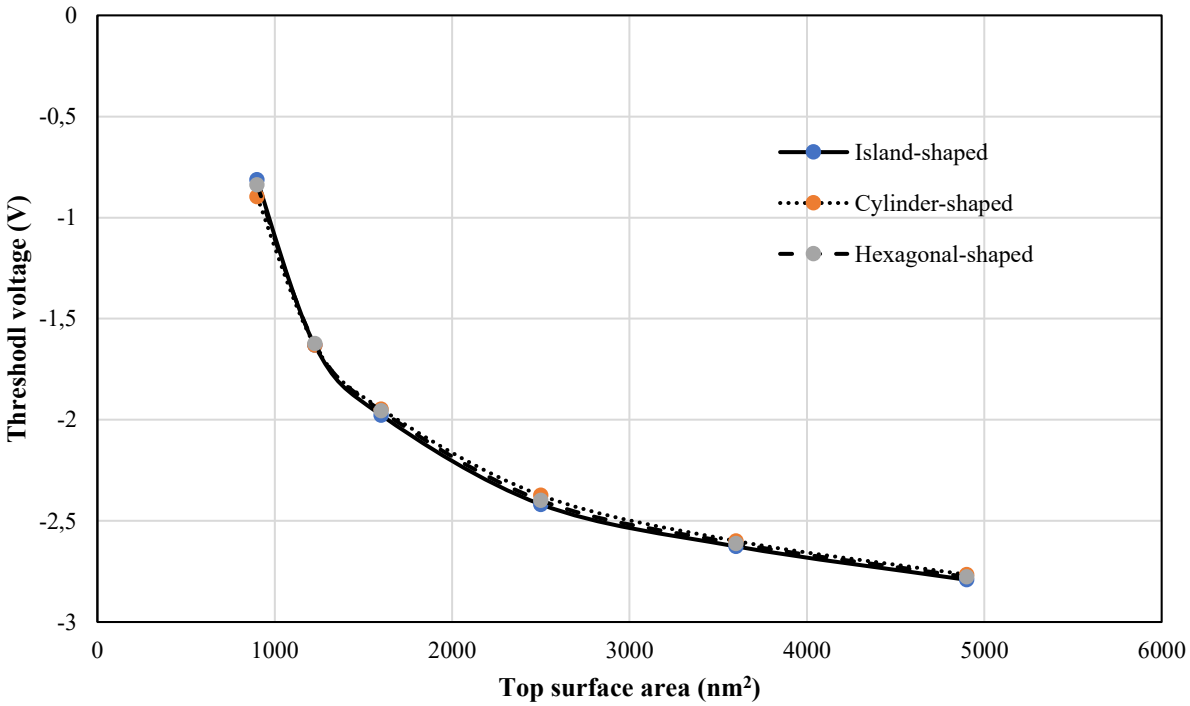

Figure 5.28 - Influence of top surface area on the threshold voltage of island-, hexagonal-, and cylindrical-shaped AlGaN/GaN heterostructures. The sidewalls are pinned at 0.6 eV below the conduction band level. The AlGaN barrier thickness is 20 nm and the aluminum mole fraction is 30%. Strain minimization algorithm is in effect.

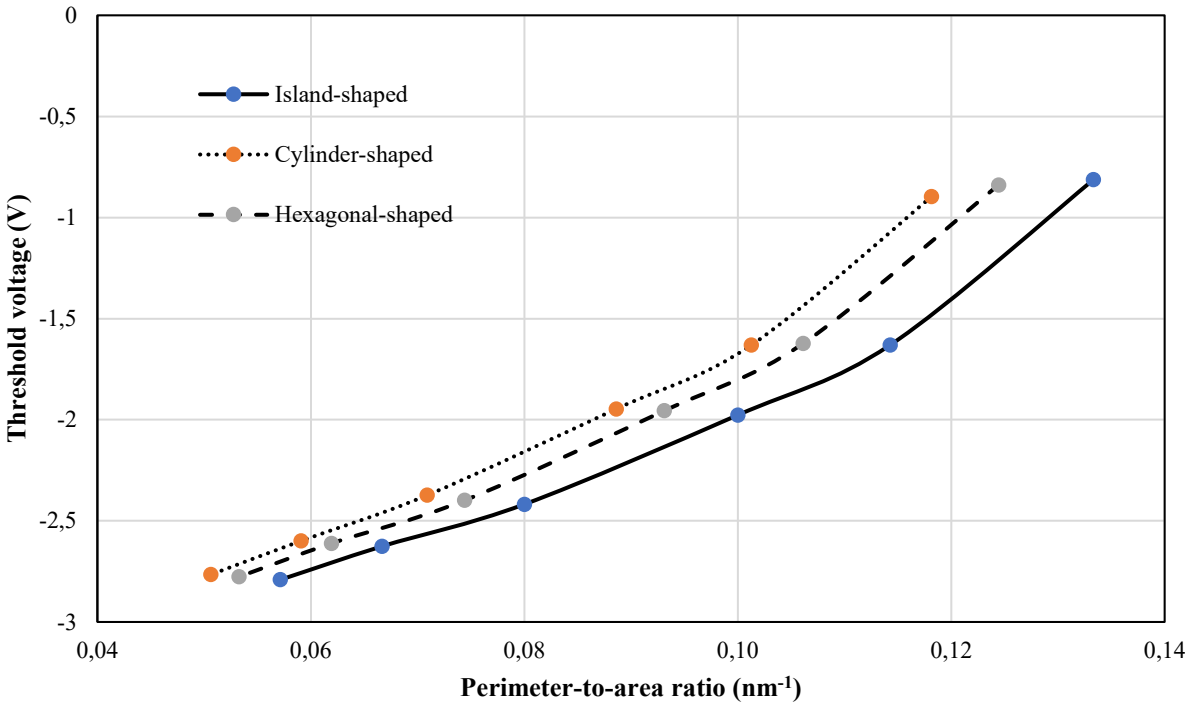

Figure 5.29 - Influence of perimeter-to-area ratio on the threshold voltage of island-, hexagonal-, and cylindrical-shaped AlGaN/GaN heterostructures. The sidewalls are pinned at 0.6 eV below the conduction band level. The AlGaN barrier thickness is 20 nm and the aluminum mole fraction is 30%. Strain minimization algorithm is in effect.

Figure 5.30 further highlights these observations. In here one can clearly see that while strain minimization alone is only capable of inducing less than 0.5 V shift in the threshold voltage as the lateral dimension of the mesa changes from 30 nm to 70 nm, for surface areas smaller than 900 nm^2 a much steeper variation of threshold voltage can be expected if the sidewalls are pinned at 0.6 eV below E_C. These results are, in terms of trend, comparable to those of [27].

What is the major outcome of the 3-D simulations reported in this chapter is that, compared to the effect of side-gating caused by Fermi-level pinning strain-minimization and variation of the roundness of the isolation feature geometry will only have a negligible effect on the threshold voltage.

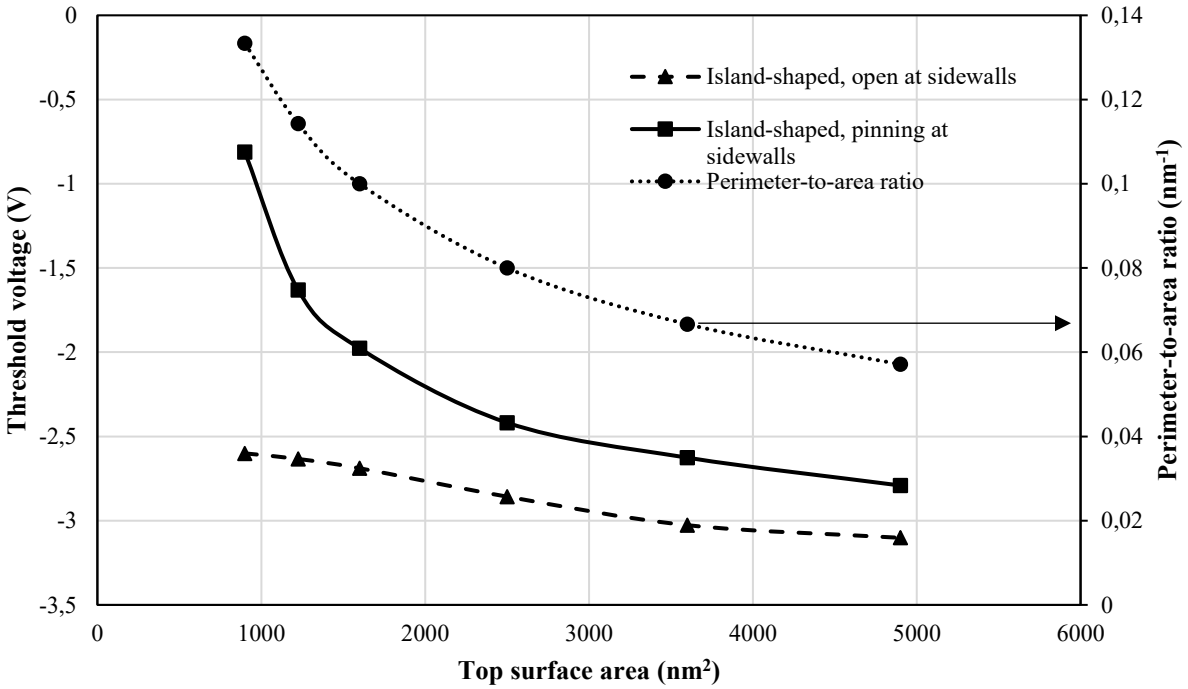

Figure 5.30 - Influence of sidewall conditions on the threshold voltage with respect to the top surface area for island-shaped AlGaN/GaN heterostructure with 30% aluminum mole fraction on a 20 nm thick AlGaN barrier. The perimeter-to-area ratio is indicated as a reference metric. Strain-minimization algorithm is in effect.

5.4.3 The effect of geometry and size on the hydrostatic pressure

In this section, the hydrostatic pressure in the AlGaN barrier is calculated for AlGaN/GaN heterostructures of decreasing mesa size for the three types of nanowire geometry. The hydrostatic pressure plays the role of an indicator for strain in the barrier. The point by point hydrostatic pressure is integrated and averaged to yield the mean hydrostatic pressure for each heterostructure. Figure 5.31 compares the mean hydrostatic pressure in the AlGaN barrier for each heterostructure to a reference value which is set as the average hydrostatic pressure in the AlGaN barrier of an island-shaped AlGaN/GaN heterostructure with cross-sectional area of 900 nm^2, AlGaN barrier thickness of 20 nm and aluminum mole fraction of 30%. Figure 5.31 shows how the average hydrostatic pressure in the barrier is a roughly 2.2 times higher for all three heterostructure geometries whose cross-sectional area is 4900 nm^2 compared with this reference value. Although

an increase in the average hydrostatic pressure is observed with the heterostructure cross-sectional area, almost no difference is observed across heterostructures of different geometry. The observed reduction in the average hydrostatic pressure for isolation-features of smaller cross-sectional area can be of value in reducing some of the long-term reliability concerns of AlGaN/GaN HFETs. Oftentimes, in correlation with the difference among the thermal expansion coefficients of the two constituents of the heterostructure, this pressure is linked with crack formation in AlGaN/GaN HFETs undergoing self-heating during high-power operation.

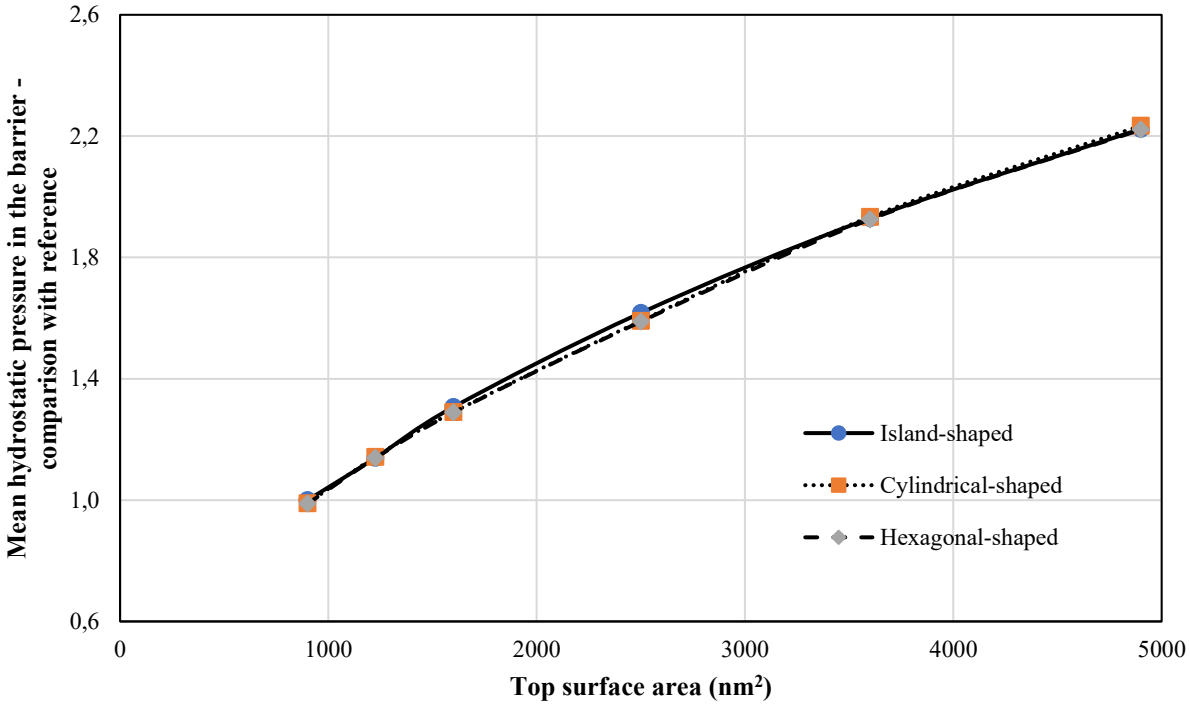

Figure 5.31 - Average hydrostatic pressure in the barrier for island-, hexagonal-, and cylindrical-shaped AlGaN-GaN heterostructures of increasing top surface area compared with a reference value. The reference value is set at the average hydrostatic pressure in the barrier of an island-shaped heterostructures whose top surface area is 900 nm^2. The aluminum mole fraction is 30% and the AlGaN barrier thickness is 20 nm for all heterostructures. Strain minimization algorithm is in effect.

5.5 Conclusion

In this chapter, the *nextnano* environment was used to simulate three-dimensional versions of AlGaN/GaN heterostructures. In terms of the observations made, we reach the conclusion that strain reduction at the boundaries of the isolation feature and its correlation with the feature geometry (and its degree of roundness) has negligible impact on shifting the threshold voltage, compared to what sidewall Fermi-level pinning induces at small lateral mesa dimensions.

Chapter 6

Conclusion and future works

In this final chapter, first the concluding remarks of this work are highlighted. Following this, ideas for possible developments related to this thesis are presented. Going a step further than ternary materials, quaternaries allow for independent control of strain and band gap in $Al_xIn_yGa_{1-x-y}N$-based heterostructures. Staying in the realm of ternaries, other physics-based simulation frameworks are proposed.

6.1 Conclusion

The influence of mesa-isolation shape and size on the 2DEG has been studied using physics-based simulations. A differentiation between two mechanisms, strain relaxation and triple-gate effect, impacting threshold voltage in AlGaN/GaN heterostructures has been suggested. It was shown that, as the cross-sectional area of three different geometries was reduced from 4900 nm^2 to 900 nm^2, it was possible to reach a threshold voltage of -0.81 V in the case of an island-shaped heterostructure whose condition at the sidewalls mimicked those of triple-gated devices. While demonstrating a certain degree of correlation between strain and both feature size and geometry of the isolation feature, this detailed investigation highlights a much greater role for the aluminum mole fraction,

barrier thickness and sidewall gating (when the lateral size of the feature is below 4900 nm^2) in determining the threshold voltage. One concern with AlGaN/GaN heterostructures is the difference in the coefficient of thermal expansion between AlGaN and GaN that leads to defects at the interface when the devices are operated at high temperatures. The reduction in mesa size would definitely be less problematic on the point of view of reliability thanks to overall strain reduction in the barrier with reduction in mesa size leading to a drop in average hydrostratic pressure.

6.2 Future works

6.2.1 Quaternary materials

Introducing InN into AlGaN-based devices does not simply imply a linear adjustment of the optoelectronic properties of the resulting quaternary. InN's narrow band gap (~0.7 eV) and large electron affinity (4.7 and 4.6 eV for In- and N-polar surfaces respectively) do not merely call for a change in parameters [60] [61] [62]. As was shown in [61], thorough theoretical work is still needed to understand the conduction band discontinuity or the carrier confinement in the In-containing 2DEG.

Altering the input files presented in chapter 3, it is possible to simulate lattice-matched quaternary devices. Preliminary results are shown in Figure 6.1 and Figure 6.2. In the first graph, the conduction band edge is plotted along the depth of the mesa for an $Al_{0.30}In_{0.07}Ga_{0.63}N$ /GaN one-dimensional heterostructure, whose barrier thickness varies between 12 and 20 nm. For 12 nm thick barrier, the bottom of the quantum well almost reaches the Fermi level (0.00257 eV), while

the 20 nm thick barrier heterostructure has a minima at -0.10993 eV for a conduction band discontinuity of: $\Delta E_C = 0.1865$ eV.

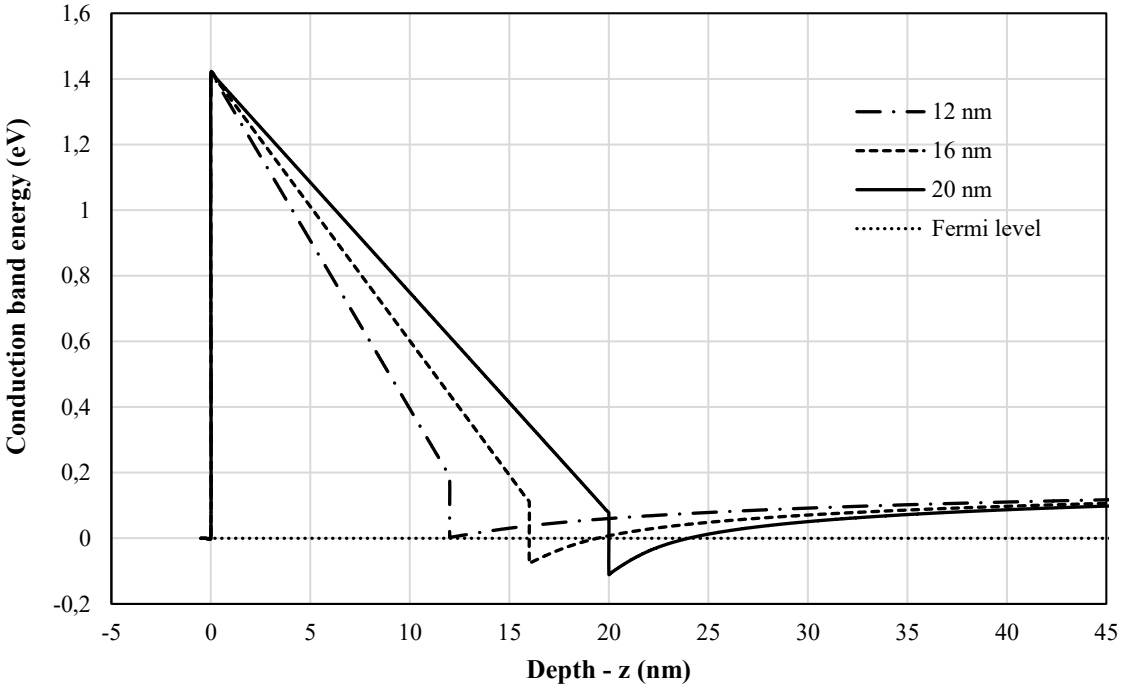

Figure 6.1 - Conduction band energy (eV) versus depth in a $Al_{0.3}In_{0.07}Ga_{0.63}N$/GaN mesas for three different AlInGaN barrier thicknesses.

Figure 6.2 shows the conduction band edges for two barrier compositions. Higher AlN and InN (thus reduced GaN) mole fractions result in a deeper quantum well and higher electron concentration: 9.612×10^{12} cm^{-2} for $Al_{0.60}In_{0.13}Ga_{0.27}N$ compared to 1.727×10^{12} cm^{-2} for $Al_{0.30}In_{0.07}Ga_{0.63}N$ heterostructures. It is clear how the changes in the barrier composition affect the polarization, thus the sheet charge density and how they can lead to higher (more positive) threshold voltages. One can imagine that carrier confinement values in the 2DEG can be extracted for lattice-matched devices and that the influence of barrier thickness can be determined. Also, refinements need to be made concerning the value of ΔE_C. Finally, due to concerns with the strain calculations implemented in one-dimension in *nextnano*, only lattice-matched devices were

simulated. Better control over this calculation and extension to two- or three-dimensions could produce interesting results.

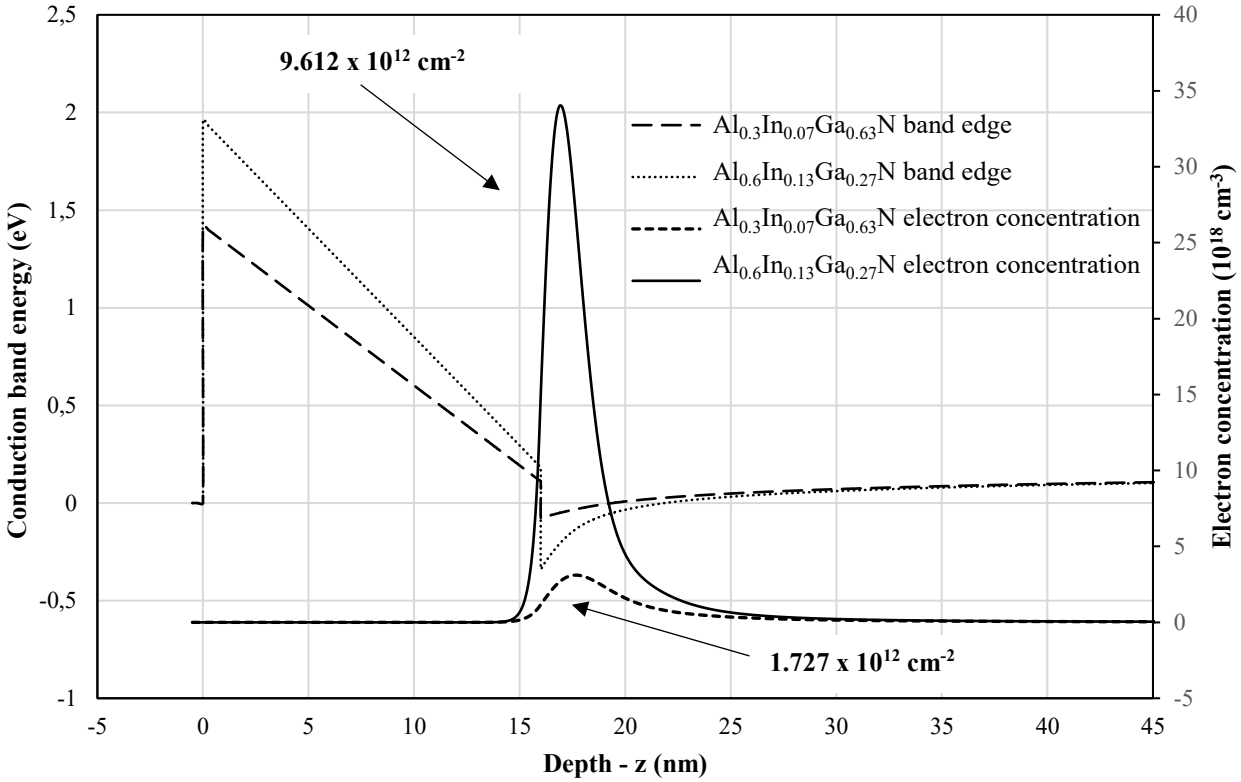

Figure 6.2 - Conduction band edges (eV) and electron concentration (10^{18} cm^{-3}) for two quaternary heterostructures with 16 nm thick barriers.

6.2.2 Mesa geometries

Other potential simulations could be related to imperfections that arise when etching fins. Depending on the etching method [63], the sidewalls could be slightly sloped at an angle θ as shown in Figure 6.3. The effect slanted sidewalls have on the 2DEG and the threshold voltage is starting to gain some attention [64], but significant advances still remain to be done.

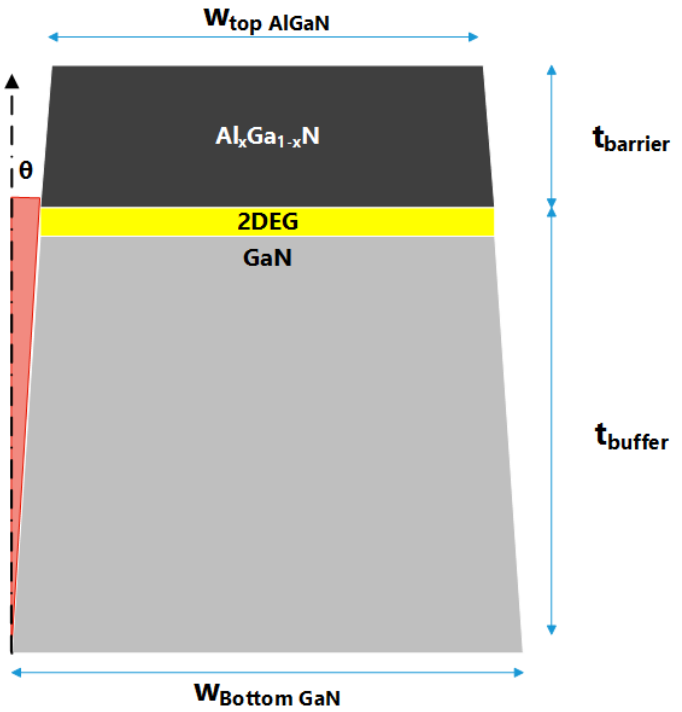

Figure 6.3 – Cross-section of a potential two- or three- dimensional simulation including effect of slanted sidewalls.

Crystal orientation plays an important role on the piezoelectric field and electronic properties determination [65] [66]. Better theoretical models are required to understand the 2DEG characteristics of newly developed vertical GaN transistors built in [67].

6.2.3 Triple-gate devices

Minor modifications to the input files used in this work would allow one to study the triple-gate effect on two- and, most importantly on three-dimensional mesas. It would be possible to isolate the contributions of tri-gate design and piezoelectric reduction due to corners in a theoretical framework. Recent papers report normally-off operation for triple-gate GaN-based devices [28] [68]. Other atypical gate and/or fin geometries could also be studied, namely vertical GaN

transistors [67] and delta shaped nanowire fin-shaped FETs [69] [70]. Those geometries allow for increased electrostatic control over the gate and reduced short-channel effects.

Finally, most recent fabricated GaN FETs introduce different gate dielectrics whose composition, thicknesses, shapes must be studied to optimize device parameters [28, 68, 67, 69, 70].

Bibliography

[1] T. Mimura, "The Early History of the High Electron Mobility Transistor," *IEEE Transactions on Microwave Theory and Techniques,* vol. 50, no. 3, pp. 780-782, 2002.

[2] T. Mimura, S. Hiyamizu, T. Fujii, and K. Nanbu, "A new field-effect transistor with selectively doped GaAs/n-AlGaAs heterojunctions," *Japanese Journal of Applied Physics,* vol. 19, no. 5, pp. L225-L227, 1980.

[3] R. Courtland, "Gallium Nitride Power Transistors Priced Cheaper Than Silicon," 8 May 2015. [Online]. Available: http://spectrum.ieee.org/tech-talk/semiconductors/design/gallium-nitride-transistors-priced-cheaper-than-silicon. [Accessed 06 07 2017].

[4] R. Muller, T. Kamins, and M. Chan, Device Electronics for Integrated Circuits, 3rd ed., New York: John Wiley & Sons, 2003.

[5] I. Vurgaftman, J. Meyer, and L. Ram-Mohan, "Band Parameters for III-V compund semiconductors and their alloys," *Journal of Applied Physics,* vol. 89, no. 11, pp. 5815-5875, 2001.

[6] J. Piprek, Nitride Semiconductor Devices - Principles and Simulations, Berlin: Wiley-VCH, 2007.

[7] S. Birner, *Modeling of semiconductor nanostructures and semiconductor-electrolyte interfaces,* Munich: Technische Universitat Munchen, 2011.

[8] S. Birner, T. Zibold, T. Andlauer, T. Kubis, M. Sabathil, A. Trellakis, and P. Vogl, "nextnano: General Purpose 3-D Simulations," *IEEE Transactions on Electron Devices,* vol. 54, no. 9, pp. 2137-2142, 2007.

[9] P. Vogl, A. Trellakis, T. Zibold, T. Andlauer, S. Birner, K. R. Smith, and R. Morschl, "The 3D nanometer device project nextnano: Concepts, methods, results," *J Comput Electron,* vol. 5, pp. 285-289, 2006.

[10] P. Valizadeh and B. AlOtaibi, "Fin- and Island-Isolated AlGaN/GaN HFETs," *IEEE Transactions on Electron Devices,* vol. 58, no. 5, pp. 1404-1407, 2011.

[11] A. Loghmany and P. Valizadeh, "Alternative isolation-feature geometries and polarization-engineering of polar AlGaN/GaN HFETs," *Solid-State Electronics,* vol. 103, pp. 162-166, 2015.

[12] I. Vurgaftman and J. Meyer, "Band parameters for nitrogen-containing semiconductors," *Journal of Applied Physics,* vol. 94, no. 6, pp. 3675-3696, 2003.

[13] T. Hanada, "Basic Properties of ZnO, GaN and Related Materials," in *Oxide and Nitride Semiconductors - Processing, Properties, and Applications*, Berlin, Springer, 2009, pp. 1-20.

[14] O. Ambacher, J. Smart, and R. Shealy, "Two-dimensional electron gases induced by spontaneous and piezoelectric charges in N- and G-face AlGaN/GaN heterostructures," *Journal of Applied Physics,* vol. 15, no. 6, pp. 3222-3233, 1999.

[15] S. A. Campbell, Fabrication Engineering at the Micro- and Nanoscale, New York: Oxford University Press, 2008.

[16] O. Ambacher, J. Majewski, C. Miskys, A. Link, M. Hermann, M. Eickhoff, M. Stutzmann, F. Bernardini, V. Fiorentini, and V. Tilak, "Pyroelectric properties of Al(In)GaN/GaN hetero- and quantum well structures," *Journal of Physics: Condensed Matter,* vol. 14, pp. 3399-3434, 2002.

[17] F. Bernardini, "Spontaneous and Piezoelectric Polarization: Basic Theory vs. Practical Recipes," in *Nitride Semiconductor Devices - Principles and Simulations*, Weinheim, Wiley-VCH, 2007, pp. 49-68.

[18] R. King-Smith and D. Vanderbilt, "Theory of polarization of crystalline solids," *Physical Review B,* vol. 47, no. 3, pp. 1651-1654, 1993.

[19] L. Landau and E. Lifshitz, Electrodynamics of continuous media - 2nd edition, Moscow: Pergamon Press, 1984.

[20] S. Elliot, The Physics and Chemistry of Solids, Chichester, UK: John Wiley & Sons, 2006.

[21] F. Bernardini, V. Fiorentini, and D. Vanderbilt, "Spontaneous polarization and piezoelectric constants of III-V nitrides," *Physical Review B,* vol. 56, no. 16, pp. 24-27, 1997.

[22] O. Ambacher, B. Foutz, J. Smart, J. Shealy, and N. Weimann, "Two dimensional electron gases induced by spontaneous and piezoelectric polarization in undoped and doped AlGaN/GaN heterostructures," *Journal of Applied Physics,* vol. 87, no. 1, pp. 334-344, 2000.

[23] F. Bernardini and V. Fiorentini, "Nonlinear macroscopic polarization in III-V nitride alloys," *Physical Review B,* vol. 64, p. 085207, 2001.

[24] S. Joglekar, M. Azize, E. Jones, D. Piedra, S. Gradecak, and T. Palacios, "Impact of Al_2O_3 Passivation on AlGaN/GaN Nanoribbon HEMT," *IEEE Transactions on Electron Devices,* vol. 63, no. 1, pp. 318-325, 2016.

[25] K. Ohi, J. Asubar, K. Nishiguchi, and T. Hashizume, "Current Stability in Multi-Mesa-Channel AlGaN/GaN HEMTs," *IEEE Transactions on Electron Devices,* vol. 60, no. 10, pp. 2997-3004, 2013.

[26] S. Takashima, Z. Li, and T. Paul Chow, "Sidewall Dominated Characteristics on Fin-Gate AlGaN/GaN MOS-Channel-HEMTs," *IEEE Transactions on Electron Devices,* vol. 60, no. 10, pp. 3025-3031, 2013.

[27] M. Alsharef, R. Granzner, and F. Schwierz, "Theoretical Investigation of Trigate AlGaN/GaN HEMTs," *IEEE Transactions on Electron Devices,* vol. 60, no. 10, pp. 3335-3341, 2013.

[28] M. Alsharef, R. Granzner, F. Schwierz, E. Ture, R. Quay, and O. Ambacher, "Performance of Tri-Gate AlGaN/GaN HEMTs," in *IEEE, European Solid State Device Research Conference*, Lausanne, 2016.

[29] F. Huang, "Theory of Strain Relaxation for Epitaxial Layers Grown on Substrate of a Finite Dimension," *Physics Review Letters,* vol. 85, no. 4, pp. 784-787, 2000.

[30] Y. Sun, S. Thompson, and T. Nishida, "Physics of strain effects in semiconductors and metal-oxide-semiconductor field-effect transistors," *Journal of Applied Physics,* vol. 101, p. 104503, 2007.

[31] P. Novikov, Y. Bolkhovityanov, O. Pchelyakov, S. Romanov, and L. Sokolov, "Specific behaviour of stress relaxation in Ge_xSi_{1-x} films grown on porous silicon based mesa substrates: computer calculations," *Semiconductor Science and Technology,* vol. 18, pp. 39-44, 2003.

[32] M. Baykan, S. Thompson, and T. Nishida, "Strain effects on three-dimensional, two-dimensional, and one-dimensional silicon logic devices: Predicting the future of strained silicon," *Journal of Applied Physics,* vol. 108, p. 093716, 2010.

[33] B. Ridley, "Polarization-induced electron populations," *Applied Physics Letters,* vol. 77, no. 7, pp. 990-992, 2000.

[34] J. Ibbetson, P. Fini, K. Ness, S. DenBaars, J. Speck, and U. Mishra, "Polarization effects, surface states, and the source of electrons in AlGaN/GaN heterostructure field-effect transistors," *Applied Physics Letters,* vol. 77, no. 2, pp. 250-252, 2000.

[35] B. Jogai, "Influence of surface states on the two-dimensional electron gas in AlGaN/GaN heterojunction field-effect transistors," *Journal of Applied Physics,* vol. 93, no. 3, pp. 1631-1635, 2003.

[36] G. Koley and M. Spencer, "On the origin of the two-dimensional electron gas at the AlGaN/GaN heterostructure interface," *Applied Physics Letters,* vol. 86, p. 042107, 2005.

[37] L. Gordon, M. Miao, S. Chowdhury, M. Higashiwaki, U. Mishra, and C. Van de Walle, "Distributed surface donor states and the two-dimensional electron gas at the AlGaN/GaN heterojunctions," *Journal of Physics D: Applied Physics,* vol. 43, p. 505501, 2010.

[38] N. Goyal, B. Iniguez, and T. Fjeldly, "Analytical modeling of bare suface barrier height and charge density in AlGaN/GaN heterostructures," *Applied Physics Letters,* vol. 101, p. 103505, 2012.

[39] N. Goyal and T. Fjeldly, "Analytical modeling of AlGaN/AlN/GAN heterostructures including effects of distributed surface donor states," *Applied Physics Letters,* vol. 105, p. 023508, 2014.

[40] D. Segev and C. Van de Walle, "Origins of Fermi-level pinning on GaN and InN polar and non-polar surfaces," *Europhysics Letters,* vol. 76, no. 2, pp. 305-311, 2006.

[41] C. Van de Walle and D. Segev, "Microscopic origins of surface states on nitride surfaces," *Journal of Applied Physics,* vol. 101, p. 081704, 2007.

[42] S. Birner, "nextnano3 - next generation 3D nanodevice simulator," nextnano GmbH, 01 01 2017. [Online]. Available: http://nextnano.com/nextnano3/. [Accessed 18 06 2017].

[43] P. Harrison, Quantum Wells, Wires and Dots, 2nd ed., Chichester: Wiley-Interscience, 2005.

[44] A. Trellakis, T. Zibold, T. Andlauer, S. Birner, R. Kent Smith, R. Morschl, and P. Vogl, "The 3D nanometer device project nextnano: Concepts, methods, results," *Journal of Computer Electronics,* vol. 5, pp. 285-289, 2006.

[45] T. Andlauer, *Optoelectronic and spin-related properties of semiconductor nanostructures in magnetic fields,* Munich: Technische Universitat Munchen, 2009.

[46] M. H. Sadd, Elasticity -Theory, Applications, and Numerics, Burlington, MA: Elsevier Butterworth-Heinemann, 2005.

[47] S. Timoshenko and J. Goodier, Theory of Elasticity, York, PA: McGraw-Hill Book Company, 1951.

[48] C. Galeriu, *K.p theory of semiconductor nanostructures,* Worcester: Worcester Polytechnic Institute, 2005.

[49] L. Thomas, "The calculation of atomic fields," *Mathematical Proceedings of the Cambridge Philosophical Society,* vol. 23, no. 5, pp. 542-548, 1927.

[50] L. Lymperakis, P. Weidllich, H. Eisele, M. Schnedler, J.-P. Nys, B. Grandidier, D. Stiévenard, R. Dunin-Borkowski, J. Neugebauer, and P. Ebert, "Hidden surface states at non-polar GaN (10-10) facets: Intrinsic pinning of nanowires," *Applied Physics Letters,* vol. 103, p. 152101, 2013.

[51] F. Manouchehri, P. Valizadeh, and M. Kabir, "Determination of subband energies and 2DEG characteristics of $Al_xGa_{1-x}N$/GaN heterojunctions using variational method," *J. Vac. Sci. Technol. A,* vol. 32, no. 2, p. 021104, 2014.

[52] S. Birner, "1D Tutorial - Two-dimensional electron gas in an AlGaN/GaN field-effect transistor," nextnano, 7 January 2016. [Online]. Available: www.nextnano.com/nextnano3/tutorial/1Dtutorial_AlGaN_GaN_FET.htm. [Accessed 11 July 2016].

[53] S. Birner, "1D Tutorial - Simple SiGe structure," nextnano, 7 January 2016. [Online]. Available: www.nextnano.com/nextnano3/tutorial/1Dtutorial1.htm. [Accessed 11 July 2016].

[54] M. Mastro, J. LaRoche, N. Bassim, and C. Eddy Jr., "Simulation on the effect of non-uniform strain from the passivation layer on AlGaN/GaN HEMT," *Microelectronics Journal,* vol. 36, pp. 705-711, 2005.

[55] M. Povolotskyi, M. Auf der Maur, and A. Di Carlo, "Strain Effects in Freestanding Three-dimensional Nitride Nanostructures," *Physica Status Solidi c,* vol. 2, no. 11, pp. 3891-3894, 2005.

[56] J. Ristic, C. Rivera, E. Calleja, S. Fernandez-Garrido, M. Povolotskyi, and A. Di Carlo, "Carrier-confinement effects in nanocolumnar GaN/$Al_xGa_{1-x}N$ quantum disks grown by molecular-beam epitaxy," *Physical Review B,* vol. 72, p. 085330, 2005.

[57] A. Andreev and E. O'Reilly, "Theory of the electronic structure of GaN/AlN hexagonal quantum dots," *Physical Review B,* vol. 62, no. 23, pp. 15851-15870, 2000.

[58] C. RIvera, U. Jahn, T. Flissikowski, J. Pau, E. Munoz, and H. Grahn, "Strain-confinement mechanism in mesoscopic quantum disks based on piezoelectric materials," *Physical Review B,* vol. 75, p. 045316, 2007.

[59] D. Dinh, S. Kang, J. Yang, S.-W. Kim, and D. Yoon, "Synthesis and field emission properties of triangular-shaped GaN nanowires on Si(100) substrates," *Journal of Crystal Growth,* vol. 311, pp. 495-499, 2009.

[60] M. Laurent, G. Gupta, S. Wienecke, A. Muqtadir, S. Keller, S. DenBaars, and U. Mishra, "Extraction of net interfacial polarization charge from $Al_{0.54}In_{0.12}Ga_{0.34}N$/GaN," *Journal of Applied Physics,* vol. 116, p. 183704, 2014.

[61] H. Rahbardar Mojaver, F. Manouchehri, and P. Valizadeh, "Theoretical evaluation of two-dimensional electron gas characteristics of quaternary $Al_xIn_yGa_{1-x-y}N$/GaN hetero-junctions," *Journal of Applied Physics,* vol. 119, p. 154502, 2016.

[62] S.-C. Lin, C.-T. Kuo, X. Liu, L.-Y. Liang, C.-H. Cheng, C.-H. Lin, S.-J. Tang, L.-Y. Chang, C.-H. Chen, and S. Gwo, "Experimental Determination of Electron Affinities for InN and GaN Polar Surfaces," *Applied Physics Express,* vol. 5, no. 031003, pp. 1-3, 2012.

[63] P. Shields, M. Hugues, J. Zuniga-Perez, M. Cooke, M. Dineen, W. Wang, F. Causa, and D. Allsopp, "Fabrication and properties of etched GaN nanorods," *physica status solidi C,* vol. 9, no. 3-4, pp. 631-634, 2012.

[64] S. Kim, J. Seo, Y. Yoon, J. Kim, S. Cho, J.-H. Lee, and I. Kang, "Electrical Characteristics of Enhancement-Mode n-Channel Vertical GaN MOSFETs and the Effects of Sidewall Slope," *Journal of Electrical Engineering Technology,* vol. 10, pp. 742-748, 2015.

[65] S.-H. Park and S.-L. Chuang, "Crystal-orientation effects on the piezoelectric field and electronic properties of strained wurtzite semiconductors," *Physical Review B,* vol. 59, no. 7, pp. 4725-4737, 1999.

[66] S.-H. Park, "Crystal Orientation Effects on Electronic Properties of Wurtzite GaN/AlGaN Quantum Wells with Spontaneous and Piezoelectric Polarization," *Japanese Journal of Applied Physics,* vol. 39, no. 6A, pp. 3478-3482, 2000.

[67] D. Shibata, R. Kajitani, M. Ogawa, K. Tanaka, S. Tamura, T. Hatsuda, M. Ishida, and T. Ueda, "1.7 kV / 1.0 mOhm cm^2 Normally-off vertical GaN transistor on GaN substrate with regrown p-GaN/AlGaN/GaN semipolar gate structure," in *International Electron Devices Meeting*, San Francisco, 2016.

[68] K. Ren, Y. Liang, and C.-F. Huang, "Physical Mechanism of Fin-gate AlGaN/GaN MIS-HEMT: Vth Model," in *IEEE Workshop on Wide Bandgap Power Devices and Applications*, Fayetteville, AR, 2016.

[69] K.-S. Im, V. Sindhuri, Y.-W. Jo, D.-H. Son, J.-H. Lee, S. Cristoloveanu, and J.-H. Lee, "Fabrication of AlGaN/GaN delta-shaped nanowire fin-shaped FETs by a top-down approach," *Applied Physics Express,* vol. 8, no. 066501, pp. 1-3, 2015.

[70] H. Yoon, M. Min, J. Lee, D. Kang, H. Ahn, H. Kim, and J. Lim, "Microwave low-noise performance of 0.17 μm gate-length AlGaN/GaN HEMTs on SiC with wide head double-deck T-shaped gate," *IEEE Electron Device Letters,* vol. 37, no. 11, pp. 1407-1410, 2016.